8-2013

Growth and Properties of Boron Phosphide Films on Silicon Carbide

Guoliang Li
gli11@utk.edu

To the Graduate Council:

I am submitting herewith a dissertation written by Guoliang Li entitled "Growth and Properties of Boron Phosphide Films on Silicon Carbide." I have examined the final electronic copy of this dissertation for form and content and recommend that it be accepted in partial fulfillment of the requirements for the degree of Doctor of Philosophy, with a major in Materials Science and Engineering.

Gerd Duscher, Major Professor

We have read this dissertation and recommend its acceptance:

Philip D. Rack, Charles S. Feigerle, Carl J. McHargue

Accepted for the Council:
Dixie L. Thompson

Vice Provost and Dean of the Graduate School

(Original signatures are on file with official student records.)

Growth and Properties of Boron Phosphide Films on Silicon Carbide

A Dissertation Presented for the

Doctor of Philosophy

Degree

The University of Tennessee, Knoxville

Guoliang Li

August 2013

DEDICATION

I dedicate this to my parents, Huaisheng Li and Fengzhen Luan, and my brother, Guoqiang Li, for their endless patience, support, and love.

ACKNOWLEDGEMENTS

First of all, I owe a deep debt of gratitude to my academic advisor, Dr. Gerd Duscher for his guidance, support, patience, understanding and encouragement during my PhD study. He is not only a great mentor, but also a good friend to me. Without him, this dissertation would not have been possible.

I am grateful to Dr. Philip Rack and Dr. Charles Feigerle for supporting my research and serving on my committee, and Dr. Julia Abbott, Dr. Daniel Brasfield, Alexis Dale, Joo Hyon Noh, Dr. Lukosi Eric for collaboration on this research project.

I would like to acknowledge Dr. Kurt Sickafus and Dr. Carl Mchargue for being interested in my research and serving on my committee, and Dr. John Dunlap for his kind help in the laboratory.

I am thankful to all my labmates, Peizhi Liu, Ondrej Dyck, Mengkun Tian, Retish Sachan, Jingxuan Ge, Rylan Bledsoe, Chen Wang. We learned a lot from each other and it has been a great time improving together with them. They made my PhD life much easier and happier.

I would also like to thank the U.S. Department of Energy (DOE) for the financial support, Basic Energy Sciences (BES) and Joint Institute of Advanced Materials (JIAM) for microscope access.

ABSTRACT

Boron phosphide (BP) is a promising material for the development of high-efficiency solid-state thermal neutron detectors. However, the synthesis of good-quality BP film had been an obstacle. In this work, silicon carbide (SiC) substrates with vicinal steps instead of the conventional silicon (Si) substrates are used for BP growths. A series of growth experiments are performed and good-quality epitaxial BP films are successfully obtained and for the first time fully characterized. The optimized growth conditions are established, the film growth mechanism and defect origination mechanism are interpreted after an integrated experimental and theoretical study.

TABLE OF CONTENTS

CHAPTER 1. INTRODUCTION 1
CHAPTER 2. LITERATURE REVIEW 7
2.1. BP on Si 7
2.2. BP on Silica glass 11
2.3. BP on Sapphire 13
2.4. BP on GaN 14
2.5. BP on SiC 15
2.6. Summary and motivation 18
CHAPTER 3. RESEARCH METHODOLOGY 19
3.1. Synthesis: CVD 19
3.2. TEM sample preparation: FIB and conventional methods 19
3.3. Analysis: TEM, STEM, EELS, SAD, SEM and XRD 20
CHAPTER 4. EXPERIMENTAL RESULTS AND ANALYSIS 23
4.1. BP growth on Si 23
4.2. BP growth on SiC 27
4.2.1. Gas flow rate study 28
4.2.2. Substrate and interface study 30
4.2.2.1. SiC polytype and growth 31
4.2.2.2. SiC polarity and growth 33
4.2.2.3.SiC offcut angle and growth 37
4.2.3. Temperature study 40
4.2.3.1. XRD examination 41
4.2.3.2. SEM examination 44
4.2.3.3. TEM examination 48
4.2.4. Summary 50
4.3. Characterization of epitaxial BP on SiC 51
4.3.1. Structural and elemental analysis 52
4.3.1.1. SAD analysis 52

4.3.1.2. TEM and diffractogram analysis 55
4.3.1.3. EELS analysis 57
4.3.2. Defect identification 59
4.3.2.1. Misfit dislocations 59
4.3.2.2. Twin boundaries 61
4.3.2.3. Stacking faults and dislocation loops 64
4.3.2.4. Dislocations 65
4.3.2.5. Grain boundaries 66
4.3.3. Strain analysis 68
4.3.4. Discussion 69
4.3.5. Summary 74
4.4. Study of the initial stage of the growth 74
4.4.1. Thermodynamic Wulff construction of the nuclei 75
4.4.2. Kinetic Wulff construction of the nuclei 79
4.4.3. The fastest growth direction 80
4.4.4. Case study 84
4.4.4.1. Truncated octahedral nuclei 84
4.4.4.2. Twinned truncated octahedral nuclei 93
4.4.4.3. Side topic: Hexagonal nanorods 99
4.4.5. Summary 108
4.5. Optimized BP growth on SiC 110
4.5.1. SEM and XRD examinations 111
4.5.2. TEM examination 112
4.5.3. Summary 114
4.5.4. Discussion 116
CHAPTER 5. CONCLUSIONS AND DISCUSSIONS 119
CHAPTER 6. FUTURE WORK 122
REFERENCES 123
VITA 128

LIST OF TABLES

Table 1-1. General properties of some boron compounds.....4
Table 1-2. General properties of the materials involved in the dissertation. 6
Table 4-1. BP/Si sample list with processing parameters and XRD results. 24
Table 4-2. BP/SiC samples included in the gas flow rate study. 28
Table 4-3. Information summary of the SiC polarity study..... 34
Table 4-4. Information summary of the SiC offcut angle study..... 37
Table 4-5. Information summary of the temperature study. 41
Table 4-6. Defect types and distributions, origins, interpretations and improvement strategies.....110

LIST OF FIGURES

Figure 1-1. Device structure of a semiconductor neutron detector 2
Figure 1-2. Atomic model of zincblende BP 4
Figure 1-3. Atomic models of 3C-SiC, 4H-SiC and 6H-SiC 5
Figure 2-1. X-ray diffraction pattern of BP on Si. 9
Figure 2-2. Electron diffraction pattern of homoepitaxial BP and negative printed electron diffraction pattern of heteroepitaxial BP 10
Figure 2-3. Dark-field cross-sectional TEM image of the (111) BP layer grown on the (111) Si substrate 11
Figure 2-4. X-ray diffraction patterns of BP films on fused silica glass at various substrate temperatures. 12
Figure 2-5. High-resolution TEM image of (111)-BP layer grown on (0001) GaN ... 14
Figure 2-6. Oriented BP crystallites deposited on the Si face of a hexagonal SiC substrate 16
Figure 2-7. HRTEM image of (111) twins in BP grown on 6H-SiC 17
Figure 3-1. Illustration of TEM sample preparation using FIB 20
Figure 3-2. Conventional cross-section TEM sample preparation using PIPS 20
Figure 4-1. HRTEM image of the BP/Si interface 24
Figure 4-2. XRD examination of sample 37 25
Figure 4-3. HRTEM of the BP/Si interface with microstructure identified 26
Figure 4-4. SAD examination of the polycrystalline BP film grown on (001) Si 27
Figure 4-5. XRD examinations of sample 31 and 36 29
Figure 4-6. HRTEM and SAD pattern of the interface of sample 31 30
Figure 4-7. Low magnification HRTEM image of sample 76 (BP/3C-SiC) 31
Figure 4-8. High magnification HRTEM images of sample 76 (BP/3C-SiC) 32
Figure 4-9. HRTEM image of the epitaxial interface of sample 63 (BP/6H-SiC). 32
Figure 4-10. SEM, XRD and TEM comparisons of sample 63 (C-face) and sample 65 (Si-face) 33
Figure 4-11. Atomic models for BP epitaxy on C-face SiC as well as Si-face SiC 36

Figure 4-12. XRD examinations of the samples of the offcut angle study 38
Figure 4-13. TEM examinations of the samples of the offcut angle study 39
Figure 4-14. Plots of (111)/(220) ratio versus temperature 42
Figure 4-15. XRD examinations of the second temperature study 43
Figure 4-16. SEM examinations of the second temperature study 45
Figure 4-17. SEM Comparison between the nuclei formed at 850°C and 950°C 46
Figure 4-18. SEM images of the crystal islands of the 850°C (# 80) and 950°C (# 83) samples and geometric models of FCC singlecrystalline nanocrystals. 47
Figure 4-19. TEM examinations of the temperature study 49
Figure 4-20. An overview STEM bright-field image of the BP film cross-section prepared via FIB 52
Figure 4-21. Sequential SAD patterns throughout the epitaxial BP film 54
Figure 4-22. . HRTEM images of the BP film on SiC viewed in three different zone axes with diffractograms 56
Figure 4-23. EELS analysis of the BP/SiC interface 58
Figure 4-24. EELS investigation of common impurities 59
Figure 4-25. Z-contrast image of the interface in SiC [11-20] zone-axis illustrating misfit dislocations 61
Figure 4-26. HRTEM images of the twin boundaries in BP 63
Figure 4-27. A HRTEM image taken in the near interface region with corresponding diffractogram on the right 64
Figure 4-28. HRTEM images of the (111) planar defects in BP 65
Figure 4-29. Two grain boundary formation mechanisms 67
Figure 4-30. Lattice distortion evolution near the interface 68
Figure 4-31. TEM and atomic simulation showing the formation of Σ3 ITBs 70
Figure 4-32. TEM mapping of the twinned region 71
Figure 4-33. SEM image and the atomic models of the nuclei 73
Figure 4-34. Illustration of the surface free energy calculation via the broken-bond model 76

Figure 4-35. Thermodynamic Wulff construction of the equilibrium shape of BP .. 77
Figure 4-36. SEM image and the atomic models of the nuclei 78
Figure 4-37. The kinetic Wulff shapes for diamond as a function of the facet growth velocity ratio 79
Figure 4-38. Plots of XRD count ratio of (111)/(220) and (220)/(111) versus film thickness..... 81
Figure 4-39. SEM images of the cross-sections of the 3rd, 5th and 8th samples involved in of XRD count ratio versus film thickness plot 82
Figure 4-40. STEM images of the columnar structures in BP 82
Figure 4-41. Effect of facet growth rate on the shape evolution of a nucleus 83
Figure 4-42. SEM and STEM overview of the truncated octahedral nuclei 85
Figure 4-43. Composite image of nucleus 1 which consists of 3 grains and 2 orientations..... 86
Figure 4-45. STEM bright field image and Z-contrast image of nucleus 2 88
Figure 4-45. Composite image of nucleus 3 which consists of 4 grains and 3 orientations..... 90
Figure 4-46. Illustration of the correlation between Σ3 ITB and Moire fringes 91
Figure 4-47. TEM images of Σ3 ITB and Moire fringes..... 92
Figure 4-48. SEM and STEM overview images of the twinned truncated octahedral nucleus 94
Figure 4-49. Structural analysis of the twinned truncated octahedral nucleus. 97
Figure 4-50. Energies of [110] symmetrical tilt grain boundaries for diamond (triangle) and silicon (square) in the misorientation range $0°\leq\theta\leq70.53°$..... 99
Figure 4-51. The distribution and morphology of the nanorods of Sample 83 100
Figure 4-52. Cross-section analysis of the BP nanorod.....102
Figure 4-53. Planview analysis of the BP nanorod.....104
Figure 4-54. Stacking fault analysis of the BP nanorod.....106
Figure 4-55. 3D-examination of the precipitates (black spots) 108
Figure 4-56. SEM and XRD examinations of the optimized sample (#85).....111
Figure 4-57. TEM and SAD examinations of the optimized sample (#85) 112

Figure 4-58. Defect demonstrations of the optimized sample (#85).....115
Figure 4-59. Interface investigation of the optimized sample (#85).....117
Figure 4-60. Atomic models of BP growth on a smooth surface and a large-angle vicinal SiC surface.....118

CHAPTER 1. INTRODUCTION

Solid State neutron detection technology has the potential to yield breakthrough discoveries in material science and can provide detection devices critical to national security, nuclear engineering as well as the medical industry. The gold standard in neutron detectors is the ^{3}He detector, unfortunately, the supply of ^{3}He is dwindling and significant shortages are inevitable unless viable alternatives are identified. Besides, this conventional ^{3}He detector is still bulky and costly though it has been dominating for 60 years. Currently, the most commonly studied alternatives are gas-filled and scintillator based detectors. Although these are well established methods, solid-state semiconductor neutron detectors offer size and operational advantages that could significantly diversify the applications of such devices.[1] A solid state neutron detector would require minimal amplification, and offer compactness and efficiency unrivaled by gas-filled detectors and scintillators. Semiconductor detectors operate by induced current caused by the ionizing radiation incident on the material. Materials with known high neutron cross-sections such as $^{10}B(n,\alpha)$ and $^{6}Li(n,\alpha)$, are always used as conversion nuclei in semiconductor detectors.[1-3] ^{10}B in semiconductor detectors, compared to ^{6}Li, is preferable due to the higher neutron cross-section (3840 versus 940 barns), higher abundance (20% versus 7%) and reduced chemical reactivity. The interaction equation of neutron and ^{10}B is known as follows:

$$^{10}B+^{1}n\rightarrow{}^{7}Li\ (0.8MeV)+^{4}He(1.5MeV);$$

The working principle of the neutron detector [4] is shown in Figure 1-1. The incident neutron flux reacts with the boron compound and generates ^{7}Li and ^{4}He particles. The two kinds of particles are energetic and can create e-h pairs which can then be separated and detected as electrical signals.

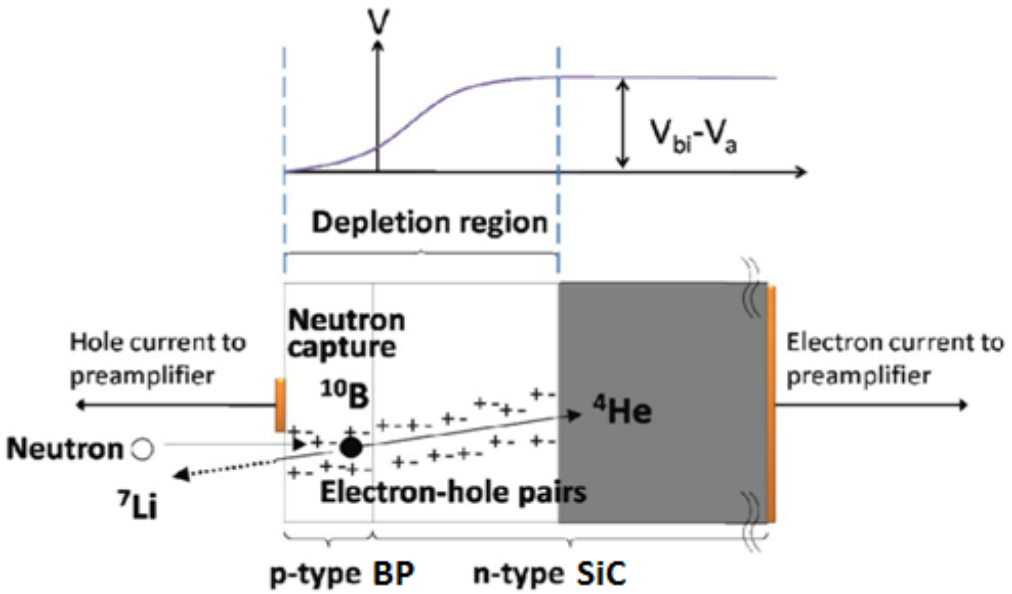

Figure 1-1. Device structure of a semiconductor neutron detector. [4]

Several designs of boron based neutron detectors have been presented over the years. The most common concept is to develop heterostructures using boron compound and another semiconductor material. According to the different roles of the boron compound in the device, these heterostrucures can be divided into two subclasses: (1) indirect-conversion and (2) direct-conversion. In the former structure, the boron compound is a thin layer coated on top of a space charge device. It is only used for converting neutron flux into energetic particles which can then create e-h pairs in the adjacent semiconductor device. While in the latter design, the boron compound is doped into either p-type or n-type to form a p-n junction with another semiconductor material. It works as a neutron converter and at the same time involves in charge collecting. [5] To further improve the detection efficiency, Rebecca J. Nikoliü suggested a pillar-structured neutron detector. [6] The pillar detector consists of etched silicon pillars of P-I-N diodes which are grown on a planar silicon substrate. The short distance between the pillars enables the energetic particles from the ^{10}B reaction to be captured by the intrinsic silicon in the maximum amount. To determine the most appropriate device structure, the travel

ranges of ^{7}Li and ^{4}He particles in the boron compound, the carrier mobility, doping density, etc. should be measured and the cost should also be considered.

Ideally, a semiconductor detector will be highly stable and have a wide band gap to allow for room temperature operation. One of the boron compounds that meets these specifications is cubic boron phosphide (BP), with an indirect band gap of 2.0 eV. The atomic model is shown in Figure 1-2. It displays rather peculiar behavior compared with other III-V family members. The atoms of BP are light elements and exhibits strong covalent bonding with only a small ionic contribution. High ionization energy is believed to be the origin of difference between BP and other III-V compounds. [7] The difficult synthesis and relatively low charge carrier mobilities have kept BP from wide device application. However, the excellent neutron absorption cross-section and natural abundance of ^{10}B makes boron based semiconductors good candidates for neutron detection. The increasing demand for compact high-efficiency neutron detectors has brought about people's interest on boron based semiconductors. An efficient BP detector would use isotopically enriched ^{10}B and, therefore, is affordable. A 200pm thick fully-depleted ^{10}BP diode would convert more than 95% of the thermal neutrons (λ = 1Å) into electron-hole pairs. [8] The good mobility of e-h pairs within BP (between 10 and 500cm^2/Vs [8, 9]) and the short distance (less than 200μm) they need to travel, indicates that thin-film BP detectors would have very fast response times. [10] All these advantages make BP the first choice in the fabrication of solid-state neutron detectors. Some general properties of BP and other Boron compounds are compared in Table 1-1. [11-17] $B_{12}P_2$ is boron subphosphide which is usually produced under high temperature and low pressure. [7] It has high resistivity, low charge carrier mobility and low thermal conductivity and, therefore, is an undesired phase during BP synthesis. This implies that a careful control of the temperature and pressure is needed during BP film growth.

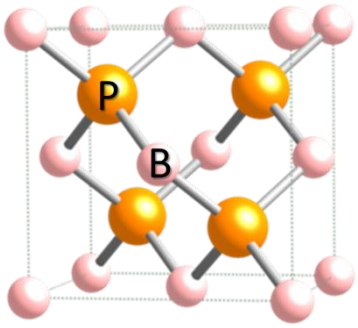

Figure 1-2. Atomic model of zincblende BP

Table 1-1. General properties of some boron compounds. [11-17]

	c-BP	***c-BN***	***B_4C***	***BAs***	***$B_{12}P_2$***
Structure	Cubic	Cubic	Rhombo-hedral	Cubic	Rhombo-hedral
lattice constant (Å)	4.54	3.62	a = 5.6 c = 12.07	4.78	a = 5.98 c = 11.81
Bandgap at RT (eV)	2.1	6.4	2.1	1.5	3.4
Coefficient of Thermal expansion (10-6 K-1)	3.6	1.2	5	-	-
Thermal conductivity (W/cm·K) at 300K	4.0	7.4	0.3-0.4	-	0.38
Resistivity (Ω-cm)	p-type, 10-12.5 n-type, 0.15-2.5	p-type, 1-1000 n-type, 1-1000	0.1-10	p-type, 0.01	p-type, 5.2e+4, 9.2e+4
Electron mobility (cm^2/Vs)	500	200	<1	100-400	50
Hole mobility (cm^2/Vs)	70	-	<1	-	-

Prior to the studies discussed in this work, BP films have been successfully grown by chemical vapor deposition (CVD) on substrates such as Si, GaN, and sapphire. In these studies, the large lattice mismatch (up to 17%) between the substrates and BP created films of insufficient quality for use as detectors.[18-28] BP has been grown by

CVD on silicon carbide (SiC) in very few cases,[18, 19] however, these films were not grown under conditions that promote step-flow growth and were not developed further. There is still plenty of room for the improvement of BP/SiC system, and this is the topic of this dissertation. Silicon carbide (SiC) exists in about 250 crystalline forms. [29] However, only three of all those SiC polytypes are widely used: 3C-SiC, 4H-SiC and 6H-SiC. The lattice mismatch between BP (111) plane and the close packed plane of SiC is only 4.5%. The atomic models are shown in Figure 1-3. Silicon carbide is very exciting to device designers because of its wide bandgap, high electron mobility and high thermal conductivity. These advantages promise substantial performance improvements over their silicon based counterparts. The material is suitable for operations at higher temperatures, higher voltages and higher frequencies under which conventional semiconductors cannot adequately perform. 3C-SiC has relatively few commercial uses because the synthesis of single crystal 3C-SiC is very difficult. Presently, all commercialized SiC devices are based on commercial SiC wafers with surfaces polished 3° to 8° off the (0001) basal plane. This off-axis polish provides a high density of atomic surface steps. The high step density and small terrace width ensures migration of mobile surface-adsorbed growth adatoms to step edges where they incorporate into the crystal. A facilitated BP growth is expected on these SiC wafers with vicinal steps. Some general properties of the materials involved in this work are listed in Table 1-2. The following paragraph is the overview of the dissertation.

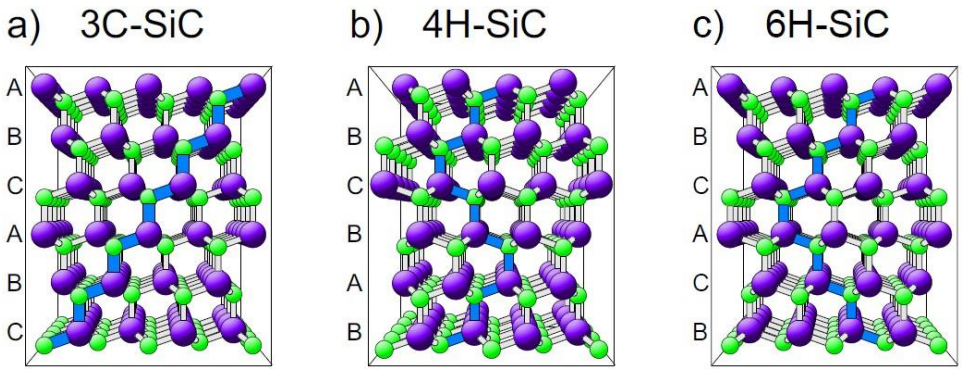

Figure 1-3. Atomic models of 3C-SiC, 4H-SiC and 6H-SiC. [30]

Table 1-2. General properties of the materials involved in the dissertation.

	BP	***Si***	***3C-SiC***	***4H-SiC***	***6H-SiC***
Crystal structure	FCC	FCC	FCC	HCP	HCP
lattice constant (Å)	4.54	5.43	4.36	a=3.07 c=10.05	a=3.07 c=15.11
Coefficient of Thermal expansion (10-6 K-1)	3.6	2.6	4.0	4.0	4.0
Thermal conductivity (W/cm·K) at 300K	4.0	1.5	3.6	3.7	4.9
Covalent radius (pm)	B(84)- P(107)	Si(111)- Si(111)	C(70)- Si(111)	C(70)- Si(111)	C(70)- Si(111)
Bond energy (eV)	2.9	2.3	3.5	3.5	3.5
Bandgap at RT (eV)	2.1	1.1	2.4	3.2	3.1
Electron mobility (cm^2/Vs)	500	1350	1000	//c: 1150 ⊥c: 950	//c: 100 ⊥c: 500
Hole mobility (cm^2/Vs)	70	480	40	120	80
Dielectric constant	11.0	11.9	9.7	10.0	10.0
Breakdown Field Strength (MV/cm)	0.4~1.0	0.3	2.0	2.2	2.5

The literature review is completed in Chapter 2. The development history, major challenges of BP film growth is summarized and the research motivation is included there. Research methodologies are listed in Chapter 3. Various electron microscopes are used for film examinations and analysis. Experimental results and microscopic analysis are presented in Chapter 4. The optimized growth conditions, film growth mechanism and defect origination mechanism are deduced for the BP/4H-SiC system based on the extensive experimental experiences and thorough structural analysis. Conclusions and discussions are made in Chapter 5. Lastly, future studies are proposed in the Chapter 6.

CHAPTER 2. LITERATURE REVIEW

The preparation of high-quality crystalline BP has been a great challenge for years. The common synthesis methods are CVD, Chemical Vapor Transport (CVT), and flux methods. [7] Among the above-mentioned methods, CVD is most widely used. Over the years, various substrates such as silicon (Si), silica glass, sapphire, gallium nitride (GaN) and SiC were employed.

2.1. BP on Si

Since Chu et al [19] first reported epitaxial growth of BP on a SiC substrate in 1971, several attempts have been made to grow BP epitaxially on Si substrates via CVD. Silicon is chosen as a substrate for epitaxial growth of BP because it is low cost, well characterized and easy to be etched, despite a large lattice mismatch of 17%.

In 1972, Nishinaga and Mizutani [31] first studied the epitaxial growth of BP on Si substrates with different orientations, through a thermal reduction process of BBr_3 and PCl_3 system. The growth rate was approximately 1μm/min and deposition temperature was in the range of 900°C to 1100°C. The layers grown on (111) surfaces were single crystal BP with the zincblende structure, while the layers on (100) surface were polycrystalline. The crystallinity was investigated via electron diffraction patterns on both sides of the BP film after removal of the Si substrate. Because of the differences of the lattice constant and the thermal expansion, grown samples were severely distorted and form a concave shape. This deformation was plastic and remained somewhat after the removal of the Si substrate.

In 1974, Takigawa et al, [32] performed thermal decomposition of diborane and phosphine. BP was epitaxially grown on Si wafers with [100], [110] and [111] orientations in the temperature range of 950°C to 1050°C with a growth rate of 70nm/min. The crystallographic orientation of BP was the same as that of the Si

substrates. The most favorable surface orientation for the hydride system was Si (100) in contrast to the halogen system Nishinaga and Mizutani used in 1972.

In 1975, Nishinaga and Mizutani [33] employed a growth rate as low as 100nm/min in the BBr3–PCl3–H_2–Si substrate thermal reduction system, they found that the best BP crystal was grown on the (100) substrate, in agreement with Takigawa et al,

In 1978, Takao Takenaka [34] did an interesting study on the diffused layers formed at the BP/Si interface during the epitaxial growth of n- or p-type BP on 2° off-axis (001) Si substrates. They used the B_2H_6 (1% in H_2) -PH_3(5% in H_2)-H_2 decompostion system. He reported that at an early growth stage of BP on Si substrates, a very small amount of boron or phosphorus covers the substrate surface first, generating a thin layer of either p-type or n-type Si. The thin diffusion layer affects the device performance. The formation and composition of the layer depends on substrate temperature, gas flow rate and the BP/Si interface quality.

In 1984, Y. Kumashiro [35] successfully grew thick BP (200-300μm) wafers on (100) and (111) faced Si substrates by thermal decomposition of B_2H_6 (1% in H_2) and PH_3 (5% in H_2) in a hydrogen atmosphere for deposition times of 24-28h. The temperature employed were 950°C for (100) faced Si samples and 1000°C for (111) faced Si samples. Still, the BP layers were severely distorted and formed a concave shape after cooling. The distortion caused cracks in BP. They also measured the microhardness of BP in different orientations of (100) and (111) planes and declared that the primary slip system was (111) < 110>. In 1988, He measured the electrical properties of the ^{10}BP single-crystalline wafers before and after thermal neutron irradiation. [36] No appreciable changes in electrical properties was observed for the (100) wafer. In the case of the (111) wafer, the carrier concentration for the n type increased and decreased for the p type after irradiation with thermal neutrons owing to the formation of donors caused by nuclear reaction of $^{10}B(n,\alpha)^7Li$. The detection efficiency was not mentioned.

In 1989, Devcom Inc. (manufacturers of CVD films) and RMD Inc. (manufacturers of radiation detectors) demonstrated the detection of neutron with a BP/Si diode. BP was deposited on (100) n-type Si with CVD. In their diode, the thickness of the depletion layer was only 10μm, which is about 20 times smaller than required for efficient neutron detection. The detection efficiency was poor.

In 2002, S. Nishimura [37] induced epitaxial BP on Si as a buffer layer to facilitate GaN growth. He used BCl3-PCl3-H_2-(100) Si thermal reduction system for BP epitaxy. To be noticed, he grew a very thin BP layer under 380°C and then heated the sample to 1030°C for further BP growth. And the growth rate was about 15nm/min. The X-ray diffraction pattern (Figure 2-1) indicates the good crystal-quality of the film.

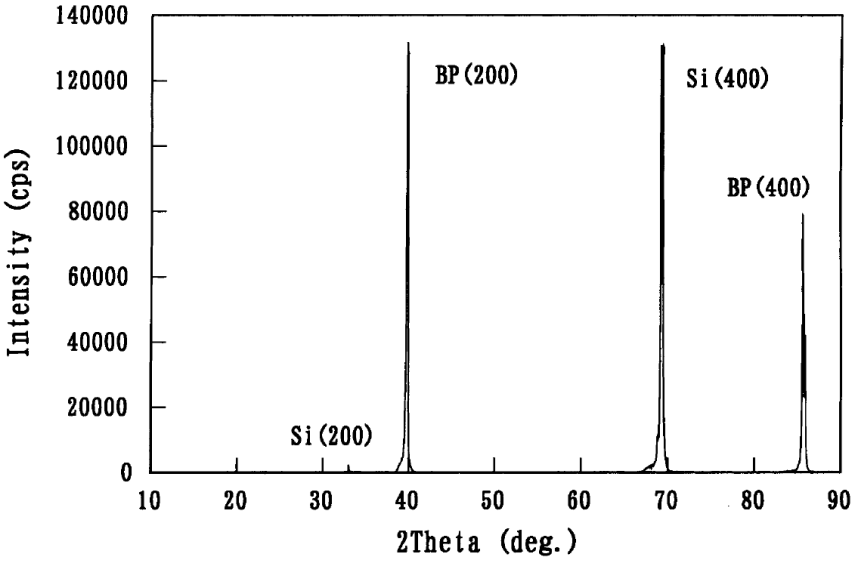

Figure 2-1. X-ray diffraction pattern of BP on Si. [37]

In 2003, M. Odawara [38] proposed BP homoepitaxy by a halide vapor phase epitaxy (VPE) procedure at 1030°C under atmospheric pressure. BP film was vapor-grown on (100) Si which had been etched to form quadrilateral shaped pits bounded by four (111) Si planes. Accompanying an epitaxial relationship of (100) [110]-Si // (100) [110]-BP, an eave layer of BP overhanging the pit was obtained. A

homoepitaxial BP films also grew toward the inside of the Si pit from the underside of the BP eaves layer. In contrast to the heteroepitaxial BP layer on the (100) Si surface, the homoepitaxially grown BP film generated no extra diffraction dots or diffused scattering due to twins or (111) planar defects (Figure 2-2). Therefore, this technique is advantageous in promoting the formation of BP films with fewer imperfections. This experiment confirmed the advantage of homoepitaxy, but the film did not meet the thickness requirement and it is hard to make a device from it.

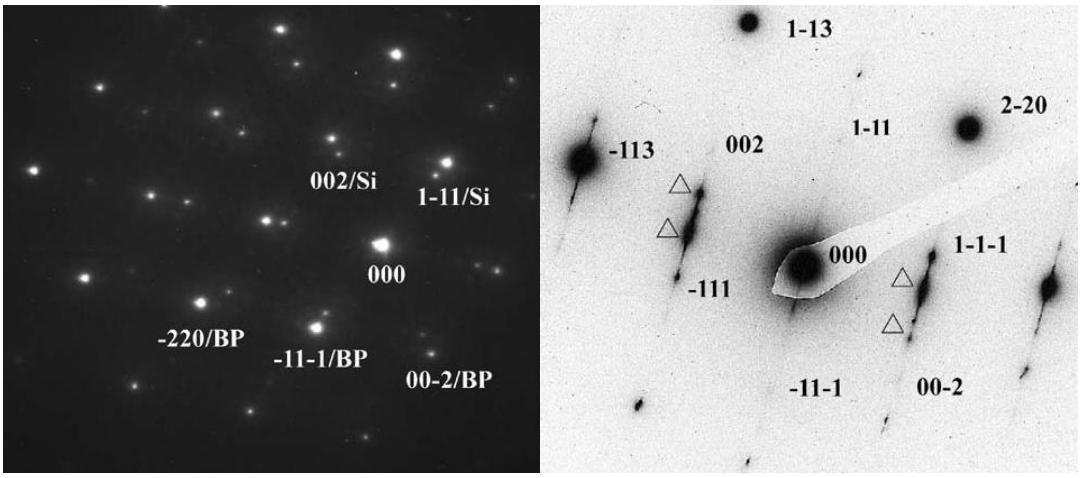

Figure 2-2. Electron diffraction pattern of homoepitaxial BP (left) and negative printed electron diffraction pattern of heteroepitaxial BP (right). [38]

In 2004, T. Yamashita [39] performed MOCVD on (111) faced Si substrate utilizing triethylboran ($(C_2H_5)B_3$) and phosphine (PH_3) as source gases. The growth rate was about 22.5nm/min and the deposition temperature was 1075°C. They obtained a 450nm thick epitaxial BP film with many twined domains (Figure 2-3) and the epitaxial relationship was confirmed as (111) [110]-Si // (111) [110]-BP. The twins bounded on the (111) BP planes aligned to either [110], [011], or <101> Si. The (111) BP layer grown on the (111) Si substrate through the aggregation of twinned (111) BP oriented uniformly in the direction parallel to the [110] Si. The diffraction contrast distribution in Figure 2-3 indicates that there are already many

grain boundaries within the 450nm film. The crystal quality of the film is poor and further film growth will not be epitaxial.

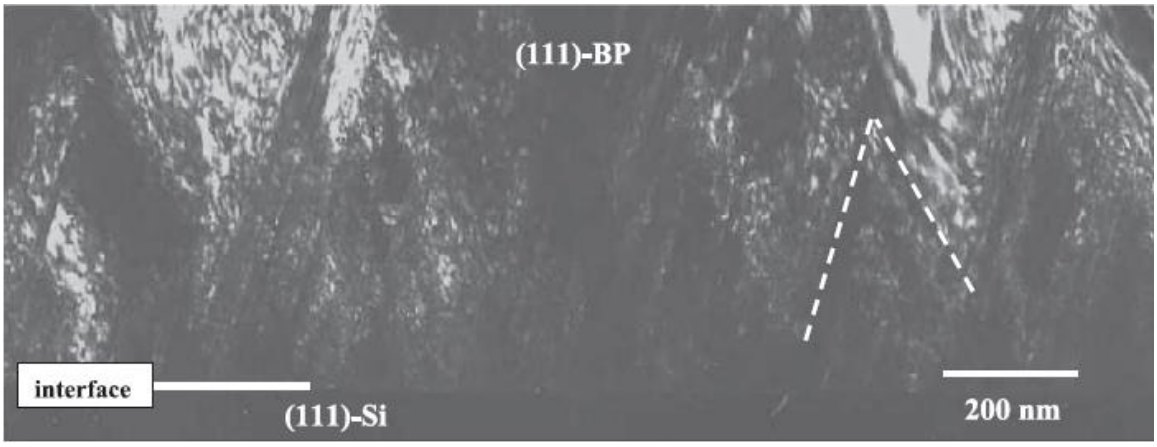

Figure 2-3. Dark-field cross-sectional TEM image of the (111) BP layer grown on the (111) Si substrate. The twinned domain is indicated with dashed lines. [39]

In general, people have successfully grown epitaxial BP on Si substrate utilizing either hydride decomposition or halide thermal reduction process. However the film quality cannot reach the rigorous demand of modern devices because it was always severely distorted, heavily defective and easily to crack. Most importantly, neutron detection efficiency of BP/Si was only 1% which is far from expectation. [10] I believe all these drawbacks are mainly resulted from the interface quality of the BP/Si system and the difference of thermal expansion coefficient.

2.2. BP on Silica glass

In 1997, Y. Kumashiro tried BP growth via CVD on fused silica glass at different temperatures. [22] The thermal decomposition system was B_2H_6 (1% in H_2) and PH_3 (5% in H_2) in hydrogen atmosphere. The growth rates were in a range from 5.7μm/h to 8.5μm/h. According to the XRD patterns, all the films were

polycrystalline except the one grown at 700°C which contains amorphous structures as well. The XRD results are shown in Figure 2-4.

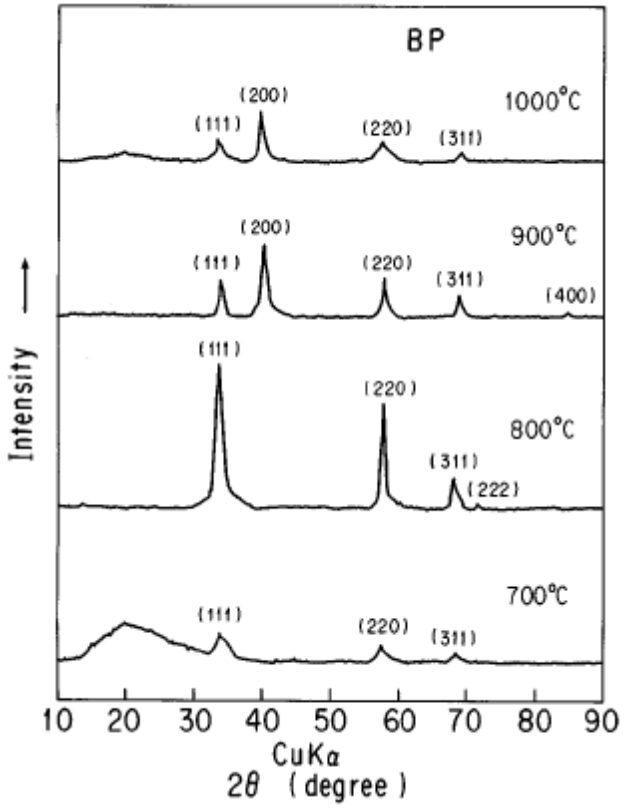

Figure 2-4. X-ray diffraction patterns of BP films on fused silica glass at various substrate temperatures.

In 2000, Y. Kumashiro conducted the same experiment with the aid of a deuterium lamp and he claimed that the crystal quality was improved. [27] According to him, the deuterium lamp is effective for the excitation of the source gases and, therefore, decreases the activation energy of the film growth.

In 2007, S. Dalui et al, deposited a phosphorous-rich BP thin film onto fused silica by co-evaporating high-purity boron and phosphorous. [40] The film was compact and

smooth. The Corresponding XRD experiment revealed the amorphous nature of the film.

Silica glass by itself is an amorphous material; therefore, BP epitaxy is not achievable on it. It can be concluded that BP grows via random nucleation or in the form of amorphous structure on silica glass. The multiple diffraction peaks presented in the XRD pattern shown in Figure 2-4 supports the conclusion.

2.3. BP on Sapphire

In 1994, Y. Kumashiro et al, conducted BP growth on sapphire A-plane using via CVD. [41] They first deposited a 40nm BP amorphous layer at 550°C and then obtained crystalline BP growth on the pre-deposited buffer layer at 1000°C. This method was named as the two-step method. The key point of it is to deposit a buffer layer at low temperature before subsequently deposition at high temperature. Reflection high-energy electron diffraction (RHEED) revealed that the film contains a large amount of twin boundaries near the surface.

In 2010, Y. Kumashiro et al, prepared BP films on sapphire R-plane via CVD. [28] Direct growth and two-step growth were both conducted in their experiment. The film directly deposited on the substrate showed polycrystalline properties. They attributed this to the large lattice-mismatch (4.6% and 11.5%) between the sapphire R-plane and BP (100) plane. As for the two-step deposition, a 100-150nm buffer layer was deposited at 600°C and then epitaxial growth was achieved at 1000°C. The film deposited with the two-step method showed improved quality. The X-ray diffraction pattern of the improved film was predominantly oriented to BP (111) and BP (200).

2.4. BP on GaN

GaN epitaxial growth using BP as a buffer layer has been studied for a long time because GaN based semiconductor devices are commercially available and occupy a large market share. However, BP epitaxy on GaN did not draw much attention.

In 2005, M. Odawara [42] reported BP growth on (0001) GaN by an atmospheric-pressure Metal-organic vapor phase epitaxy (MOVPE) procedure. The epitaxial relationship was (0001), <11-20>-GaN // (111), [110]-BP. A large amount of dislocations, double-positioning boundaries and microtwins were observed. The growth technique needs to be modified to suppress these imperfections. Figure 2-5 is a HRTEM image of the interface taken in [110] zone-axis. The author claimed that T1, T2 and T3 are microtwins. However, to me T2 seems like BP crystal viewed in [112] zone-axis, thus the boundary between T1 and T2, T2 and T3 should be grain boundaries instead of twin boundaries.

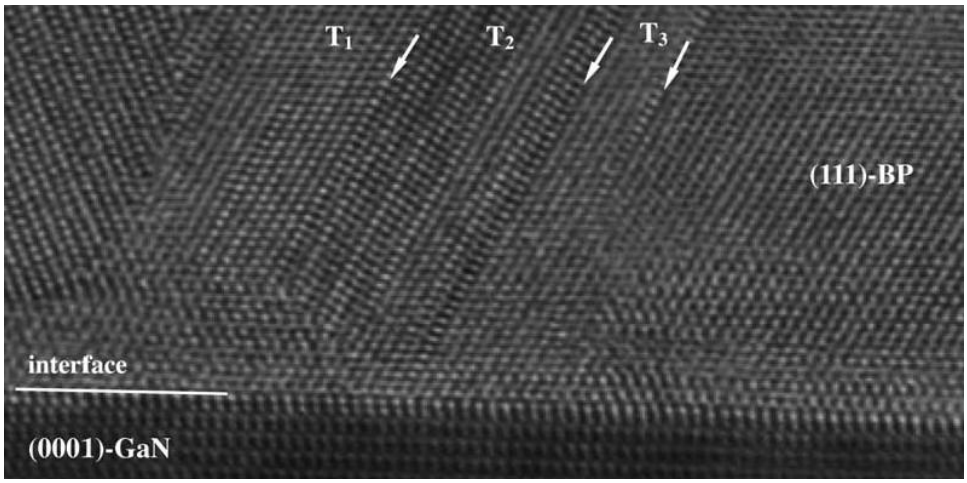

Figure 2-5. High-resolution TEM image of (111)-BP layer grown on (0001) GaN. Grain boundaries in the (111)-BP layer are indicated with arrows (↓). [42]

Ideally, the 1% lattice mismatch of GaN with BP should make it a good candidate for BP epitaxy. However, the interface quality of the GaN/BP sample shown in Figure 2-

5 is not satisfactory. An optimization of the growth parameters should be able to suppress the amount of defects. Note though, degenerated epitaxy is always induced when the three-fold symmetric (111) plane of a BP grows on the six-fold symmetric (0001) surface of GaN. This kind of epitaxy will inevitably result in twin boundaries at the interface. More importantly, the cost of high-quality GaN wafers is much higher than any other common substrates.

2.5. BP on SiC

SiC is now popular in epitaxy of semiconductor materials from considerations of chemical inertness, crystal symmetry, lattice parameters, thermal properties and electron mobilities which are crucial for device purposes. But not much work has been done on the SiC/BP system since Chu first reported BP epitaxy on SiC in 1971. Because large-diameter SiC wafers with high crystalline quality, controlled impurity content and precisely controlled offcut techniques was not well developed until late 1990s. [43] The basal plane of hexagonal SiC has three-fold symmetry and a lattice parameter of 3.07Å, which is very similar to the interatomic distance in (111) plane of boron phosphide, 3.21Å [21]. The lattice mismatch is only 4.5%.

In 1971, T. L. Chu et al, [19] for the first time reported BP epitaxy on hexagonal SiC. They conducted both hydride decomposition and halide thermal reduction experiments. BP formed by hydride decomposition on Si-face SiC tended to be single crystalline with different stacking possibilities under higher temperature and polycrystalline under lower temperature. As is shown in Figure 2-6, when the nucleated crystal sites with different stacking possibilities meet, twin boundaries are generated. Though the author didn't provide cross-sectional TEM images, we are unsure about the crystal quality. For C-face SiC, BP was mostly polycrystalline at lower substrate temperature while it showed some preferred orientations at higher temperature. BP layers deposited by halide thermal reduction at 1050-1150°C have

been found to be single crystalline and epitaxial with respect to the substrate. The epitaxial relationship is (0001) <11-20>-SiC // (111) [110]-BP.

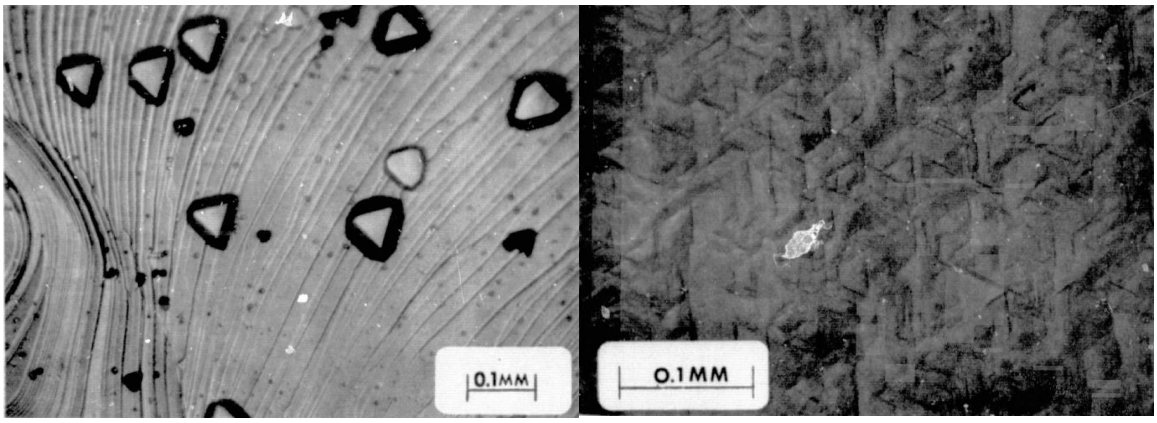

Figure 2-6. Oriented BP crystallites deposited on the Si-face of a hexagonal SiC substrate, early stage planview on the left and the surface of the 40µm film on the right. The triangular crystallites of opposite orientations indicate different stacking possibilities. [19]

In 1997, Michael Fitzsimmons et al, at Los Alamos National Lab explored CVD methods to produce BP films on silicon carbide substrates. [10] They proposed BP epitaxy on SiC instead of Si to avoid the problems induced by the poor lattice mismatch between BP and Si.

In 2005, T. Udagawa [44] grew epitaxial BP on 6H-SiC by means of MOVPE procedure using triethylboran ($(C2H_5)B_3$) and phosphine (PH_3) as source gases. The temperature was in 900°C and the film thickness was 440nm. The epitaxial relationship is: (0001) <11-20>-SiC // (111) [110]-BP. He found many twins near the interface and also some randomly configured atomic planes (Figure 2-7). He concluded that the defective interface was caused by the lattice mismatch.

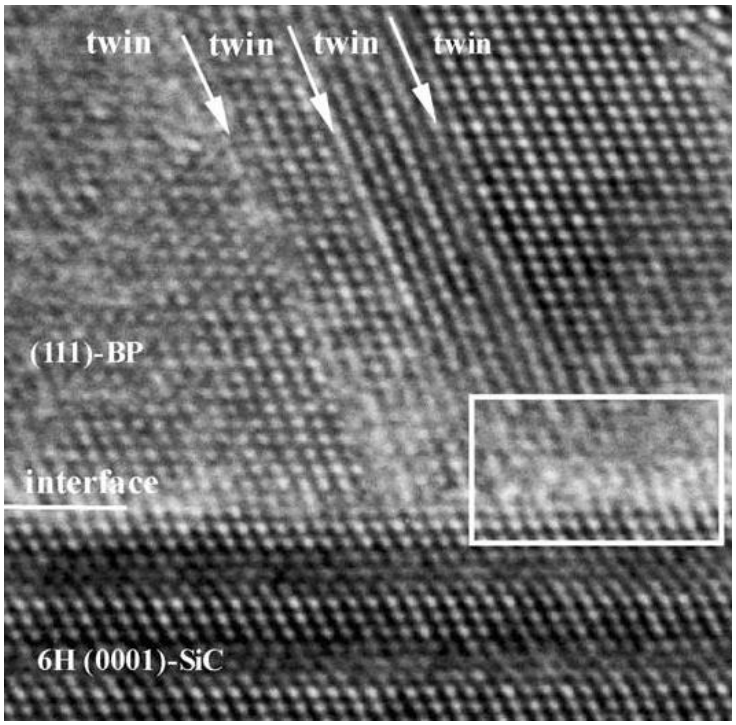

Figure 2-7. HRTEM image of (111) twins (→) in BP grown on 6H-SiC (magnification: 5300K). A region in which atomic planes in the BP layer configures randomly is shown in the rectangular frame. [44]

BP/ SiC are supposed to be a better epitaxy system than BP/Si, but apparently not much effort has been spent on this system. According to the work that had already been accomplished on BP/SiC system, defect density is high near the interface and the main defect is twin boundary. However, Alexander reported that electron mobility in 3C-SiC which also has the same atomic structure as BP, is higher when the twin concentration is higher. [57] He believed that twin boundaries behave as defect sink which makes the electron mobility larger. Therefore, twin boundaries might not be detrimental the device performance, while dislocations and incoherent grain boundaries which cause dangling bonds are not favorable. Since single crystal SiC wafers with very low impurity content are already commercially available, the substrate influence on BP epitaxy can now be minimized. Moreover, the off-axis SiC wafers with vicinal steps can provide more nucleation sites and promote step-flow growth; therefore, high-quality epitaxial film can be expected.

2.6. Summary and motivation

To sum up:

(1). Most of BP growths were performed on Si which is not an ideal substrate due to its large lattice mismatch (17%) with BP. SiC is better suited for BP growth from considerations of chemical inertness, crystal symmetry, lattice parameters, thermal properties and electron mobilities which are crucial for device purposes. But very little work has been done on SiC/BP system.

(2). Epitaxial BP has been reported in many articles; however, none of them gave a thorough characterization of the BP film. Questions like how many types of defects are generated during growth; how they originate and evolve; how they distribute within the film, were never solved.

(3). Various techniques were employed to determine the crystalline quality, such as imaging a small area of the interface, taking RHEED patterns of the surface, or simply showing XRD data. But these techniques are not able to precisely determine the film quality independently. Good result from each of these techniques alone is prerequisite but does not guarantee a good crystal-quality.

Therefore, I am motivated to:

(1). Perform a thorough study on SiC/BP system and optimize BP growth to produce high-quality film for detector use.

(2). Characterize the BP film synergetically with TEM, SEM and XRD and correlate the structure change with growth parameters to predict film growth.

(3). Study the effect of SiC/BP interface on defect variety, origination and evolution and deepen the fundamental understanding of epitaxial growth.

CHAPTER 3. RESEARCH METHODOLOGY

The film is synthesized by CVD and examined with TEM, STEM, SEM and XRD. TEM samples are prepared via FIB which is much more efficient than the conventional approaches. The turnaround time is shortened and a wealth of data is collected.

3.1. Synthesis: CVD

Thin BP film CVD are performed using diborane and phosphine with a balance of hydrogen gas with RF induction heating. [45] The gas reaction equation is as follows:

$$B_2H_6+2PH_3 \rightarrow 2BP+6H_2$$

Growth temperature, pressure, flow rate ratio between B_2H_6 (1% in H_2) and PH_3 (5% in H_2), wafer sizes, and substrate types were all controlled to find their respective influences on film growth and quality. Julia Abbott, Daniel Brasfield and Alexis Dale did the film synthesis work.

3.2. TEM sample preparation: FIB and conventional methods

FIB method is relatively new compared to conventional method. It is an efficient way of preparing TEM samples. The instrument used for this work is Zeiss Auriga SEM/FIB cross beam microscope. It has a field emission electron column for high-resolution electron imaging and a Canion Ga+ column for precision ion beam milling. The ion beam operation is from 5keV to 30keV. It has a super eucentric stage and nano-manipulator for TEM sample prep.

The first step of preparing a cross-section TEM sample is to cut a lamella which includes a protection layer, the film cross-section and some substrate materials. Then lift it out and weld it to the copper grid with the nano-manipulator. After that, use small beam current to polish the lamella till it becomes electron transparent (usually <80nm). The Process of TEM sample preparation is illustrated in Figure 3-1.

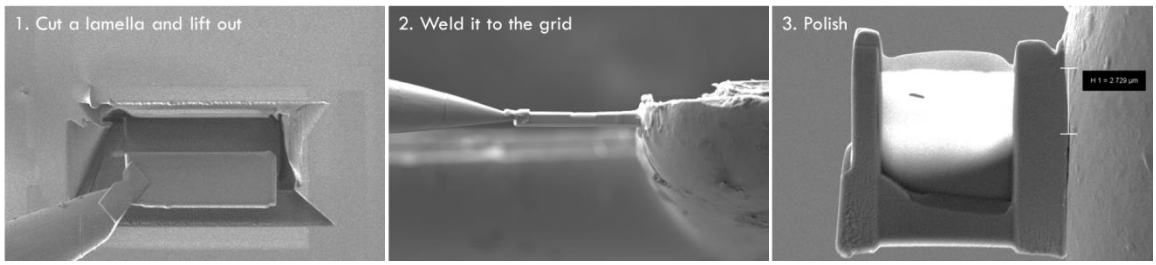

Figure 3-1. Illustration of TEM sample preparation using FIB.

The conventional way of preparing TEM samples is to first mechanically polish a sandwiched sample to less than 20μm and then put it in a precision ion-polishing system (PIPS) for final polish. The PIPS uses Ar^+ ion beam to bombard the mechanically polished sample to create a thin area which is electron transparent. The process is illustrated in Figure 3-2. A thin sample with a smooth surface can short the milling time considerably.

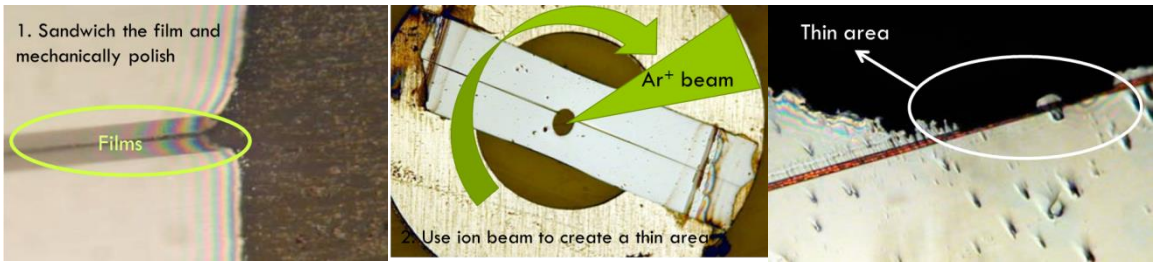

Figure 3-2. Conventional cross-section TEM sample preparation using PIPS.

3.3. Analysis: TEM, STEM, EELS, SAD, SEM and XRD

Various methods are used to characterize the BP film. They are transmission electron microscopy (TEM); scanning transmission electron microscopy (STEM); scanning electron microscopy (SEM); electron energy-loss spectrum (EELS); selected area diffraction (SAD); and X-ray diffraction (XRD).

The TEM used in this work is a Zeiss Libra 200MC. It has a Schottky field emission with Ω monochromator. The accelerating voltage range is 60-200kV. The point resolution is 2.4A and energy resolution is better than 0.2eV. Its high tilting capability enables us to conduct investigations from different angles and to construct 3-D images. High-resolution transmission electron microscopy (HRTEM), SAD, EELS can be performed using this TEM. With this powerful TEM, we can observe defects like dislocations, dislocation loops, stacking faults, precipitates directly; determine the thickness, symmetry, polarity, microstructure and strain; map the element distribution and find the impurities. [62]

HRTEM are formed by illuminating parallel electron beams on the sample and use the diffraction contrast for imaging. Periodicity and crystallographic information are included in the image. Defects like grain boundaries and dislocations would change the periodicity of the atom arrangements and show different contrast compared to the regular crystals. Morphology, microstructures and defect distribution can be visualized. The fast Fourier transform (FFT) of a HRTEM image is its corresponding diffractogram. Crystal phases and orientations can be identified directly by fitting the diffraction spots, distortions can be calculated using the distance between diffraction spots.

SAD allows one to choose regions of interest in the film and extract electron diffraction patterns which contain crystallographic and defect information. With the Libra 200MC, SAD study is able to cover an area as large as $3\mu m^2$. While diffractogram analysis is limited by the information/mm, limit of the corresponding HRTEM image, therefore, the area limit is about $0.02\mu m^2$. In SAD patterns, all diffraction spots are blurred because the diffracted wave is convoluted with the aberration function. Diffractogram is the Fourier transform of the aberration limited image with the effect that the diffraction spots are differently blurred. Some of the spots may be absent when the contrast transfer function (CTF) is zero at certain frequencies; therefore, using different defocus for imaging is necessary.

EELS involves analyzing the energy distribution of initially monoenergetic electrons, after they have interacted within a specimen. [63] The lost-energy of an electron after the interaction for each element is characteristic and, therefore, can be used for element identification. Also, the areal density of the atoms can be correlated with the number of interacted electrons, and this property makes quantitative elemental analysis available. Model based EELS quantification in this dissertation was performed with Quantifit 9.02, a python program developed by Dr. Gerd Duscher's research group.

SEM was used to perform surface morphology and cross-section analysis. We have two models of SEM in this lab, one is LEO 1525 and the other is Zeiss Auriga SEM which works synergetically with FIB. LEO 1525 may be run at accelerating voltages from 0.5kV to 20kV and the resolution of the microscope is 1.5nm at 20kV and 3.5nm at 1kV. The electron beam operation of the Zeiss Auriga SEM is from 0.1 to 30keV and the resolution can reach 1.0nm and 4.0nm at the accelerating voltage of 30kV and 1kV, respectively.

STEM is another powerful tool for film analysis. Oak Ridge National Laboratory has several aberration-corrected STEMs which can reach a spatial resolution of below 1A. The one we used is VG 603 U with Nion aberration corrector running at 300kV acceleration voltage. By taking Z-contrast images in which the intensity is atomic number dependent, we were able to find out the how the atoms arrange at the interface.

XRD is a popular non-destructive analytical technique which reveals information about the crystal structure, chemical composition of thin films. The one we used for this work is PANalytical Empyrean.

CHAPTER 4. EXPERIMENTAL RESULTS AND ANALYSIS

Growth of boron phosphide is traditionally done on Si and so we start the result chapter (4.1) with the Si/BP system as a reference for the more important study of BP on SiC. A wide variety of growths on SiC were done and the appropriate growth parameters were found (4.2). The crystal quality and usability of our system is critically associated with the defects and the full characterization is presented in sub-chapter 4.3. The important defects are already present in the initial growth and, therefore, warranted a detailed study (4.4). Nucleation and growth mechanisms are better understood in this sub-chapter. Based on the extensive experiences and the theoretical studies, the best growth parameters, growth mechanism and defect origination mechanism are established. The best sample grown with the optimized parameters is presented in detail in 4.5 as the final of this results chapter.

4.1. BP growth on Si

BP growths on Si (100) wafers were performed prior to our studies on SiC/BP system. These initial experiments helped us test the new-built CVD system and verify the quality of the source gases. Silicon wafers are chosen for the test growths because they are common and cheap. BP deposition has been previously reported on Si, the results in this sub-chapter are compared to those in the literature to confirm BP film identity and quality. Also, these experiments can be used as references for our later SiC/BP system. We were expecting an epitaxial interface like what is shown in Figure 4-1. The epitaxial relationship is BP (001), (110)// Si (001), (110).

Several growths of BP on (100) Si substrates were performed. The main parameters that have been varied for these growths are the flow rate, the partial pressures of precursor gases and the substrate temperature. The sample list with their respective processing parameters and XRD results are shown in Table 4-1. The XRD pattern of sample 37 is shown in Figure 4-2.

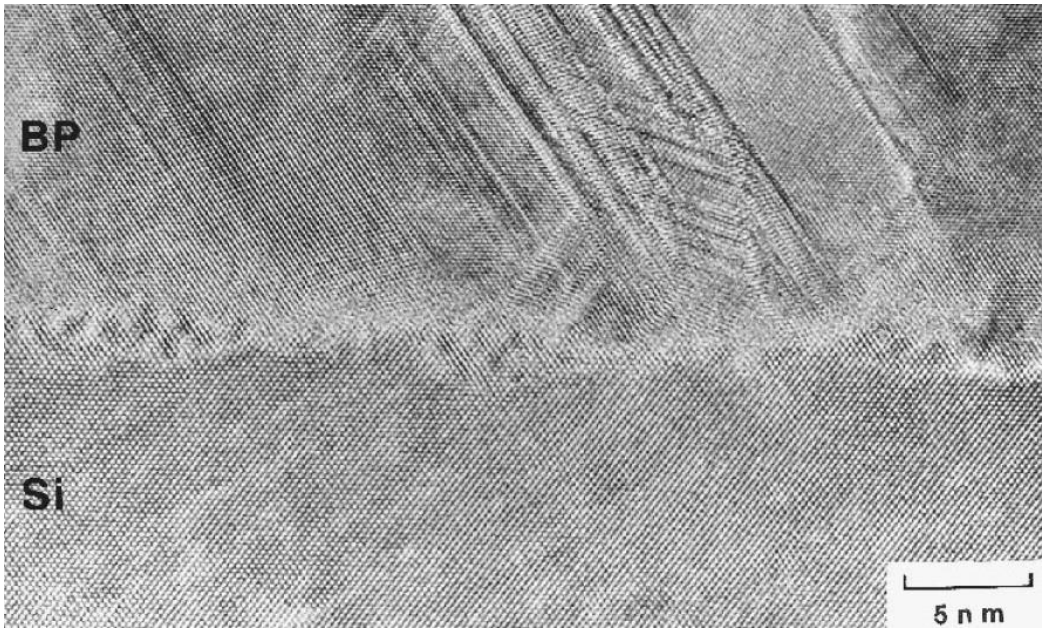

Figure 4-1. HRTEM image of the BP/Si interface. the epitaxial relationship is BP (001), (110)// Si (001), (110). (Courtesy of Dr. Y. Fujita, Itami Laboratory, Sumitomo Electric Industries.)

Table 4-1. BP/Si sample list with processing parameters and XRD results

Sample No.	*Pressure (Torr)*	*Temp (°C)*	*H_2 (sccm)*	*PH_3 (sccm)*	*B_2H_6 (sccm)*	*Run time (hr)*	*Growth Rate (μm/h)*	*(111), (220) Counts in XRD*
1	630	810	2500	300	20	1.5	6	-
8	630	830	2500	300	30	2	2.1	30, 240
22	630	803	2500	300	30	0.5	5.4	50, 380
23	630	805	2500	100	10	0.5	2	120, 210
24	630	805	2500	300	30	0.5	5.3	120, 2100
25	630	798	2500	300	10	0.5	1.7	350, 5600
26	630	811	2500	150	30	0.5	5.3	1500, 2800
27	630	855	2500	300	30	0.5	5.1	550, 5800
37	630	812	2500	100	20	0.5	3.7	2600, 2800
38	630	820	2500	300	30	0.16	4.7	1400, 800
39	630	821	2500	100	10	2	2.3	2000, 13000
44	630	810	2500	100	20	0.5	4.2	-

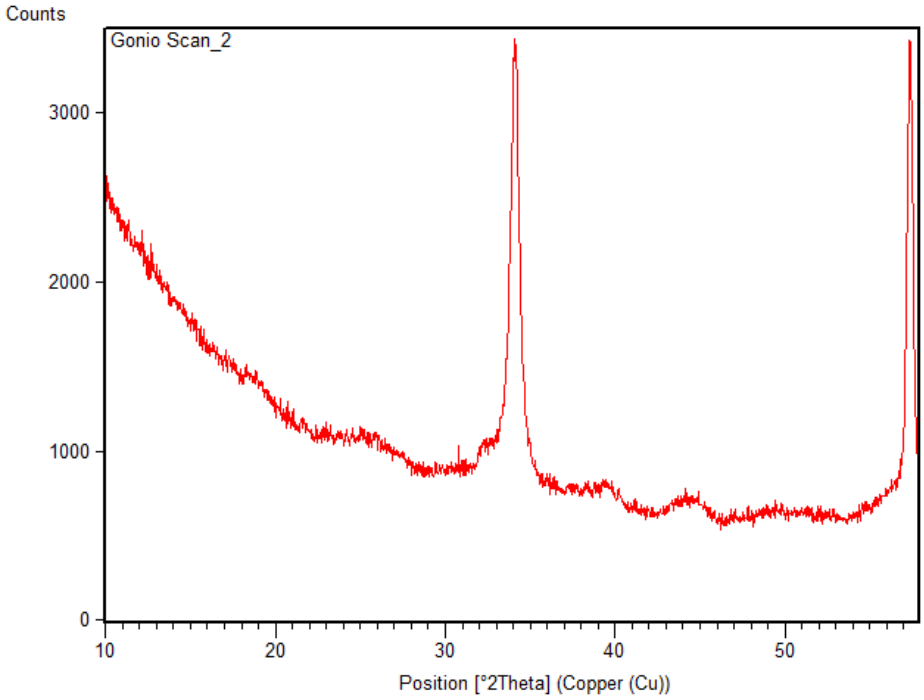

Figure 4-2. XRD examination of sample 37, BP (111) and (220) diffractions at 34.17° and 57.33° were observed. There is no BP (200) diffraction.

According to the θ/2θ scan results of all the samples, there are always two strong peaks besides the Si (200) peak at 32.95°. They are BP (111) and (220) diffractions at 34.17° and 57.33°, respectively. These peak positions indicate the formation of cubic BP. However, none of the films is epitaxial since no quantifiable BP (200) peak was ever observed. To understand the growth mechanism, TEM analysis is then performed on sample 37 which gave approximately the equal amount of (111) and (220) diffractions.

A HRTEM image of the interface is shown in Figure 4-3. A 50nm amorphous BP layer was observed and it spread over the whole interfacial region. On top of the amorphous layer, polycrystalline BP nucleated and grew. The grain size varies along the growth direction, and the evidence of this statement is shown in the following SAD analysis (Figure 4-4). Because the number of Bragg diffractions in the near-surface region is less than that of the near-interface region. This means the BP

grains at the surface are fewer and larger, accordingly. The orientation of BP is not aligned with any of the silicon orientations. This is due to the fact that the crystalline BP is grown on amorphous BP and nucleates randomly. Detailed studies on BP nucleation are presented in sub-chapter 4.4.

There are many factors that might contribute to the formation of the amorphous layer. The 17% lattice mismatch between the film and substrate maybe the main reason. This makes the bonding of the first several boron phosphide layers very difficult. Besides, the 800°C -850°C temperature range might also be unfavorable for the adatoms to diffuse far enough on the silicon substrate to find another atom to form a bond. Varying gas flow rates did not bring epitaxy either. Moreover, the large difference of thermal expansion properties between Si and BP can be another concern if the device has to undergo frequent temperature changes. In general, we don't consider silicon an ideal substrate for BP epitaxial growth; therefore, we proceed with SiC.

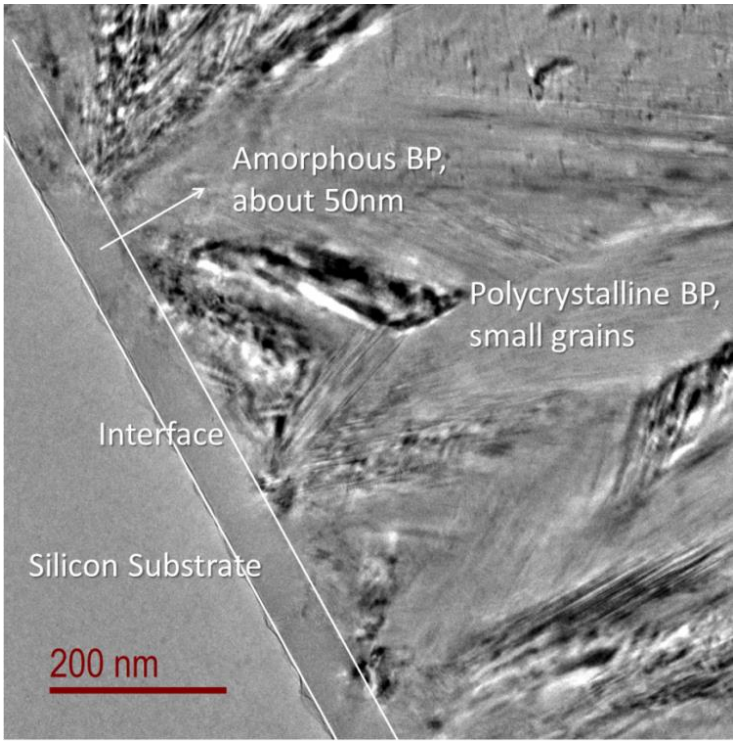

Figure 4-3. HRTEM of the BP/Si interface with microstructure identified.

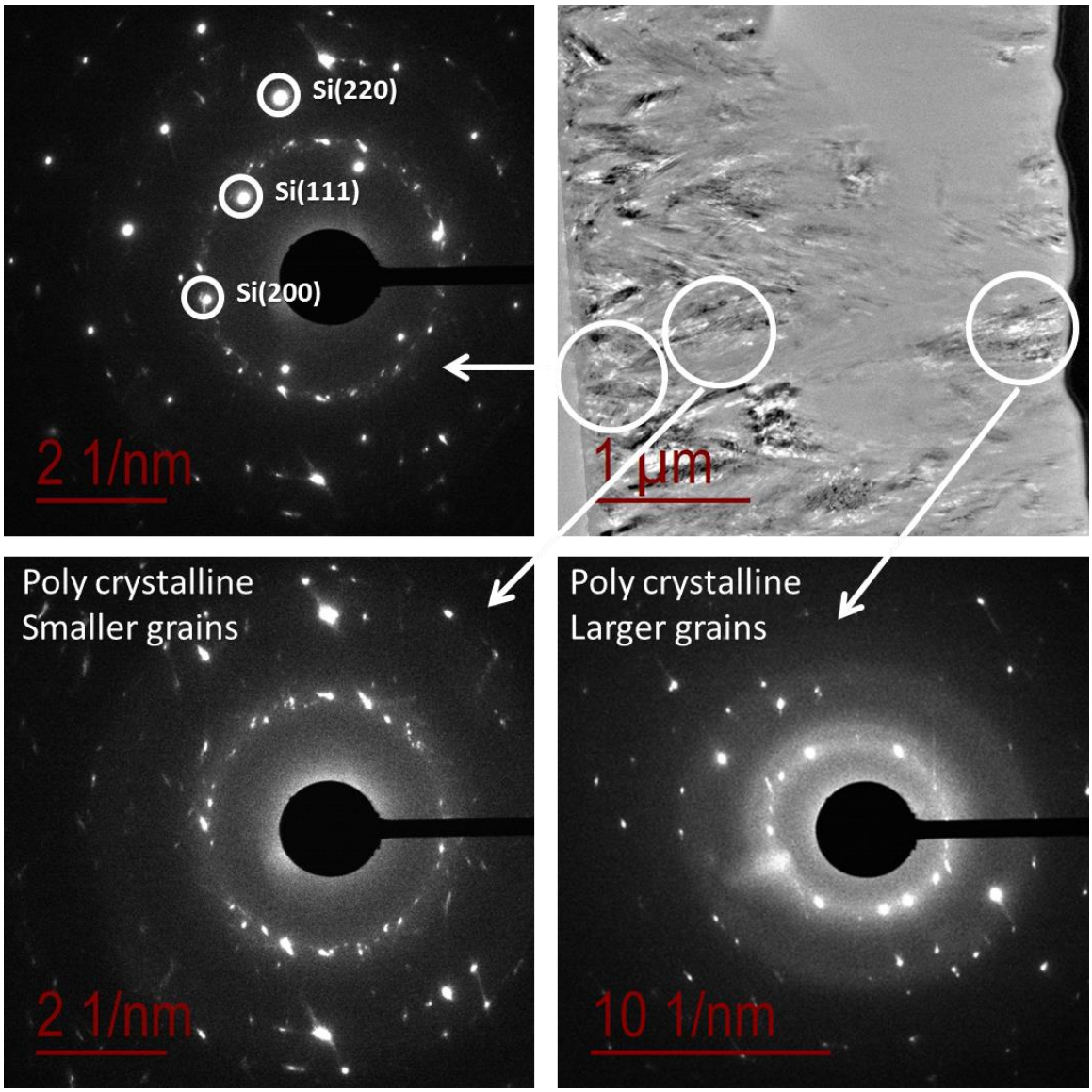

Figure 4-4. SAD results indicate a polycrystalline BP film is grown on (001) Si. The grain size varies between the interface and the surface, circles show locations only approximately.

4.2. BP growth on SiC

BP growths on SiC were systematically studied by varying growth parameters. XRD, SEM and TEM are utilized to determine the qualities of the grown films. In this sub-chapter, the suitable gas flow rate and temperature are defined; the appropriate SiC polytype is selected; the favorable polarity of SiC as well as the offcut angle is

determined. However, the surface roughness effect is not covered in this chapter since epi-ready C-face SiC wafers were not available during the period of this study. Optimized BP growth on a smooth SiC surface is reported in 4.5.

4.2.1. Gas flow rate study

A gas flow study was conducted during the first several growths and the favorable gas flow rate was defined. All depositions were conducted at around 800°C and 630Torr on C-face 4H-SiC wafers with 4° offcut along [11-20] direction. [111] epitaxial growth is expected since BP grows on the basal plane of the hexagonal SiC. According to the XRD data, there are always only BP (111) and (220) diffraction peaks in these XRD patterns. The intensity of the former peak indicates epitaxial content, while the latter represents off-axis growth which is undesirable because it might induce more grain boundaries. Therefore, the height ratio between (111) and (220) peak was used to gauge the crystal quality. Table 4-2 listed the samples included in this study. The XRD patterns of sample 31 and 36 (duplication of #31) are shown in Figure 4-5.

Table 4-2. BP/SiC samples included in the gas flow rate study.*

Sample No.	*H_2 (sccm)*	*PH_3 (sccm)*	*B_2H_6 (sccm)*	*Growth Rate (μm/h)*	*(111)/(220) Height Ratio*
28	2500	300	60	7.3	3/1
29	2500	100	10	1.9	30/1
30	2500	300	30	6.7	1/75
31	2500	100	20	5.3	40/1
34	2500	50	10	3.0	1.5/1
35	2500	100	40	10.3	2/1
36	2500	100	20	5.6	14.5/1
42	2500	100	20	4.8	13/1

*** Depositions were conducted at 800°C and 630 Torr. C-face 4H-SiC wafers with 4° offcut along [11-20] direction had been used exclusively.**

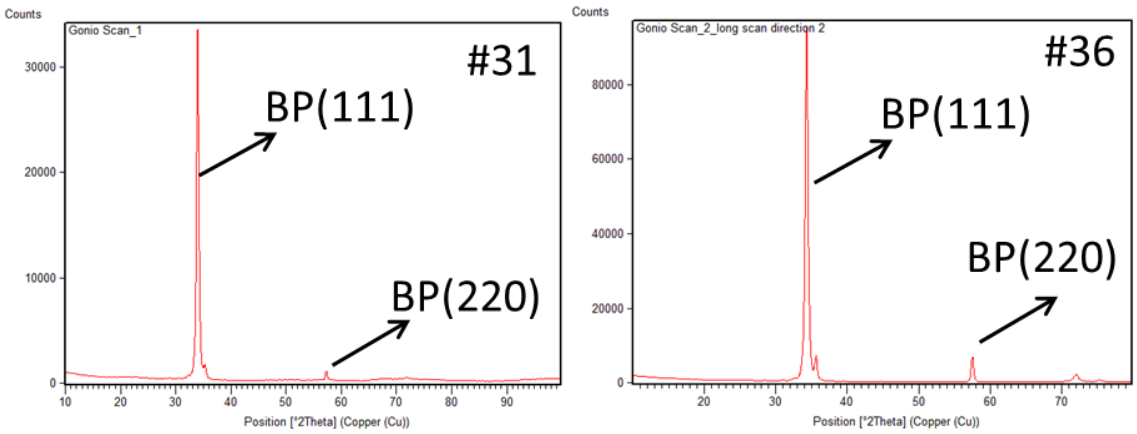

Figure 4-5. XRD examinations of sample 31 (left) and 36 (right). In either pattern, a strong BP (111) peak at 34.17° and a weak BP (220) peak at 57.33° were observed. This indicates that BP epitaxy on SiC was achieved.

By comparing the XRD results in Table 4-2, we found that sample 31, 36 and 42 give the highest (111)/(220) ratios which indicate high epitaxial contents. Therefore, the favorable flow rate should be B_2H_6 (1% in H_2) at 20 sccm and PH_3 (5% in H_2) at 100sccm. This refined flow rate combination was then used as the standard gas flow in later BP growth. The overwhelming intensities of BP (111) diffraction in sample 31 and 36 (Figure 4-4) imply that BP epitaxy on SiC was achieved. To confirm this, TEM analysis was performed.

HRTEM image and SAD pattern of the interface of sample 31 were shown in Figure 4-6. As is clearly seen, zincblende BP grows epitaxially on SiC. No amorphous structure was observed at all. The electron diffraction pattern revealed that the epitaxial relationship is (0001) <11-20>-SiC // (111) [110]-BP.

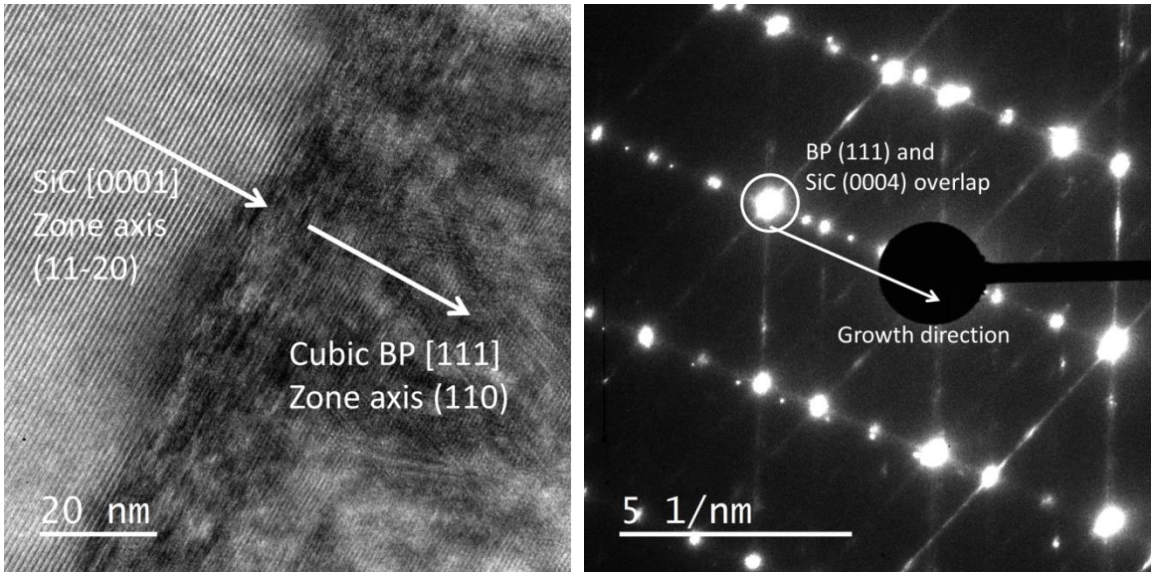

Figure 4-6. HRTEM and SAD pattern of the interface of sample 31. Epitaxial BP was obtained on top of SiC and the epitaxial relationship is (0001) <11-20>-SiC // (111) [110]-BP.

4.2.2. Substrate and interface study

As was mentioned in the introduction, SiC has three common polytypes: 3C-SiC, 4H-SiC and 6H-SiC. Lattice mismatches between the hexagonal planes of the three SiC polytypes and the (111) plane of zincblende BP are 4.5%. 3C-SiC has the same crystal structure as zincblende BP, however, the synthesis of high crystal quality 3C-SiC wafers is still a challenge. In contrast, high quality 4H-SiC and 6H-SiC wafers are now commercially available. Moreover, alteration of the offcut angle and SiC polarity can further tune the performances of these hexagonal SiC wafers when used as substrates.

To study the influences of the polytypes, offcut angles and SiC polarities on BP film growth, a series of experiments were conducted. The interface and crystal qualities of the grown film were used as criterions. Detailed results and analysis are shown in the following three small chapters under 4.2.2. To be noted, the gas flow rates were all B_2H_6 (1% in H_2) at 20 sccm and PH_3 (5% in H_2) at 100sccm.

4.2.2.1. SiC polytype and growth

3C-SiC:

BP Epitaxy was not achieved on the 3C-SiC substrate. Instead, a partial amorphous and partial polycrystalline structured BP was formed at the interface. A low magnification HRTEM image of the interface of sample 76 is shown in Figure 4-7. This fruitless growth does not mean 3C-SiC is a bad candidate for BP growth. The reason for the failure is because the quality of the 3C-SiC layer is poor. It is only 2∼3 nm thick and nonuniform. The highly magnified TEM images of the interfaces can be found in Figure 4-8. Since not many 3C-SiC sources were available and the quality are be guaranteed, we laid 3C-SiC aside and focused on the hexagonal SiC substrates.

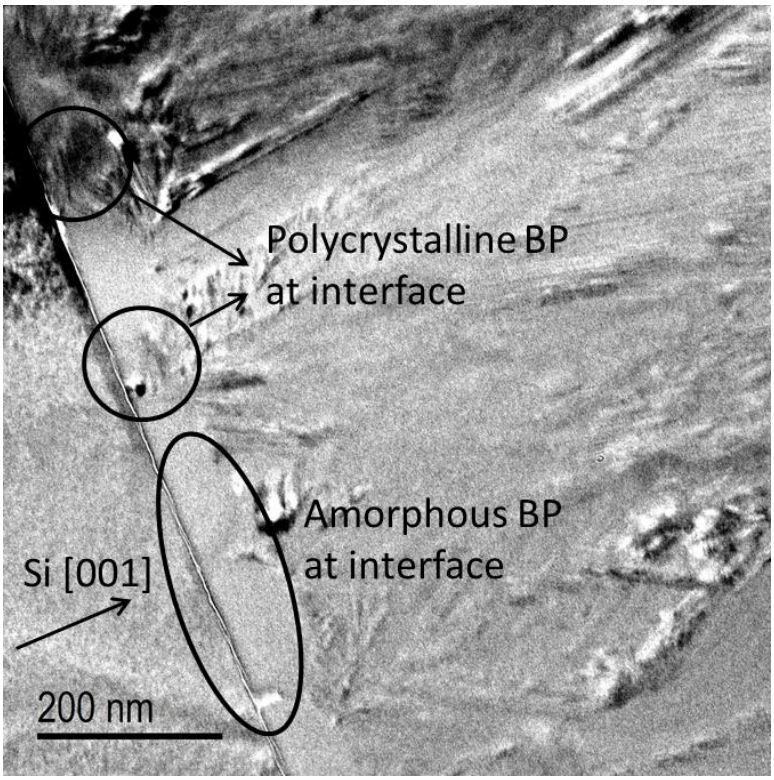

Figure 4-7. Low magnification HRTEM image of sample 76 (BP/3C-SiC). A partial amorphous and partial polycrystalline structured BP was formed at the interface.

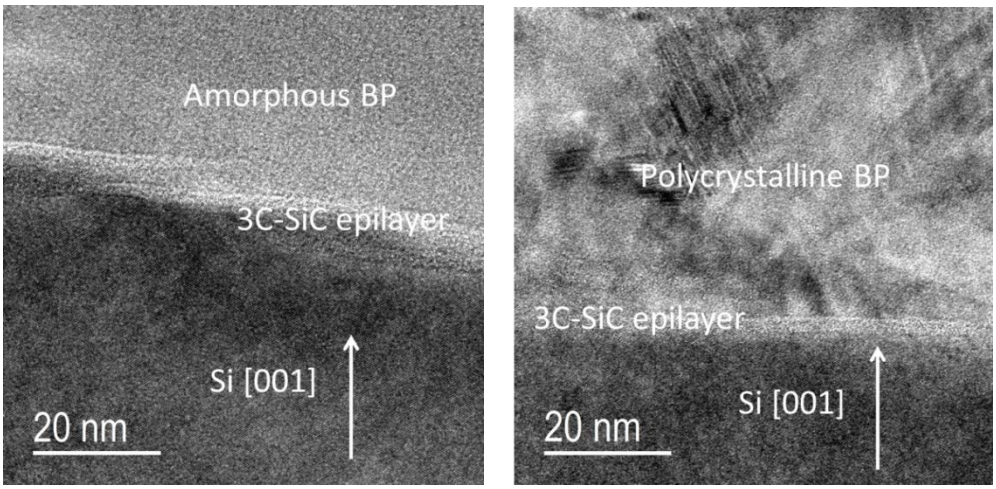

Figure 4-8. High magnification HRTEM images of sample 76 (BP/3C-SiC). Amorphous BP was grown in the left image and polycrystalline BP was grown in the right image. The surface of Si is rough, therefore, the quality of the subsequent 3C-SiC epilayer is poor.

6H-SiC:

A HRTEM image of the epitaxial interface of sample 63 (BP/6H-SiC) is shown in Figure 4-9. Obviously, BP epitaxy was achieved as well. However, the XRD results (see 4.2.2.2) are not exciting. Moreover, the options we have for tuning the growth are limited because Cree. Inc does not provide 6H-SiC wafers with offcut angles.

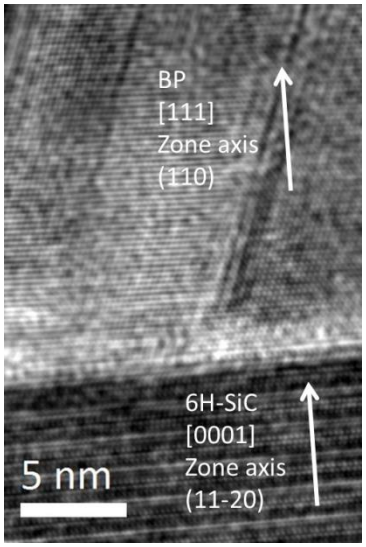

Figure 4-9. HRTEM image of the epitaxial interface of sample 63 (BP/6H-SiC).

4H-SiC:

As indicated in the gas flow rate study, high quality epitaxial BP was successfully grown on 4H-SiC (Figure 4-6). This progress made us confident that 4H-SiC is an appropriate substrate for BP epitaxy. We are then motivated to pursue the best growth parameters to optimize the film quality on 4H-SiC.

After weighing up the pros and cons, 4H-SiC was determined to be the most appropriate substrate and it should be worth more efforts.

4.2.2.2. SiC polarity and growth

Theoretically, the polarity vector for a covalent compound points from the more electronegative element to the less electronegative one. Since the electronegativity for Si, C, B and P is 1.90, 2.55, 2.04 and 2.19, respectively, the polarity for SiC is Si→C and for BP is B→P. Figure 4-10 shows the atomic model for BP grown on C-face SiC as well as Si-face SiC.

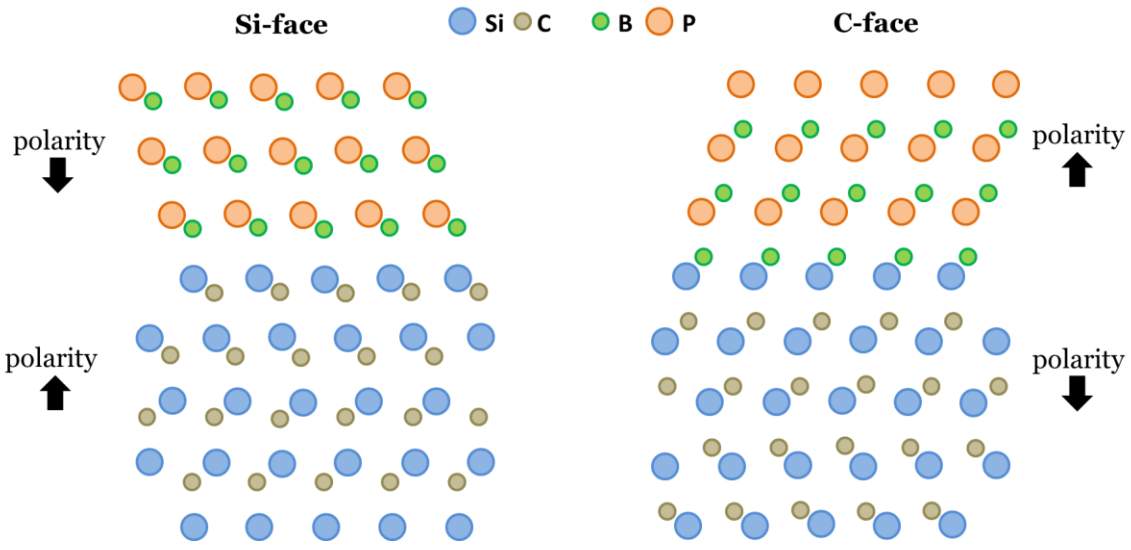

Figure 4-10. Atomic models for BP epitaxy on C-face SiC as well as Si-face SiC.

It has been reported that the polarity of SiC would affect the diffusion length of the adatoms on the surface of the substrate, [58] which is directly linked to the interface quality and further film growth. Therefore, the appropriate SiC polarity has to be identified to facilitate BP epitaxial growth. Experiments were then conducted to study the influences of the SiC polarities on film growth. The results are summed up in Table 4-3. Sample 63 and 65 are grown on C epi-ready and Si epi-ready 6H-SiC on-axis wafers, respectively. This controlled experiment is especially designed to find out the favorable SiC polarity of BP growth. Sample 51 is grown on a Si epi-ready 4H-SiC wafers with a 4° offcut along the [11-20] direction, while sample 31 is actually grown on the backside of the wafer used for sample 51, therefore, sample 31 is C-face with a relatively rough surface. Though sample 51 and 31 are not pre-designed for the SiC polarity study, the comparison between them is still quite instructive and can serve as supplementary results.

Table 4-3. Information summary of the SiC polarity study.

Sample No.	*Polytype*	*Offcut angle (°)*	*Terminated face*	*Growth Rate (μm/h)*	*Deposition Temp (°C)*	*(111)/(220) Ratio*	*Epitaxy?*
51	4H-SiC	4	Si	6.0	800	1/1.2	-
31	4H-SiC	4	C	5.3	800	40/1	Yes
65	6H-SiC	0	Si	5.4	850	1.6/1	No
63	6H-SiC	0	C	5.1	850	3/1	Yes

The two groups of experiments listed in Table 4-3 clearly reveal the preference of BP growth. The (111)/(220) ratio of sample 31 is much higher than that of sample 51. This means sample 31 has a high epitaxial content, while sample 51 is likely to have the similar structure shown in Figure 4-3. It seems that the effect of the SiC polarities weighs more than that of the surface roughness in BP growth. Sample 63 and 65 were rigorously controlled experiments to study the SiC polarity effects. SEM, XRD and TEM were all utilized to analyze the film. The results are shown in Figure 4-11. Again, C-face SiC is found to be superior for BP growth.

Figure 4-11 (a) and (b) are SEM images of the surfaces of sample 63 and 65, respectively. The densely distributed small pyramid structures observed in sample 63 indicate that BP grows mainly in the epitaxial direction [111] which has a three-fold symmetry. While the features on the surface of sample 65 looks more randomly orientated. The XRD results in Figure 4-11 (c) and (d) further confirmed this. The XRD pattern of sample 63 has a (111) dominant peak and a minor (220) peak, all the other diffraction peaks except the 6H-SiC (0001) peak at 35.4° are neglectable. This means that the BP film prefers to grow epitaxially on the SiC (0001) basal plane in [111] direction. However, the XRD pattern of sample 65 shows a random polycrystalline character because the (111), (200) and (220) peaks are all very low and comparable. The evidences are shown in Figure 4-11 (e) and (f). The interface structures were directly imaged by the TEM. Sample 63 is epitaxial, while sample 65 has a 60~70nm amorphous layer formed on the substrate and then a polycrystalline BP film was grown on top of that. The "two-step" growth of sample 65 also explains its XRD result, because the polycrystalline film was nucleated from an amorphous layer which has non-preferred orientations.

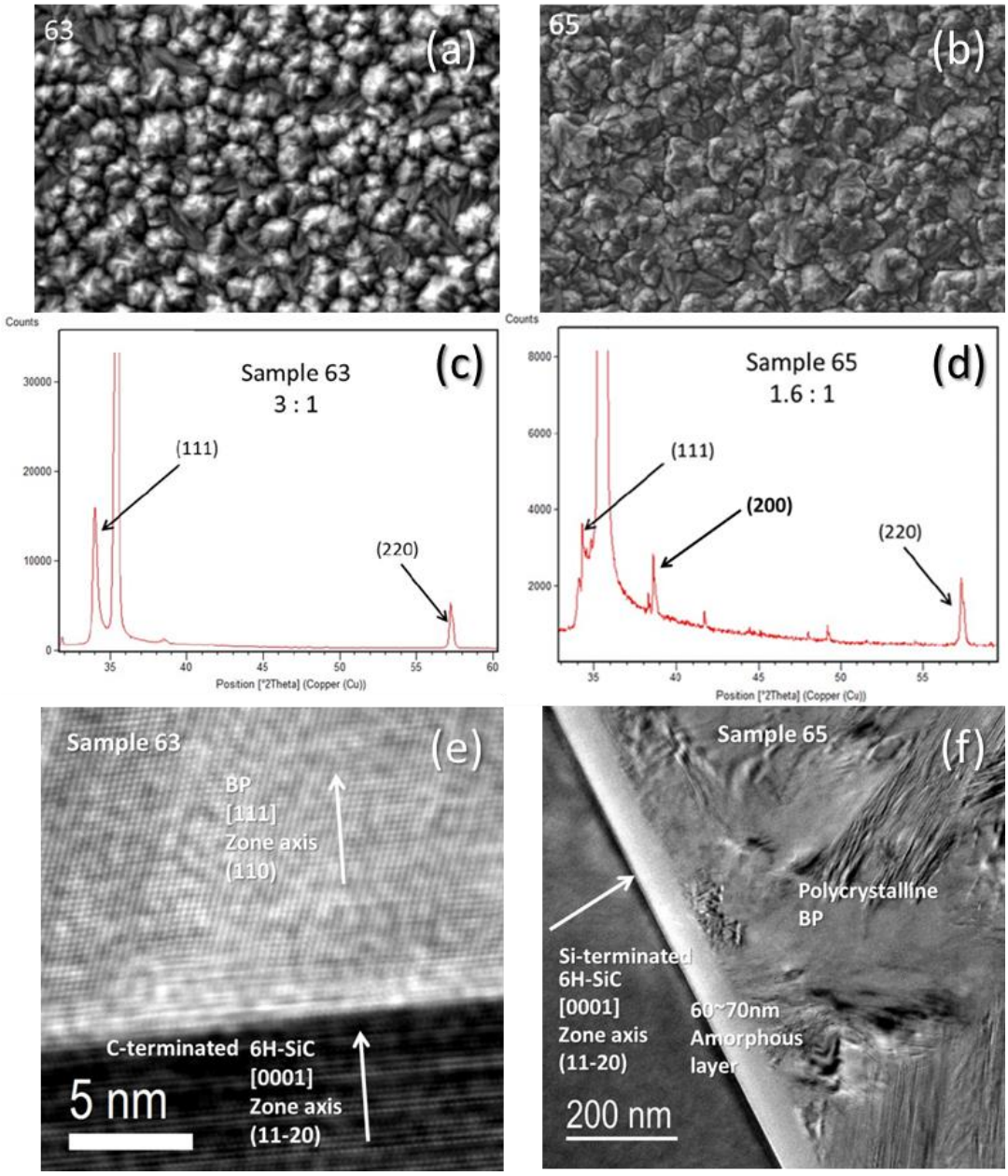

Figure 4-11. SEM, XRD and TEM comparisons of sample 63 (C-face) and sample 65 (Si-face). (a) and (b) are SEM images of the surface of the samples, the densely distributed pyramid structures indicate that sample 63 has more [111] growth. (c) and (d) are XRD diffraction patterns, still sample 63 seems to be more epitaxial and sample 65 looks like random polycrystalline. (e) and (f) are HRTEM images of the interfaces. Sample 63 shows epitaxial growth while sample 65 has amorphous BP formed at the interface.

In conclusion, C-face SiC substrate is more suitable for BP epitaxy.

4.2.2.3. SiC offcut angle and growth

Tsunenobu Kimoto tried SiC homoepitaxy on 6H-SiC with different offcut angles and he found that offcut angles are associated with the growth mode and thereby affect the film morphology in the initial stage. [58] To find out an appropriate offcut angle, 4H-SiC substrates with 4° and 8° offcut angles (toward the [11-20] direction) were both employed for BP growth. The film qualities are compared and the details are listed in Table 4-4. The XRD and TEM analysis are summed in Figure 4-12 and Figure 4-13, respectively. Note that still, all the substrates in this study are C-faces, that are, the backside of the Si epi-ready wafers.

Table 4-4. Information summary of the SiC offcut angle study.

Sample No.	***Polytype***	***Offcut angle (°)***	***Growth Rate (μm/h)***	***Deposition Temp (℃)***	***(111)/(220) Ratio***	***Epitaxy?***
31	4H-SiC	4	5.3	800	40/1	Yes
50	4H-SiC	8	5.7	800	1/2	No
45	4H-SiC	4	5.4	850	94/1	Yes
53	4H-SiC	8	5.6	850	1/6	No
61	4H-SiC	4	2.9	950	202/1	Yes
67	4H-SiC	8	5.0	950	5/1	Partial

According to the XRD patterns, all the film grown on the 4° offcut SiC wafers (sample 31, 45 and 61) show very strong BP (111) diffraction peaks at 34.17° and no other diffractions are comparable to it. This indicates good BP epitaxy. In contrast, the 8° offcut SiC wafers (sample 50, 53 and 67) are disappointing. In either sample 50 or 53, instead of (111) diffraction, the (220) diffraction dominates. This peak intensity reversions plus the emergences of the (113) peaks imply that the films are probably nucleated from amorphous layers. Sample 67 improved a lot if compared with sample 50 and 53, this is probably due to the temperature adjustment. But it is still far below the standard the 4° offcut SiC wafers reached. The following TEM analysis clearly demonstrates what happened at the interfaces.

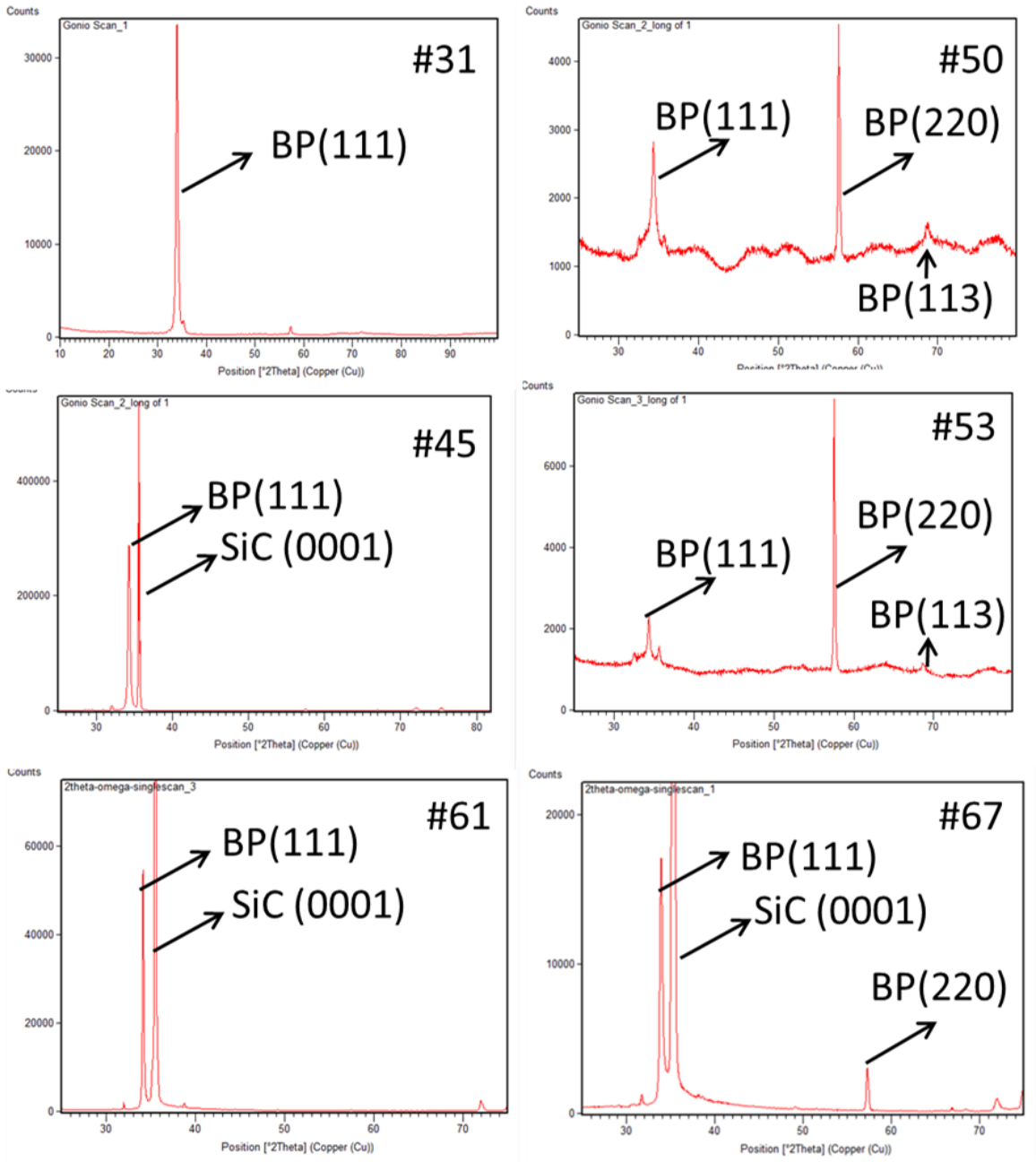

Figure 4-12. XRD examinations of the samples of the offcut angle study. Apparently, film grown on the 4° offcut wafers all have a large epitaxial component since the XRD patterns are all dominated by the BP (111) diffractions. However, the 8° offcut wafers do not yield epitaxial growth. Note that sample 67 performs better than sample 50 and 53, this should be due to the temperature adjustment. TEM analysis will be necessary.

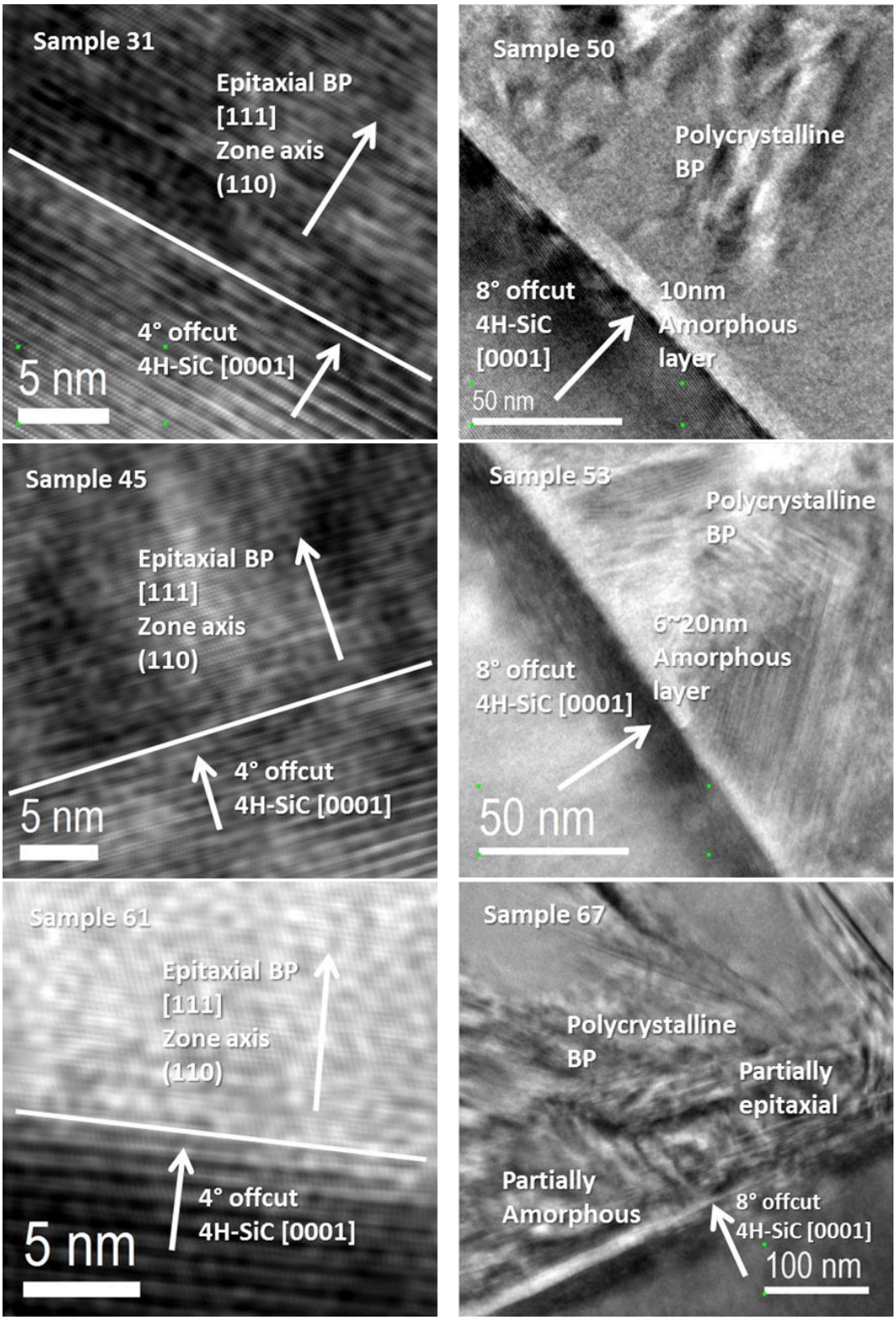

Figure 4-13. TEM examinations of the samples of the offcut angle study. Sample 31, 45 and 61 all show successful BP epitaxy. Both sample 50 and 53 have amorphous layers at the interface. The interface of sample 67 is partially amorphous and partially epitaxial.

The TEM investigations are consistent with the previous speculations. As were shown in Figure 4-13, all three of the 4° offcut SiC wafers yield good BP epitaxy, while the 8° offcut SiC wafers lead to the formation of amorphous structures at the interface. Though amorphous layers were observed on all three 8° offcut SiC wafers, their thicknesses and distributions differ. In sample 50, the amorphous layer is 10nm thick and it uniformly covers the whole SiC substrate. Sample 53 also has a thin amorphous layer, but it is not as uniform. The thickness ranges from 6nm~20nm. On sample 67, the interface becomes partially amorphous and partially epitaxial. This decent improvement should be considered as a result of the temperature adjustment. It seems that the quality of the film grown on the 8° offcut SiC wafer improves when the deposition temperature increases, however it is still not comparable to what we have achieved on the 4° offcut SiC wafers.

It can be concluded from these experimental results that the most favorable substrate for BP growth is C-face 4H-SiC with 4° offcut.

4.2.3. Temperature study

Temperature is always a crucial factor in thin film industry not only because it affects the film quality significantly but also because it is closely related to the feasibility and the cost. Therefore, a temperature study is imperative.

A serial experiment was performed to investigate the temperature influences on the film growth. The temperature ranges from 800°C to 1000°C with the interval of 50°C. All the other parameters used in this study were previously optimized parameters and kept the same. To be specific, the five growths were completed on the C-face 4H-SiC substrates with 4° offcut and the gas flow rates were B_2H_6 (1% in H_2) at 20 sccm and PH_3 (5% in H_2) at 100sccm. The information summary of temperature study is presented in Table 4-5. Note that the 4H-SiC wafers used in this study are from new batches; therefore, the small variation of the XRD data compared with that of the early studied samples is acceptable.

Table 4-5. Information summary of the temperature study.

Sample No.	*Deposition Temp (°C)*	*Growth Rate (μm/h)*	*(111)/(220) Ratio*	*Epitaxy?*
81	800	5.6	6/1	Yes
80	850	4.7	15/1	Yes
82	900	4.7	19/1	Yes
83	950	4.3	42/1	Yes
84	1000	2.0	4/1	No

Briefly speaking, BP films grown at 800°C-950°C are all epitaxial. However, the crystal quality of these epitaxial films varies with temperatures. At 1000°C, a thick amorphous layer was deposited first and then crystalline BP formed on top of that. Detailed XRD, SEM and TEM examinations are performed on each of the samples. The results are shown in the following three small chapters respectively.

4.2.3.1. XRD examination

As was mentioned, the epitaxial relationship is 4H-SiC (0001), [11-20] // FCC BP (111), [1-10]. Perfect epitaxial growth should give us a single sharp BP (111) peak in the XRD pattern. However, there is always a small BP (220) peak in our XRD data. This non-epitaxial orientation is undesired because it creates grain boundaries with the epitaxial orientation. Therefore, (111)/(220) ratio in XRD pattern can serve as a straightforward criterion to roughly evaluate the crystal quality. Figure 4-14 is the plot of (111)/(220) ratio versus temperature. Figure 4-15 listed the XRD patterns of all the five samples.

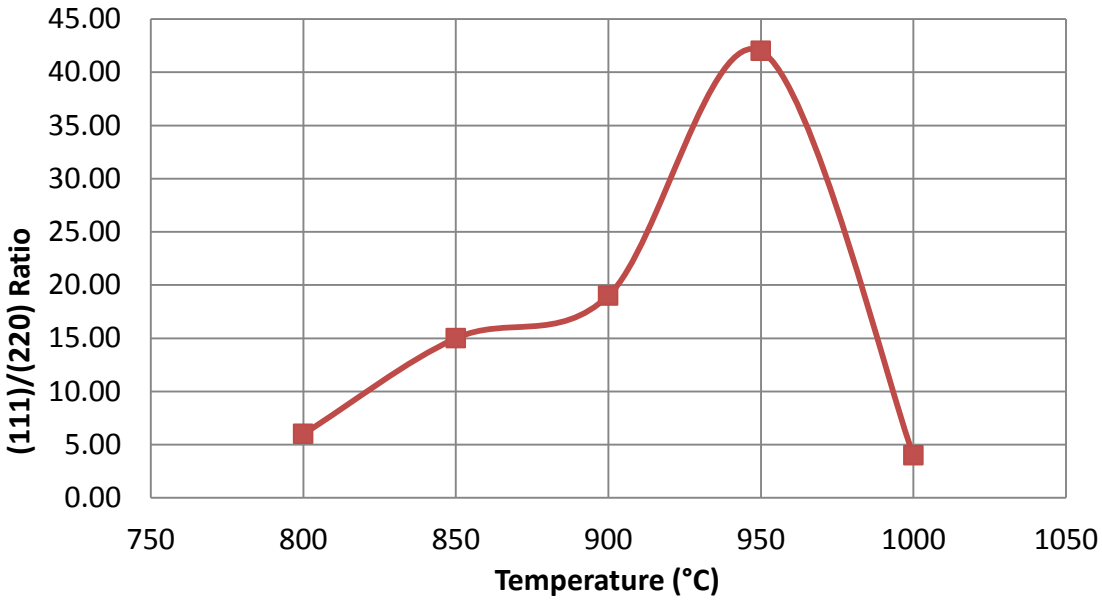

Figure 4-14. Plot of (111)/(220) ratio versus temperature. 950°C seems to be the best growth temperature. More careful investigations of the film are needed to confirm this.

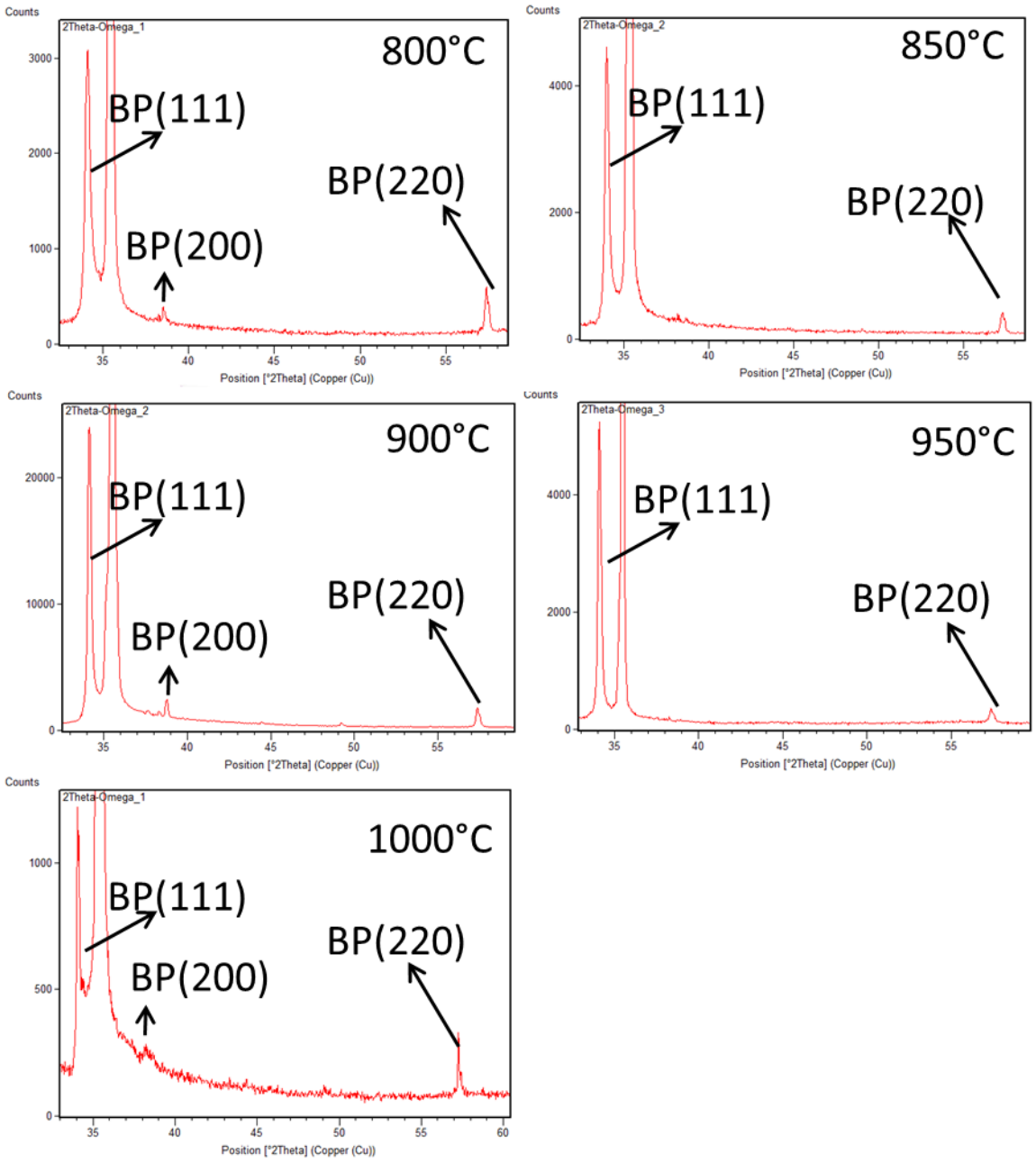

Figure 4-15. XRD examinations of the temperature study. The BP film grown at 950°C has highest epitaxial content. 850°C and 900°C gives about the same (111)/(220) ratio, however, the later also causes an non-neglectable amount of (200) orientations which have the potential of inducing more grain boundaries. 800°C, if compared with the other three temperatures, is also unsatisfactory. 1000°C causes randomly crystal growth.

The plot in Figure 4-14 directly reveals the relationship between epitaxial quality and growth temperature. 950°C is the best growth temperature according to the plot. This is also consistent with the previous experiments (sample 61) performed at 950°C in which a (111)/(220) ratio as high as 202/1 was achieved. Figure 4-15 show the XRD patterns of all the five samples of the second temperature study. The BP film grown at 950°C has the highest epitaxial content. 850°C and 900°C gives about the same (111)/(220) ratio, however, the later also causes an non-neglectable amount of (200) orientations which have the potential of inducing more grain boundaries. Growth at 800°C, compared with the other three temperatures, is unsatisfactory. Apparently, the quality of the epitaxial films degraded collectively compared to previously studied samples such as #31(800°C), #45(850°C) and #61(950°C). We attribute this to the variation of the SiC wafer qualities since a new batch of wafers were employed after sample #68. The BP film grown at 1000°C seems to be an exception. It shows a random polycrystalline character. Since 1000°C is close to the reported melting temperature (1100°C) of BP, it is highly possible that the BP nucleation and decomposition processes occurred simultaneously. The relatively slow growth rate supports this speculation.

XRD examination reveals whether the film is epitaxial or not, SEM and TEM investigations are needed to confirm and visualize the film qualities.

4.2.3.2. SEM examination

All films have thicknesses ranging from 2.5μm to 3.0μm except the one grown at 1000°C, which basically has no BP coverage on the substrate. Compared with the ultimate thickness requirement of 200μm, what we have achieved should be regarded as an early stage and the surface morphology can be used to predict further growth. An SEM study on the surface morphologies of all the samples was performed. Figure 4-16 listed the SEM images of the surfaces of five samples. The magnifications are all 30K.

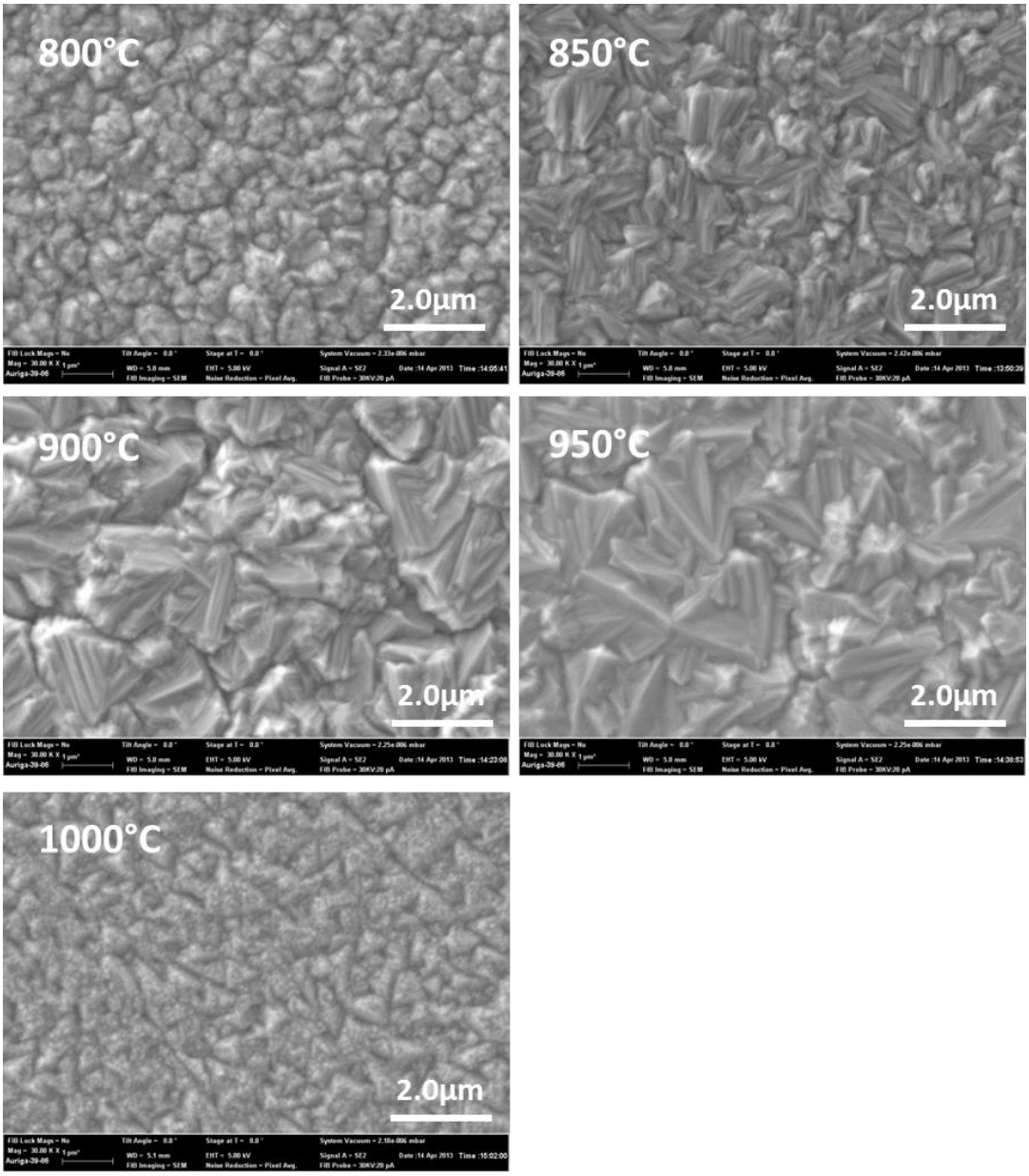

Figure 4-16. SEM examinations of the temperature study. The grains of the 800°C sample exhibit a circular morphology which indicates a large amount of non-epitaxial content at the surface. The grains of the 850°C, 900°C and 950°C samples all look triangular, which means BP [111] is still the dominating orientation near the surfaces of the three sample. The 1000°C sample shows no crystalline character, it is probably just a thin amorphous layer.

The results of the SEM examinations are in agreement with the previous XRD studies. The surface of the 800°C sample show fine grains with an average size of

approximately 0.5μm. These grains exhibit a circular morphology which indicates a large amount of non-epitaxial content at the surface. 850°C, 900°C and 950°C samples all have more triangular morphology which indicates more epitaxial growth. But the rough surface also indicates many other growth orientations occurred at the same time and competed with epitaxial growth. Note that the grain size of the 850°C sample is about half that of the other two which means there are more nucleation sites formed at 850°C. While the 1000°C sample shows no crystalline characters at the surface. It is probably just a thin amorphous layer sitting on top of the substrate.

The SEM images in Figure 4-16 are taken in the regions where the films grow continuously. However, for the samples grown at temperature above 850°C, we did not obtain full coverage due to the insufficient deposition time. Some of the crystal islands were just nucleated and still isolated from the others, while some of them coalesced but did not join the continuous film. These cases enabled us to study the initial stage of the film growth as well as the grain boundary formation mechanism. The 850°C (sample 80) and 950°C (sample 83) samples were chosen for comparison.

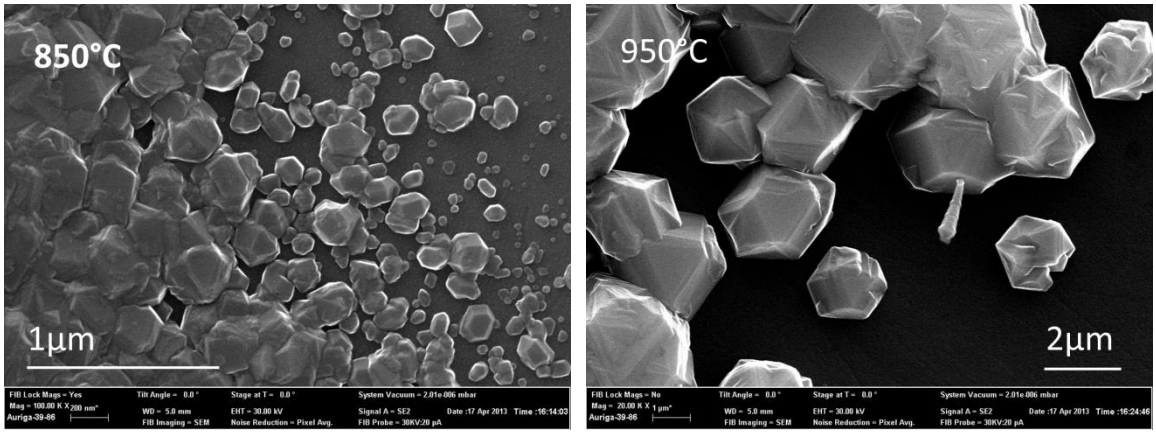

Figure 4-17. SEM Comparison of between the nuclei formed at 850°C and 950°C. The average nucleus size of the 850°C sample is smaller. It is consistent with what was concluded from Figure 4-16.

The nucleus size was compared in Figure 4-17. The images were taken near the border of the continuous films. Apparently, the 950°C sample has fewer but much larger nuclei compared to the 850°C sample. This is consistent with what we concluded from Figure 4-16.

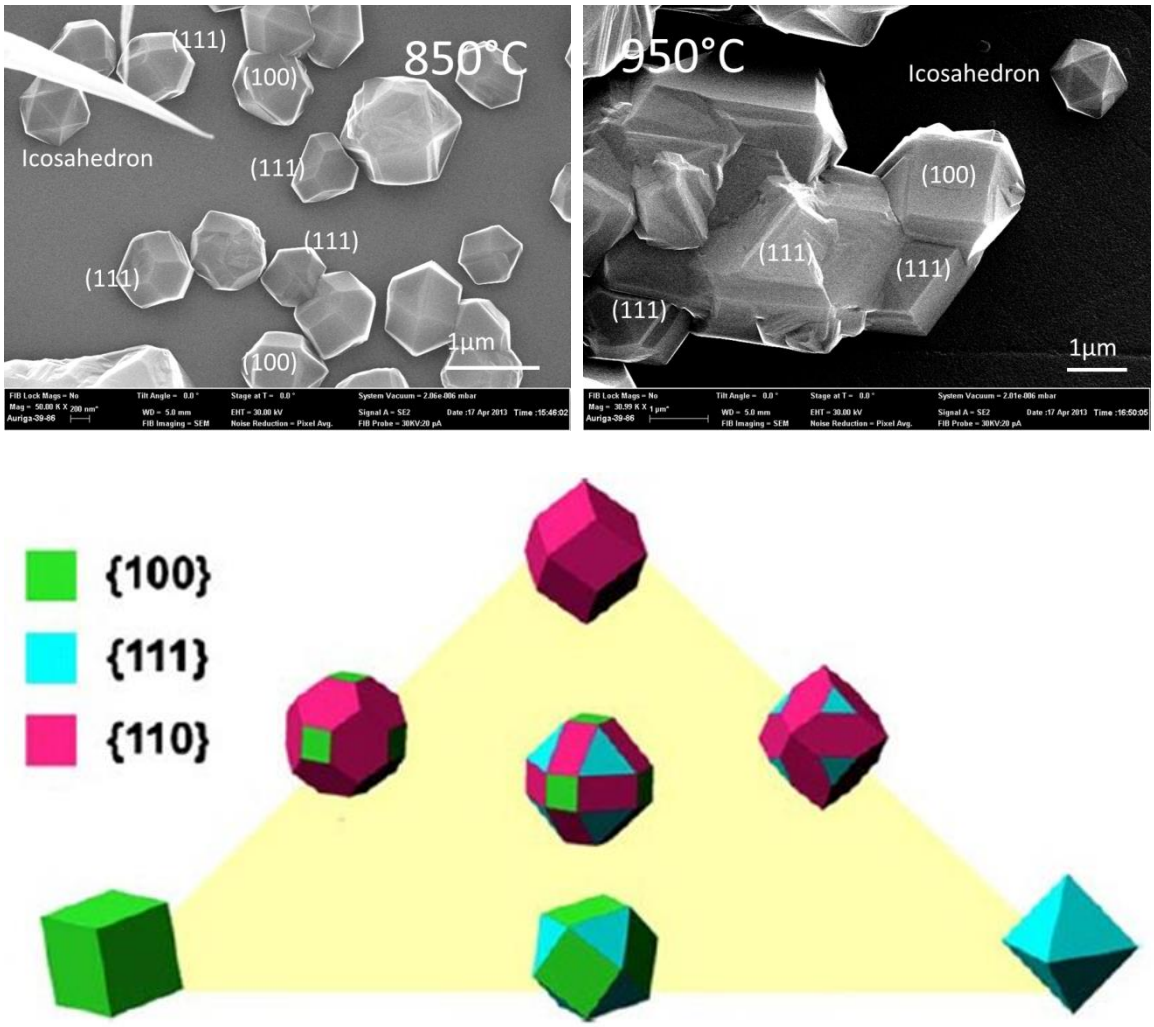

Figure 4-18. SEM images of the crystal islands of the 850°C (sample 80) and 950°C (sample 83) samples. Some of the facets are labeled. The model below illustrates the common geometry of FCC singlecrystalline nanocrystals. [47]

The SEM images in Figure 4-18 shows that the BP nuclei have many kinds of shapes. The facets can be indexed according to the following geometrical models of typical

FCC single-crystalline nanocrystals. [47] Most of the BP nuclei have hexagonal or triangular facets facing normal which suggests [111] growth direction. This means epitaxial growth occurred at these sites. The rectangular facets indicate (100) atomic planes. Note that they are not perpendicular to the page even though they seem to be. In both of the images, we observe icosahedral nanocrystals. It is caused by multiple twinning of (111) facets. Here, we only show the trend of the temperature effects on number of nucleation sites and the size of the crystal islands. More detailed studies on the shapes and formation mechanisms were also done. The results and discussions were organized and will be presented in sub-chapter 4.4.

In summary, the 800°C sample does not look quite epitaxial. TEM is needed to verify whether epitaxy occurred at the interface. In comparison, the film grown in the temperature range of 850°C-950°C has more epitaxial content. Furthermore, the grain size of the film tends to increase as the temperature increases within the 800°C-950°C range. At 1000°C, a uniform amorphous layer was formed and a few inhomogeneous nucleation occurred on top of that. Since neither of the 1000°C processed samples yields good results, higher temperatures will not be attempted.

4.2.3.3. TEM examination

TEM was also employed to investigate the interface between BP and SiC. High-resolution imaging and electron diffraction make the direct observation of the crystal quality available.

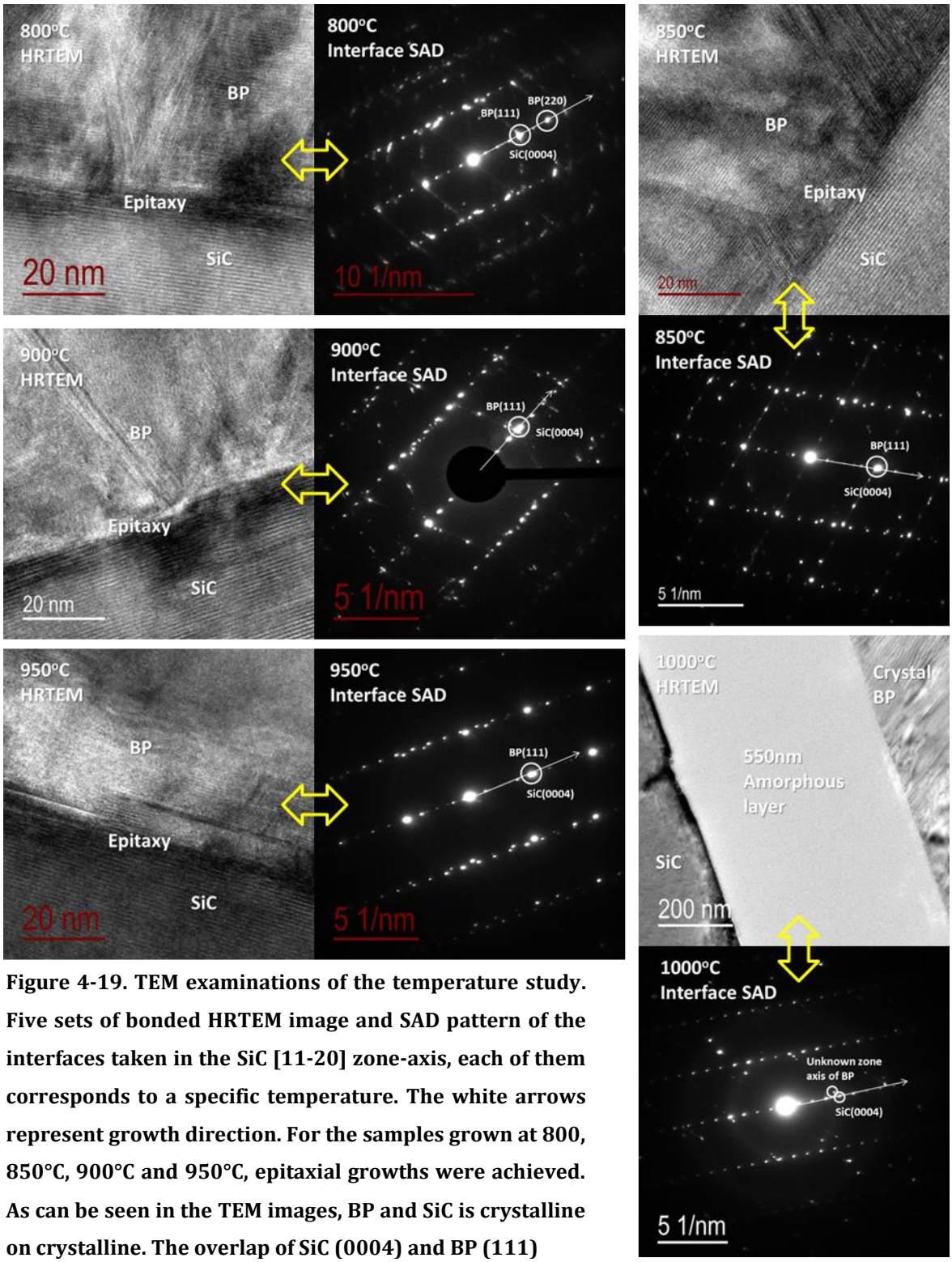

Figure 4-19. TEM examinations of the temperature study. Five sets of bonded HRTEM image and SAD pattern of the interfaces taken in the SiC [11-20] zone-axis, each of them corresponds to a specific temperature. The white arrows represent growth direction. For the samples grown at 800, 850°C, 900°C and 950°C, epitaxial growths were achieved. As can be seen in the TEM images, BP and SiC is crystalline on crystalline. The overlap of SiC (0004) and BP (111) diffraction spots is another evidence of epitaxy. While the 1000°C sample has a thick amorphous layer formed before crystalline BP starts to grow. The orientation of the BP crystalline is unknown.

Figure 4-19 shows five sets of bonded HRTEM image and SAD pattern of the interfaces taken in the SiC [11-20] zone-axis, each of them corresponds to a specific temperature. The zone axes are all SiC [11-20]. The white arrow in each SAD pattern represents growth direction. For the samples grown at 800, 850°C, 900°C and 950°C, epitaxial growths were achieved. As can be seen in the TEM images, BP and SiC is crystalline on crystalline. The overlap of SiC (0004) and BP (111) diffraction spots is another evidence of epitaxy. However, the epitaxy quality varies with temperatures if we examine the diffraction patterns carefully. The 800°C sample has obviously two orientations dominating the growth since there is BP (111) as well as a BP (220) diffraction spot along the growth direction. Furthermore, the extra diffraction spots which does not belong to singlecrystalline BP [110] diffraction and the widespread diffuse streaks indicate grain boundaries and planar defects. This matches well with the XRD data. The 850°C sample, compared with the 800°C one, is much better. The diffraction pattern is well defined. More details of the diffraction patterns will be discussed in 4.3. The 900°C sample looks similar to the 800°C one except for the absence of BP (220) spots. The 950°C sample shows a large improvement comparatively. The diffraction pattern of it looks like single-crystalline BP on SiC. It should have much better crystal quality than all the above-mentioned samples. The 1000°C is disappointing since it has a thick amorphous layer formed before crystalline BP starts to grow in random orientations. The orientation of the BP crystalline is unknown because it nucleated on an amorphous layer which has no periodical lattice planes for the atoms to arrange on.

To sum up, 950°C is the most suitable temperature among the five selected temperatures for BP epitaxial growth on SiC.

4.2.4. Summary

To sum up, epitaxial BP growth is achieved on SiC. The favorable gas flow rate is B_2H_6 (1% in H_2) at 20 sccm, PH_3 (5% in H_2) at 100sccm and pure H_2 at 2500sccm. The favorable growth temperature is 950°C. Further tunings should be possible. 4H-

SiC with 4° offcut along the [11-20] direction and C-face is considered to be the most suitable substrate at hand; C-face epi-ready 4H-SiC with 4° offcut was used for growth at the end of this work, the results will be presented in 4.5.

4.3. Characterization of epitaxial BP on SiC

As was mentioned in the introduction, the large thickness requirements for neutron detector materials call for fast film growth. Therefore, the types, distribution and density of defects are important. Sample 45 (grown at 850°C) was one of the earliest epitaxial samples we grew and both XRD and TEM investigations revealed its epitaxial character. Hence, a thorough defect characterization was done on sample 45. Figure 4-20 is an overview bright-field STEM image of the BP film cross-section prepared via FIB. As we can see in the image, the near interface region (< 1.5μm) has black contrast, while the upper part of the film (>1.5μm) has more white contrast. This actually means BP grows epitaxially from the interface but deviates from epitaxial growth to some extent as the film grows. Because the crystal near the interface is in zone-axis due to its epitaxial character, therefore, more electrons are diffracted and the resulted signal deficiency in this region is then observed as black contrast. Vice versa is the explanation for the white contrast of the upper part of the film. This explains the rough morphology of the surface. Detailed film analysis is shown in the following small sub-chapters.

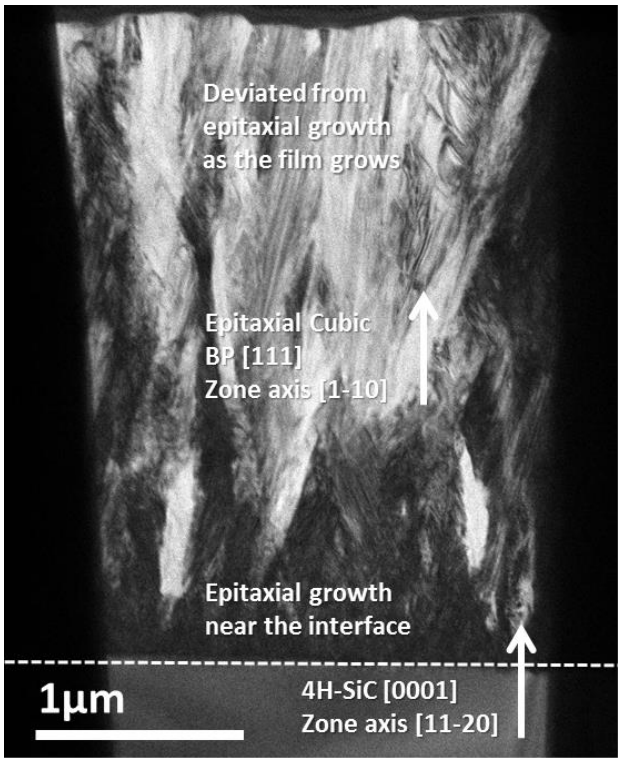

Figure 4-20. An overview STEM bright-field image of the BP film cross-section prepared via FIB. The contrast change along the growth direction means that BP grows epitaxially from the interface and deviates from epitaxial growth to some extent as the film grows.

4.3.1. Structural and elemental analysis

As was summarized in chapter 2, most of the published BP film characterizations were limited to either the surface or the interface. Whole film examination was never done before, therefore the reported high-quality film is questionable. To completely reveal every detail of our epitaxial BP film, a thorough film examination including structural and elemental analysis is performed utilizing SAD, TEM, diffractograms and EELS.

4.3.1.1. SAD analysis

SAD is a common tool to for crystal structure analysis. The epitaxial relationship and structural evolution of the whole BP film are determined by analyzing the SAD

patterns across the whole film. The SAD aperture diameter is approximately 850nm and all the SAD patterns are taken in [11-20] zone-axis of SiC. The results are shown in Figure 4-21 where the approximate regions that contributed to the diffractions are indicated by a circle in the HRTEM image. While details of the diffraction pattern analysis will be discussed in the following text, the following sequence will serve as an overview:

(a). 4H-SiC and BP interface: The diffraction pattern reveals that the epitaxial relationship of zincblende BP with SiC is SiC (0001), [11-20] // FCC BP (111), [1-10]. The mirrored diffractions and diffuse streaks in the SAD pattern indicate the presence of twins and (111) planar defects.
(b). Near-interface region (<1μm): Still, the mirrored diffractions and diffuse streaks indicate the presence of twins and (111) planar defects in zincblende BP.
(c). Mid-film region (~1-2μm): The intensity difference between the mirrored diffraction and the original implies that one orientation prevails over the other. The reduced diffuse streak intensity means the planar defects decreased. The extra spots which do not belong to BP [1-10] diffraction indicate the presence of grain boundaries.
(d). Near-surface region (~2-3μm): The absence of mirrored diffractions means there is no twin boundaries in this region. The reduced intensity and length of the diffuse streaks indicate a decreased amount of planar defects. Grain boundary is the main defect near the surface.

Note that the so-called (111) planar defects basically refer to the stacking faults and dislocation loops lying within the (111) closed packed planes.

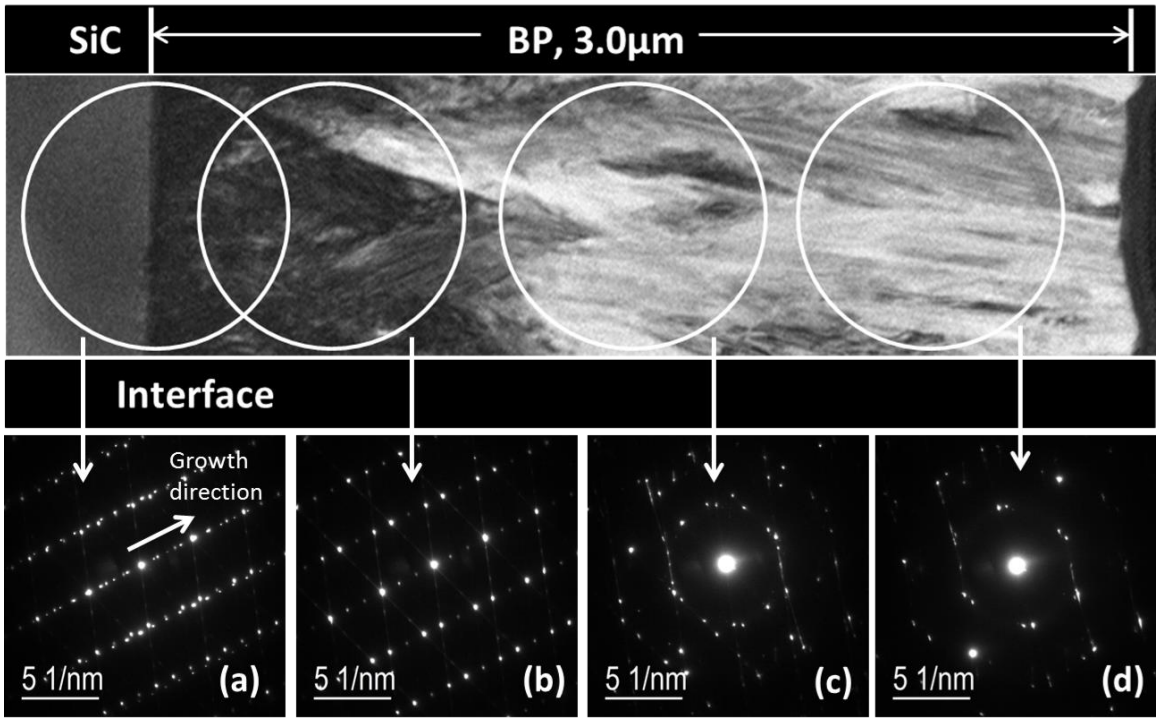

Figure 4-21. Sequential SAD patterns throughout the epitaxial BP film. Figure 4-21(a) is the overlap of 4H-SiC and zincblende BP diffraction pattern which reveals their epitaxial relationship. (b), (c) and (d) together illustrate the structure evolution: Twins and (111) planar defects dominate the near-interface region and decrease along the growth direction. Grain boundary starts to emerge in the middle, and then becomes the main defect in the near-surface region. The BP film can be described as crystalline with different types of defects along the growth direction.

The structure evolution can be summarized as: Twins and (111) planar defects dominate the near-interface region and decrease along the growth direction. Grain boundaries start to emerge in the middle, and then becomes the main defect in the near-surface region. This is consistent with what was stated in Figure 4-20. Moreover, the grain size gets larger as the film grows because the number of diffraction spots decreases. The film can be described as zincblende BP crystalline with different types of defects along the growth direction.

4.3.1.2. TEM and diffractogram analysis

The SAD experiment gave an overview of the film evolution. HRTEM was then performed to investigate the microstructure evolution and defects at the atomic level. Figure 4-22 (a) shows a series of high-resolution electron micrographs of the film in SiC [11-20] zone-axis with diffractogram analysis showing the evolution of the microstructure in the near-interface region (<500nm). With this approach we are able to examine with higher resolution the defect evolution within the perfect epitaxial region. The results indicate that the evolution of the film near the interface is the following:

1. Interface between SiC and zincblende BP with twins and planar defects.
2-3. Zincblende BP with twins and small-size planar defects.
4. Zincblende BP with fewer twins and large-size planar defects.
5. Zincblende BP with large-size planar defects.

The first four HRTEM images in Figure 4-22 (a) combined with their corresponding abnormal diffractograms reveal the fact that the pyramid structures which locate near the interface are closely related to the twin boundaries and planar defects. The pyramidal morphology is due to the crosses of the (111) atomic planes of the mutually twinned grains. The fifth HRTEM image in which no pyramid structures were observed appears less defective. It generates a typical BP [110] diffractogram.

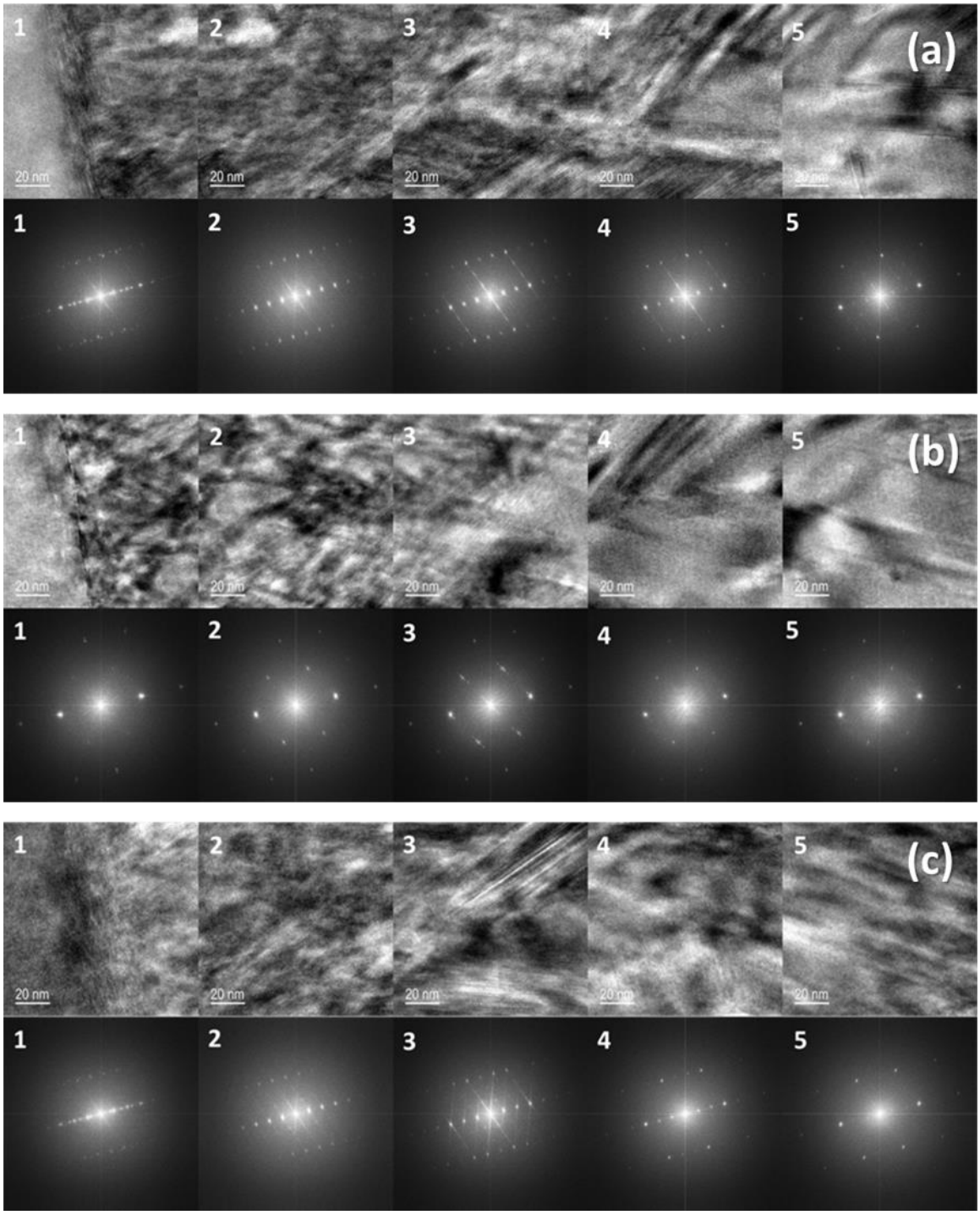

Figure 4-22. HRTEM images of the BP film on SiC viewed in three different zone axes with diffractograms. (a) [11-20], (b) [10-10], (c) [2-1-10].

The microstructure evolution in different orientations which are rotated 30° and 60° about the 4H-SiC [0001] direction were also investigated, the results can be found in Figure 4-22 (b) and (c) respectively. After a 30° rotation, SiC [10-10] zone-axis and BP [112] zone-axis were simultaneously obtained. The extra spots observed at 1/2 [113] in the BP [112] diffraction patterns indicate that a kind of super lattice was formed, and the specific structure of it needs more investigation. The small spots around 1/2 [113] are caused by Moiré fringes, which should be closely related to the twins. While after a 60° rotation, the zone-axis becomes to SiC [2-1-10] which is equivalent to SiC [11-20]. The structure evolution looks similar to what was observed in the SiC [11-20] zone-axis. The three sets of HRTEM images offer us 3D overview of the film and 3D structure of the defects. They all show a trend that the film gets less defective the further away it is from the interface.

4.3.1.3. EELS analysis

Though the BP is identified to have zincblende structure, the atomic ratio between boron and phosphorous is unknown. Is it 1:1 or one prevails over the other? Moreover, is there any impurity absorbed by the film? EELS experiment was then performed to find out the answers. Note that the sample used for this analysis is grown at 800 °C, it has basically the same structure as the one grown at 850 °C.

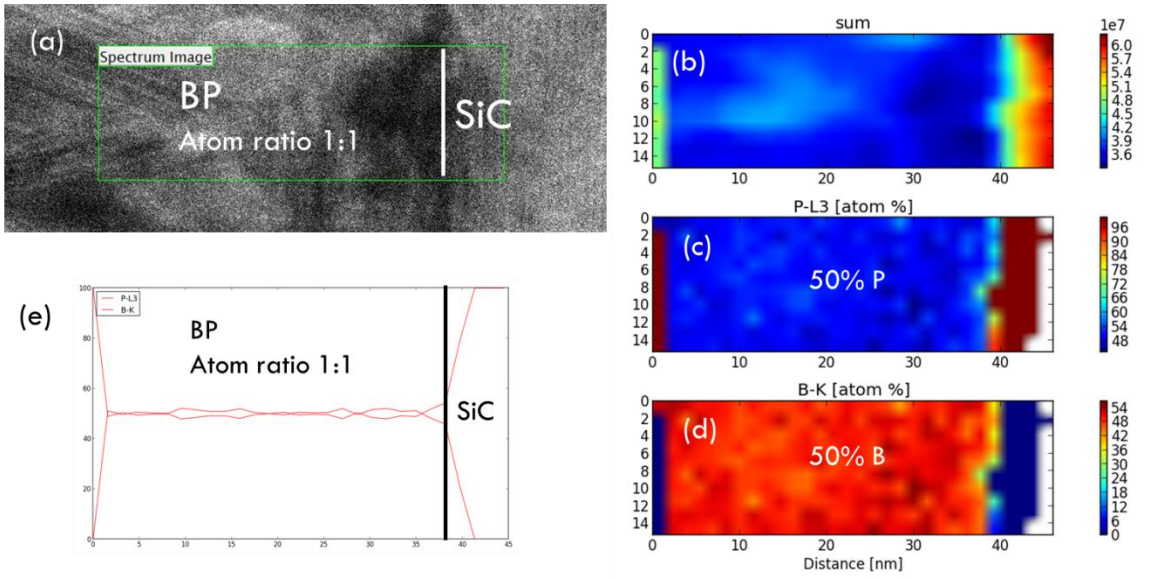

Figure 4-23. EELS analysis of the BP/SiC interface. (a) shows the sampling area of the EELS spectrum, the area is about 50nm×20nm. (b) is the EELS spectrum. (c) is the quantified atomic percent of phosphorus in BP. (d) is the quantified atomic percent of boron in boron phosphide. (e) is the atomic ratio calculated across the sampling area.

A 50nm×20nm area across the interface was selected for EELS investigation, the spectrum image and the EELS spectrum were shown in Figure 4-23 (a) and (b), respectively. Model based quantification was performed via Quantifit 9.02, a python program developed by Dr. Gerd Duscher's research group. The phosphorous $L_{2,3}$ edge at 132eV and the boron K edge at 188eV were fitted with mathematical models and the areal densities were extracted and converted into atomic percentages. The calculated atomic percentages were plotted and shown in Figure 4-23 (c) and (d). They are both 50% with 2% fluctuations. Figure 4-23 (e) was produced by dividing (c) by (d), a 1:1 atomic ratio between boron and phosphorous was obtained.

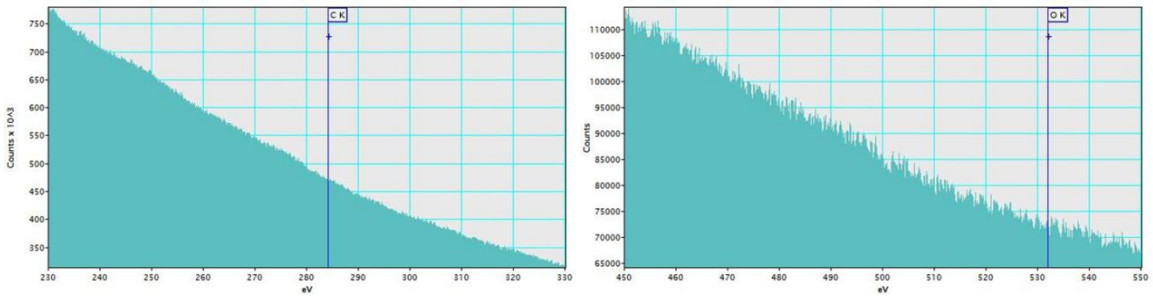

Figure 4-24. EELS investigation of common impurities. (a) No sign of carbon in the film. (b) No sign of oxygen in the film.

By navigating the convergent electron beam over the sample and simultaneously acquiring EELS spectrums, impurity information can be obtained. The EELS spectrums shown in Figure 4-24 are acquired near the interface where BP is more defective and more likely to absorb impurities like carbon or oxygen. However, neither carbon nor oxygen peak was observed in the spectrum. It means that there are no impurities or the density of the impurities is below the detection limit of our EELS detector. In conclusion, the BP film has a high-purity.

4.3.2. Defect identification

General investigations in 4.3.1 offered an overview of the film, but the defects are not identified. This sub-chapter will focus on the identification of all the defects emerged within the film starting from the interface. TEM and STEM are utilized. The formation mechanisms of the defects are also interpreted.

4.3.2.1. Misfit dislocations

Misfit dislocations are inevitable at the interface in all heteroepitaxial systems as long as lattice mismatch exists and the film thickness exceeds the strain-dependent critical value. Aberration-corrected scanning transmission electron microscope (STEM) was used to study the atomic structures at the interface. The image below

(Figure 4-25) was acquired with the dedicated STEM VG HB603 at Oak Ridge National Laboratory. Counting the atoms, we found that 108 BP (111) atomic columns correspond to 112 SiC (11-20) atomic columns. The statistics indicate that there is one misfit dislocation in every 28 SiC lattice planes, or one misfit dislocation per 7.5nm if viewed in the SiC [11-20] zone-axis. Assuming that the SiC lattice is not distorted and using it as a gauge, then the calculated BP (111) d-spacing would be 3.16A which results in a 1.6% misfit at this interface. The theoretical misfit of BP and SiC is, however, 4.5%, which means that BP is still strained by the interface. This finding is consistent with the results of the strain analysis in the later discussion. The role of these misfit dislocations is to release the strain from BP/SiC lattice mismatch. However, there are not enough misfit dislocations present to fully release the strain and the residual strain seems to interact with the subsequently formed twins and planar defects. Normally, for every misfit dislocation there are always two threading dislocations at the ends of the misfit which must thread to a surface or form a loop so that the two ends of the dislocation can join.[59] They typically have detrimental influences on charge carrier mobilities.[60] However, threading dislocations are not observed in the film. Their absence must be due to the abnormal strain relief mechanism of the film.

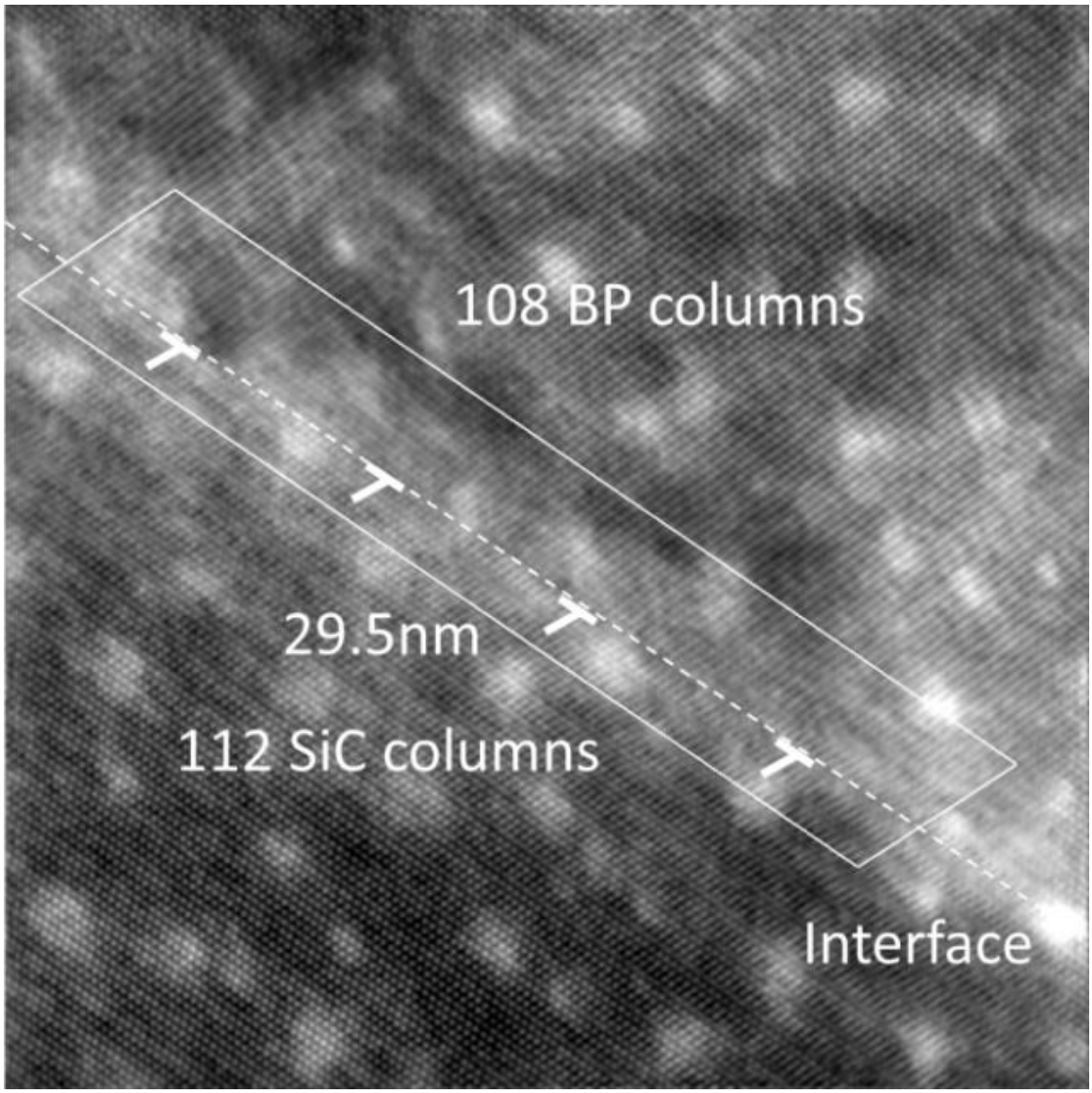

Figure 4-25. Z-contrast image of the interface in SiC [11-20] zone-axis. 108 BP (111) atomic planes correspond to 112 SiC (11-20) atomic planes, which is about 30nm in distance.

4.3.2.2. Twin boundaries

Based on the previous microstructure evolution study, twin boundaries are abundant in the near-interface region of BP. It has been reported that Σ3 coherent twin boundaries (CTBs) emerged at the interface of epitaxial BP on 6H-SiC substrate.[18] However in our growths of epitaxial BP on 4° miscut 4H-SiC, there are not only Σ3 CTBs which normally plays the role of strain-relief, but also Σ3

incoherent twin boundaries (ITBs) which cause extended distortion. They appear as lines and trapezoids, respectively, if viewed in BP [110] zone-axis in the TEM. There are two different atomic stacking sequences (ABC and ACB) in a FCC structured material. Σ3CTBs were formed when ABC and ACB stacking sequences pile up on each other. However Σ3 ITBs are formed when an ABC stack meets an ACB stack horizontally. In this case the "A" atomic layers stay unstrained horizontally in the same positions, known as coincidence site lattice points. But the "B" and "C" layers would be under compressive and tensile strain, or vice versa. Note that these Σ3 ITBs might also appear as Moire' fringes in the TEM if viewed in different view directions. The existence of the two kinds of twin boundaries can be well illustrated using diffractograms because together they form a pattern which looks like a hexagonal closed-packed (HCP) lattice diffraction, as demonstrated in the second diffractogram in Figure 4-22(a). The 1/3 [224], 1/3 [111] and 2/3 [111] diffraction spots which are not supposed to exist in a FCC diffraction with Σ3 CTBs are caused by the coincidence site lattice of the Σ3 ITBs, or to be specific, their formation is due to the change of periodicities in both [224] and [111] directions. Electron micrographs and diffraction patterns of the two kinds of twins are shown in Figure 4-26 and 4-27, respectively. Figure 4-26 are HRTEM images taken in BP [1-10] zone-axis showing twin structures. (a) and (b) show FCC BP with two different stacking sequences: ABC and CBA. (c) shows the formation of Σ3 incoherent twin boundaries (ITBs) as well as Σ3 coherent twin boundaries (CTBs) when ABC stacking meets ACB stacking. (d) shows the atomic positions derived from image (c) showing a similar structure as observed in BP. Changes from Σ3 ITBs to Σ3 CTBs were frequently observed. Figure 4-25 is a HRTEM image taken in the near interface region with its diffractogram on the right. The existence of both Σ3 coherent and incoherent twins is well demonstrated in the diffractogram. Apparently, there are many extra spots beside the typical FCC diffraction pattern which was marked with circles. The square marked spots are caused by Σ3 coherent twins while the triangle marked ones are due to Σ3 incoherent twins.

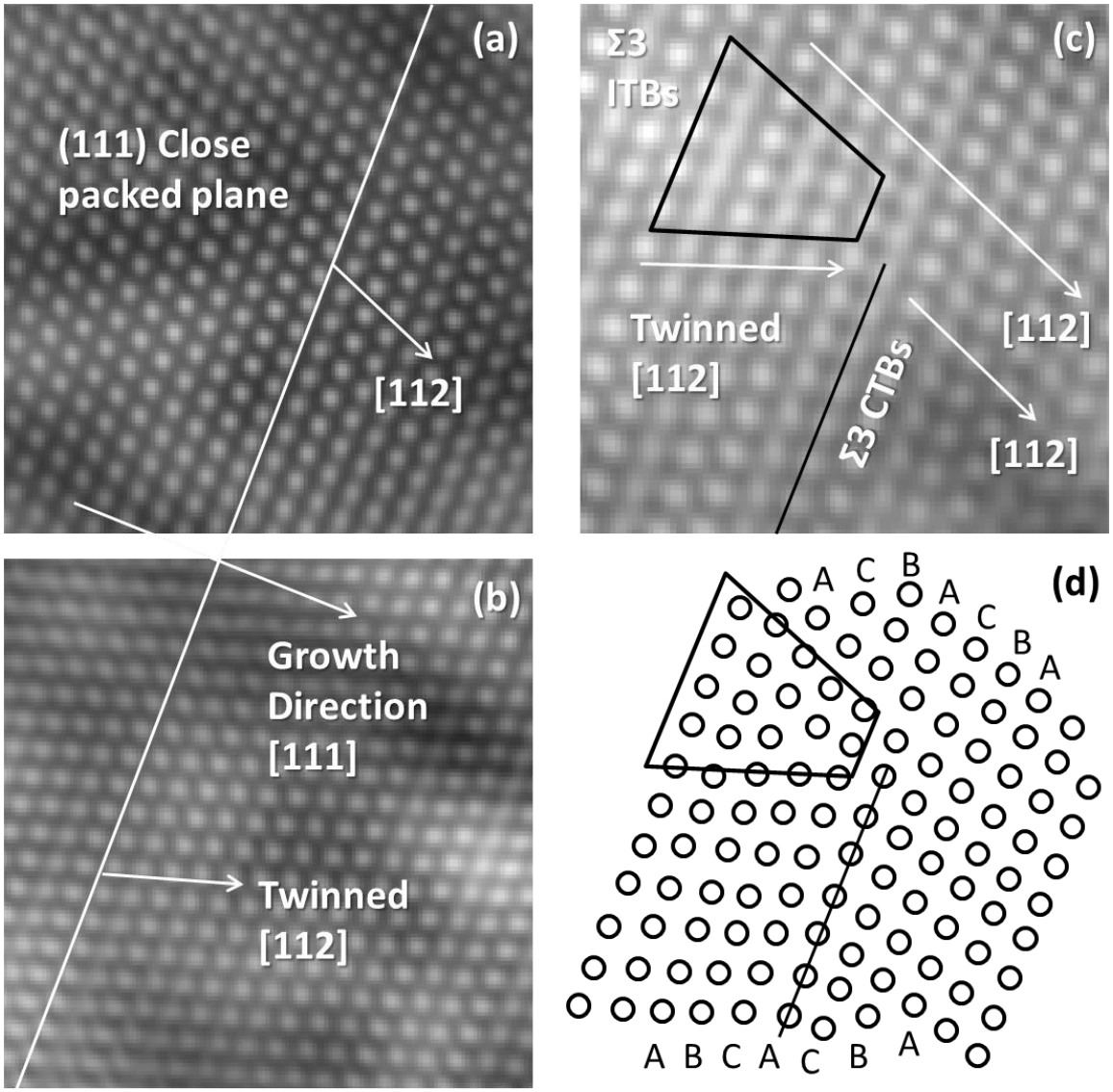

Figure 4-26. HRTEM images of the twin boundaries in BP. (a) and (b): two stacking sequences of the growth. (c) Typical structures of the twin boundaries, the trapezoid and the black line represent Σ3 ITBs and Σ3 CTBs respectively. (d) A model derived from (c).

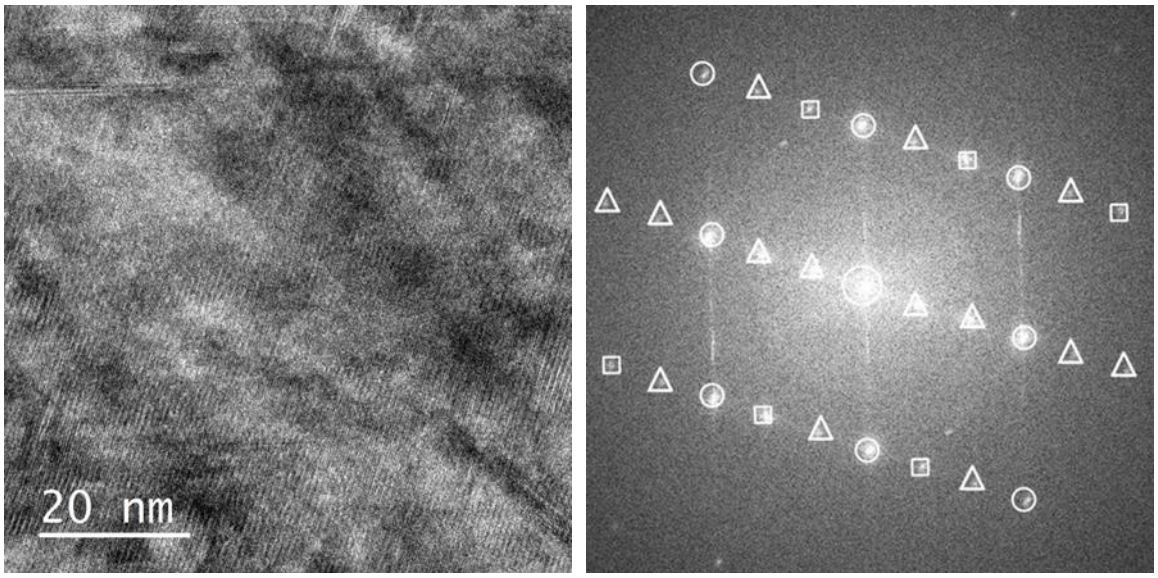

Figure 4-27. A HRTEM image taken in the near interface region with corresponding diffractogram on the right. The circle marked spots form a typical FCC diffraction pattern, the square and triangle marked spots are caused by Σ3 coherent and incoherent twins, respectively. The diffractogram indicates that the two types of twins co-exist in this region.

These twin boundaries can serve as either a source or a sink of the strain and would interact with the residual strain which were not released by the misfit dislocations.

4.3.2.3. Stacking faults and dislocation loops

If, for example, the additional lattice plane is not a half-plane but of finite size, a dislocation loop is formed at the boundary of the dislocation lines. If, the stacking sequence of the crystal structure is interrupted by one or two atomic layers, then a stacking fault is generated. Dislocation loops and stacking faults are widely distributed planar defects in our BP films. The boundary of a stacking fault is actually a dislocation loop. Therefore, they are always accompanied with each other. Their dimensions are limited by the twin boundaries in the near interface region and increase when this limitation is reduced further away from the interface. Figure 4-28 (a) is a HRTEM image illustrating the two types of defects. The stripes circled in Figure 4-28 represent dislocation loops or stacking faults which all lie on the (111)

close packed planes. The contrast of the stripes comes from electron deflection of the defect planes. The pattern inside is the diffractogram of the image, which is a typical FCC BP [110] diffraction pattern. Note that there are also many diffuse streaks connecting the diffraction spots. Their formations are due to the intersections of the Ewald's sphere and the reciprocal rods generated by the planar defects. The streaks in the diffractogram can help determine the orientation of the planar defects and reveal their dimensions and densities between two regions. Figure 4-28 (b) and (c) are Z-contrast images showing clearly a dislocation loop and a stacking fault, respectively.

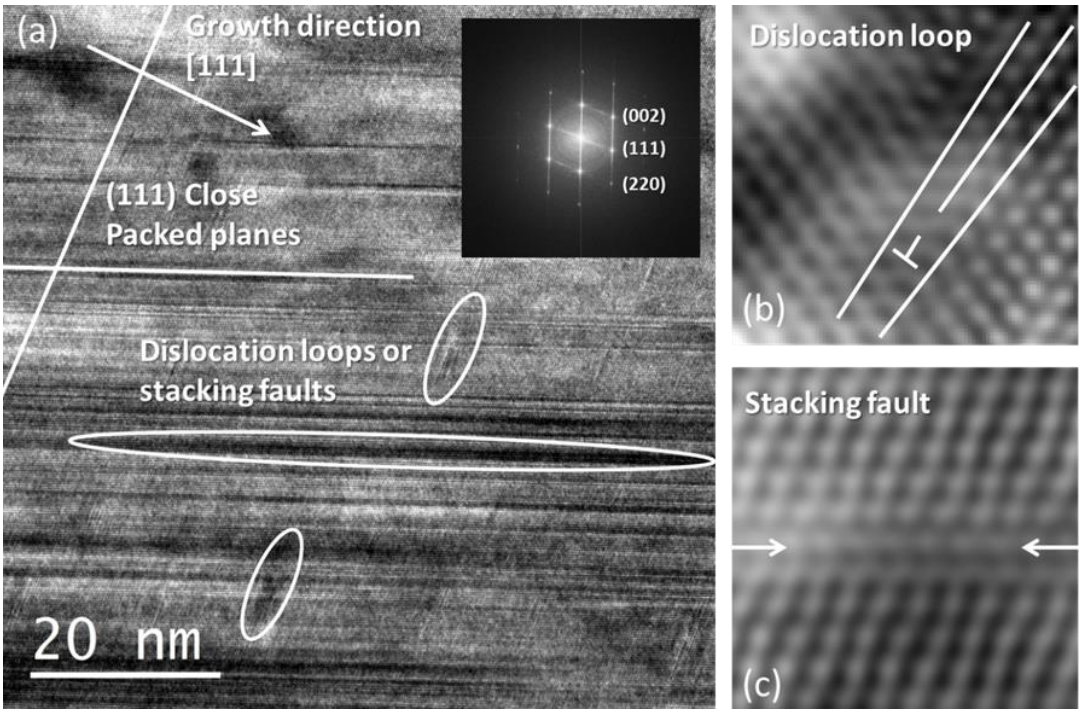

Figure 4-28. HRTEM images with different magnifications showing dislocation loops, stacking faults and the pattern inside Figure 4-28 (a) is its corresponding diffractogram.

4.3.2.4. Dislocations

Dislocations can hardly be found in this film, while twinning, stacking faults and accompanied dislocation loops occur frequently. This is probably because the

formation energy of dislocations is higher than that of twin boundaries or stacking faults. Besides, even if a dislocation forms, it is not supposed to spread far in the film because it will be blocked by the dense twin boundaries or stacking faults.

4.3.2.5. Grain boundaries

Grain boundary is another important defect in the film. The grain boundaries within the film can be divided into two types according to their origination mechanisms. The first type is due to coalescence of the nuclei or further grown crystals. The second type is due to multifold-twinning inside the nuclei which is normally named as Σ3n grain boundaries, "n" is the folds of twinning occurred. They are responsible for the (220) signals in the XRD patterns. Because the first type grain boundaries have multiple orientations. The [220] orientated crystals will generate (220) signals in XRD pattern. The reason the other orientations like [200] or [311] are always absent is because [220] is the most preferred growth orientation and it can easily triumph over the others. This is proved in 4.4. The second type grain boundaries also contribute the (220) signals because two-fold and three-fold twinning will make [220] orientation close to the normal direction of the surface. Then small-angle grain boundaries and a 4° offcut angle will make the (220) planes parallel to the surface and get detected. Figure 4-29 (a) and (b) shows the two mechanisms respectively. (a) is a color mix of the dark field images taken with different diffraction beams. The red area means epitaxial growth. All the other colored areas represent non-epitaxial columnar growths with different orientations. They occur at the coalescing boundaries of the nuclei or further grown crystals and then compete with epitaxial growth. (b) shows the orientation evolution of multifold-twinning.

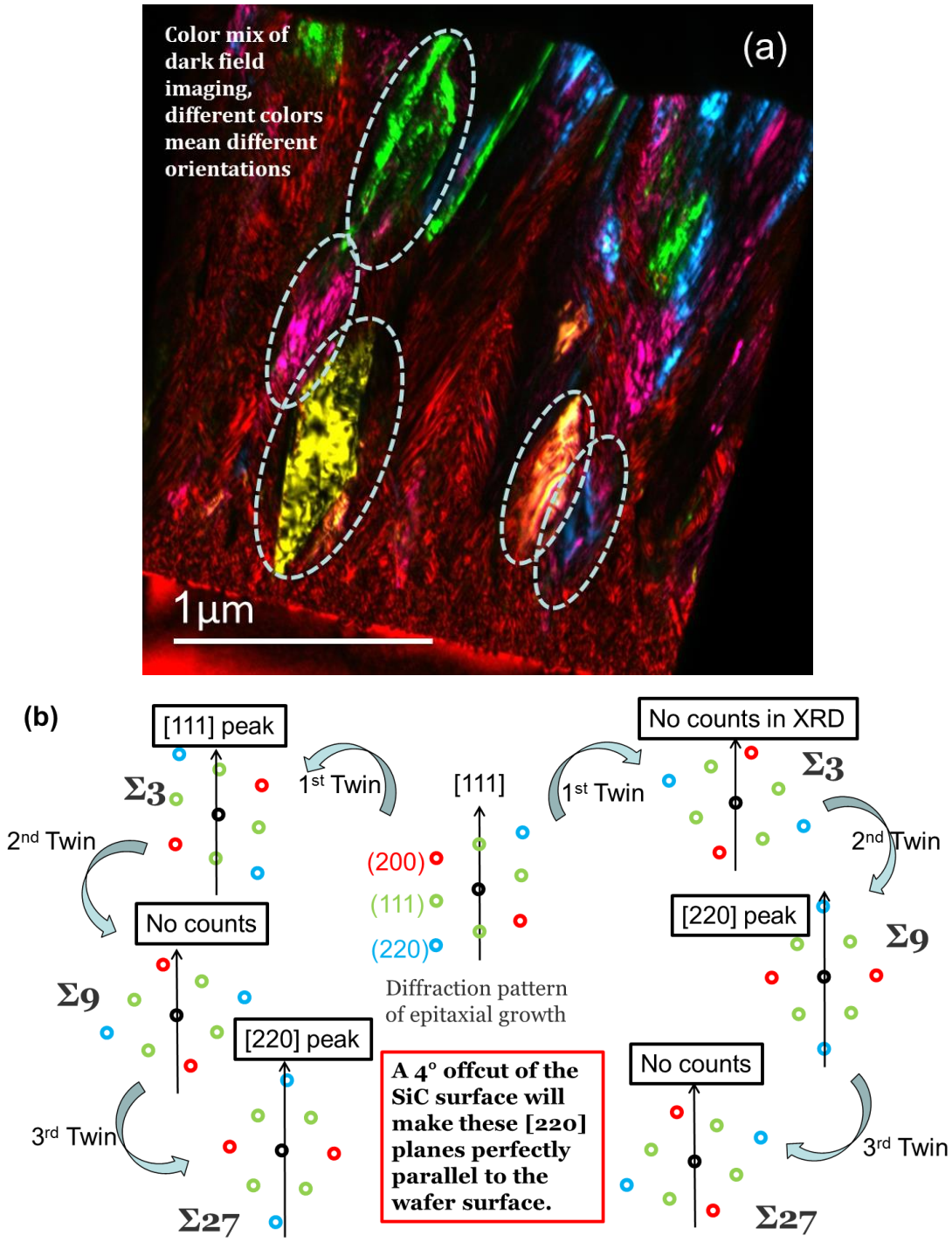

Figure 4-29. Two grain boundary formation mechanisms. The first type (a) is due to coalescence of the nuclei or further grown crystals. The non-epitaxial columnar growth competes with the epitaxial growth. The second type (b) is due to multifold-twinning inside the nuclei which is normally named as Σ3n grain boundaries, "n" is the folds of twinning occurred. They both contribute to the (220) signals in XRD patterns.

4.3.3. Strain analysis

Lattice distortions of the near interface region (<1μm) of the BP film were investigated using diffractograms of the HRTEM images. 13 HRTEM images were taken starting from the interface with step size of approximately 80nm. The d-spacings were calculated and compiled in a plot to show the distortion evolution.

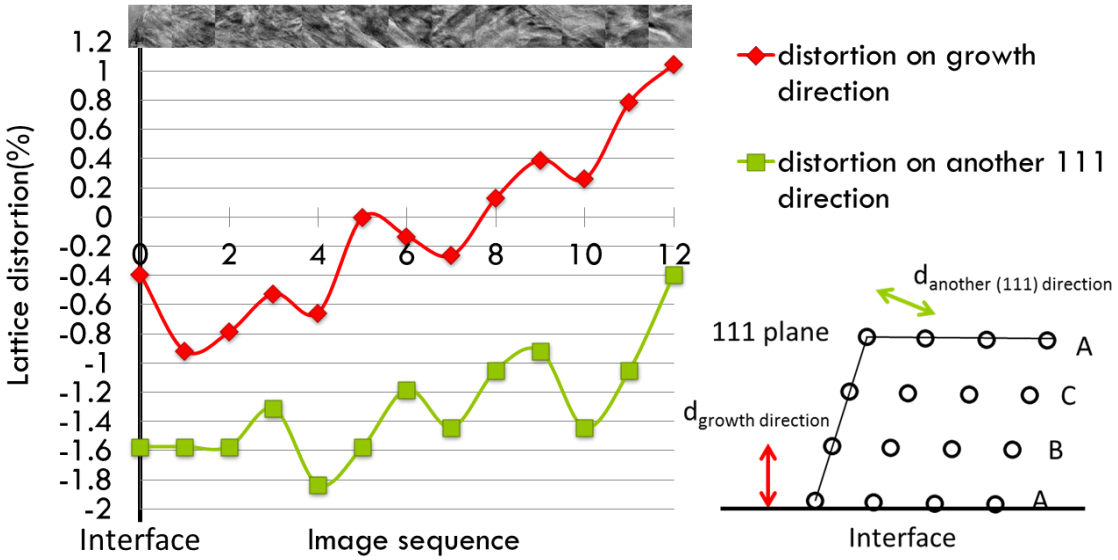

Figure 4-30. Lattice distortion evolution near the interface. The red curve shows distortion along growth direction; the green curve represents distortion in the other close packed plane.

Figure 4-30 shows that basically BP lattices shrink near the interface and expand as the film grows. The d-spacing shrinkage in the growth direction should be closely related to twin boundaries, as we can see the lattice distortion changes from negative to positive values when the density of twin boundaries decreases along the growth direction. This is a general observation in all our epitaxial BP samples. However, the d-spacing reduction in another (111) close packed plane should be due to BP/SiC lattice mismatch. As was mentioned in 4.2.3.1, there are not enough misfit dislocations generated at the interface to fully release the strain of the 4.5% lattice mismatch. Therefore, the residual strain was released by the twinning,

stacking faults and accompanied dislocation loops frequently emerged in the near-interface region. The zigzag shape of the distortion evolution reflects the complex character of the near-interface strain field.

4.3.4. Discussion

Σ3 CTBs and Σ3 ITBs are frequently observed near the interface, the former is normally considered as a result of strain-relief while the latter is not energy-favorable and they form when two FCC structured crystal islands with reversed stacking sequences meet horizontally. Σ3 ITBs can serve as either a source or a sink of the strain. Together they form a complex strain field within the film. Their distribution within the film can lead us to a better understanding of the microstructure evolution. By putting an objective aperture on the characteristic diffraction spots of the twinned crystal and Σ3 ITBs in diffraction mode and then switch to imaging mode, we can obtain the map of the twinned region and Σ3 ITBs. According to the analysis in 4.3.3.2, twinned region can be imaged with the mirrored spots and Σ3 ITBs can be imaged with the 1/3 BP (111), 2/3 BP (111) and 1/3 BP (224) diffraction spots which was actually coincidence lattice sites diffractions. The obtained maps were shown in the Figure 4-31 and Figure 4-32, respectively.

Figure 4-31 illustrutes TEM mapping of the twinned region. (a) is the diffraction pattern of the whole film. The small white circles represent the objective apertures. The selected diffraction spots were indexed. (b) is obtained by imaging with the common (111) diffraction beam in growth direction which contains mostly the diffractions from both the original and twinned crystals. The wide spread bright contrast means most of the BP crystalline grows epitaxially. The black regions perfectly illustrate the above-mentioned growth deviation. They have columar mophologies and compete with the epitaxial growth. Note that the substrate also show bright contrast because the circled area in the diffraction pattern contains also SiC [0001] diffraction. (c) and (d) show the map of the original and twinned BP

crystalline respectively. (e) is a simple combination of (c) and (d), in which the boundaries and overlapped regions indicate twin boundaries. It seems that the two epitaixal orientations are also competing with each other during growth.

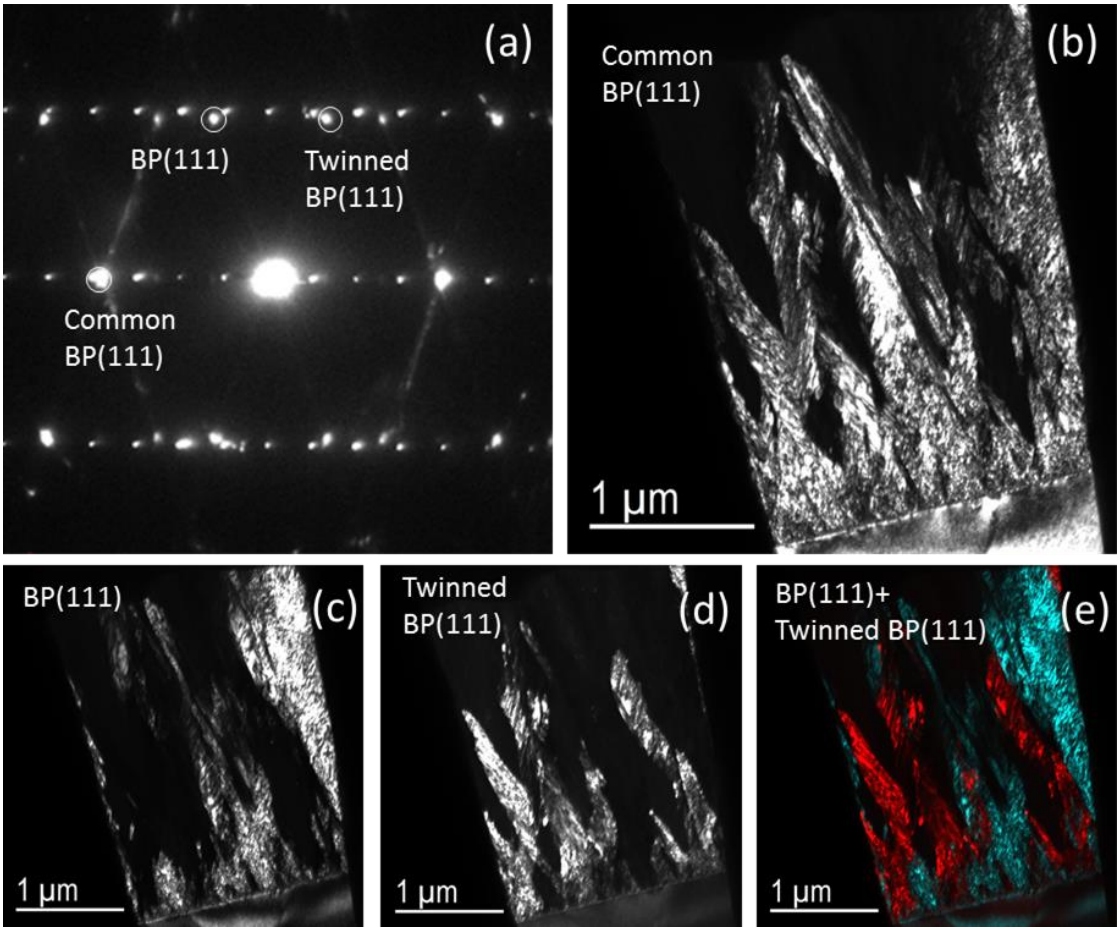

Figure 4-31. TEM mapping of the twinned region. (a) is the Diffraction pattern of the whole film. The small white circles represent the objective apertures. The selected diffraction spots were indexed. (b) is obtained by imaging with the common (111) diffraction beam which comes from both the original and twinned crystal. (c) and (d) show the map of the original and twinned BP crystalline respectively. (e) is a simple combination of (c) and (d), in which the boundaries and overlapped regions indicate twin boundaries and the black regions represent deviated growth.

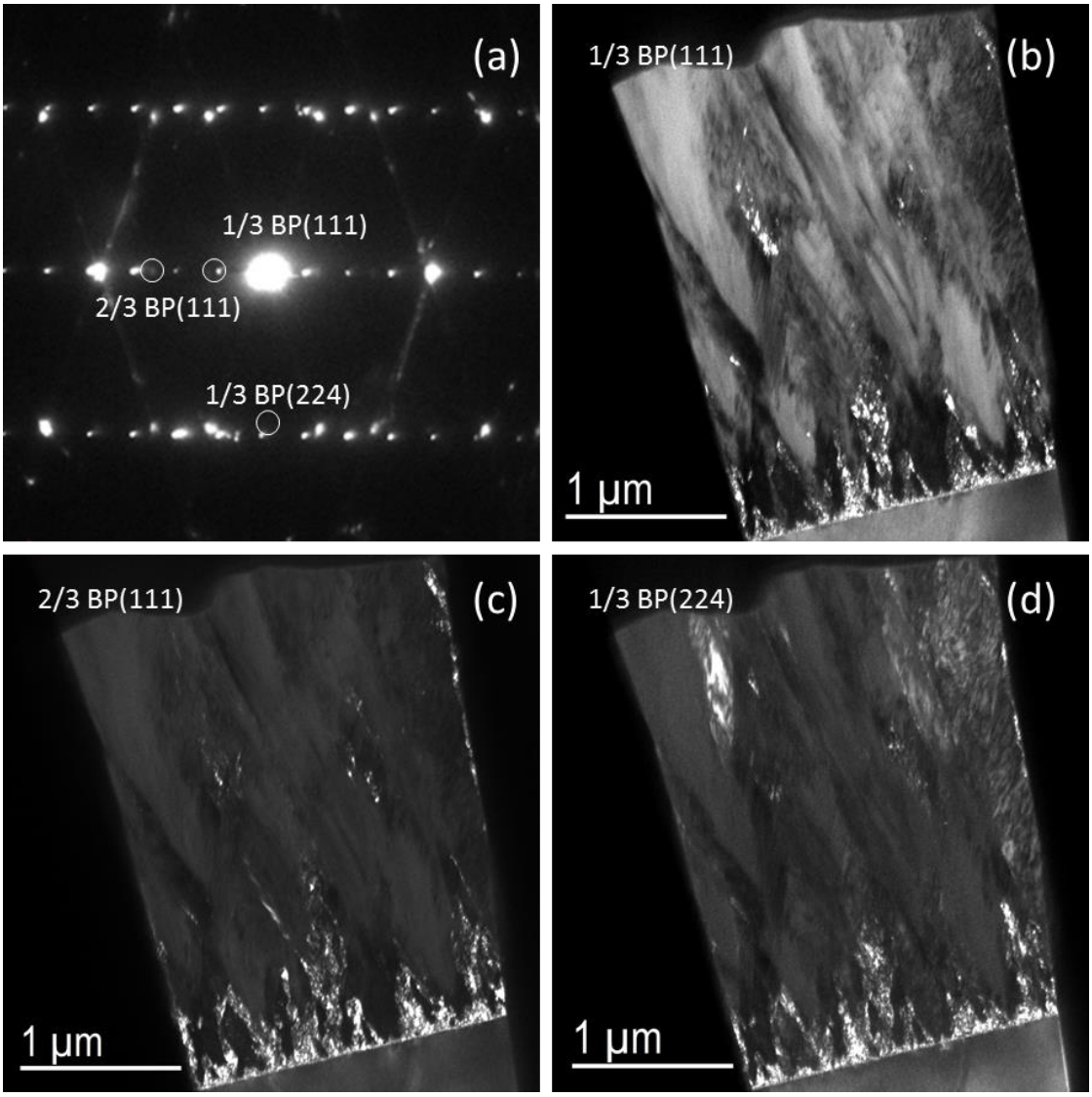

Figure 4-32. TEM mapping of Σ3 ITBs. (a) is the Diffraction pattern of the whole film. The small white circles represent the objective apertures. The selected diffraction spots were indexed. The bright contrast in (b) represents the distribution of BP (111) & SiC(0004) lattice planes. In (c) and (d), the distribution of Σ3 ITBs is mapped.

Similarly, Figure 4-32(a) is the diffraction pattern of the whole film. The small white circles represent the objective apertures. (b), (c) and (d) were obtained by imaging with the 1/3 BP (111), 2/3 BP (111) and 1/3 BP (224) diffraction beam respectively. Apparently the Σ3 ITBs locate mainly at the interface and they can form a complex strain field that run through the whole near-interface region. This agrees with the

above speculation about the absence of threading dislocations. The threading dislocations are believed to have been stopped or suppressed by the densely distributed Σ3 ITBs at the interface.

Again, as was mentioned in 4.3.3.1, misfit dislocations are always accompanied by threading dislocations which are the major defects which limit the performance of heteroepitaxial semiconductor devices. However, no such threading dislocations were found in the relaxed part of our BP film. There are two possibilities for the phenomenon, either no or few threading dislocations were generated, or they were effectively suppressed by the complex strain fields of the twin boundaries. The first possibility seems quite unlikely to us. We propose that the frequent alternation of BP stacking sequences are due to the 4° miscut of the SiC substrate, which creates different SiC steps that were exposed to the source gases. Normally strong covalent bonds favor zincblende sites. [61] They might take wurtzite sites when there is a large strain field around. Irregular atomic arrangement at a vicinal step, lattice mismatch and grain boundary can all contribute to the strain-field. The exposed vicinal surface of 4H-SiC contains both zincblende sites and wurtzite sites, therefore, the probability of BP stacking variation increases accordingly. The structure of the Σ3 ITB in our epitaxial BP on 4H-SiC can be referred to the double positioning boundary in epitaxial β-SiC on α-SiC.[20] Twin boundaries with complex strain field were then formed when the two stacking sequences meet and interact with each other. The evidence supporting this description together with an atomic simulation is shown in Figure 4-33.

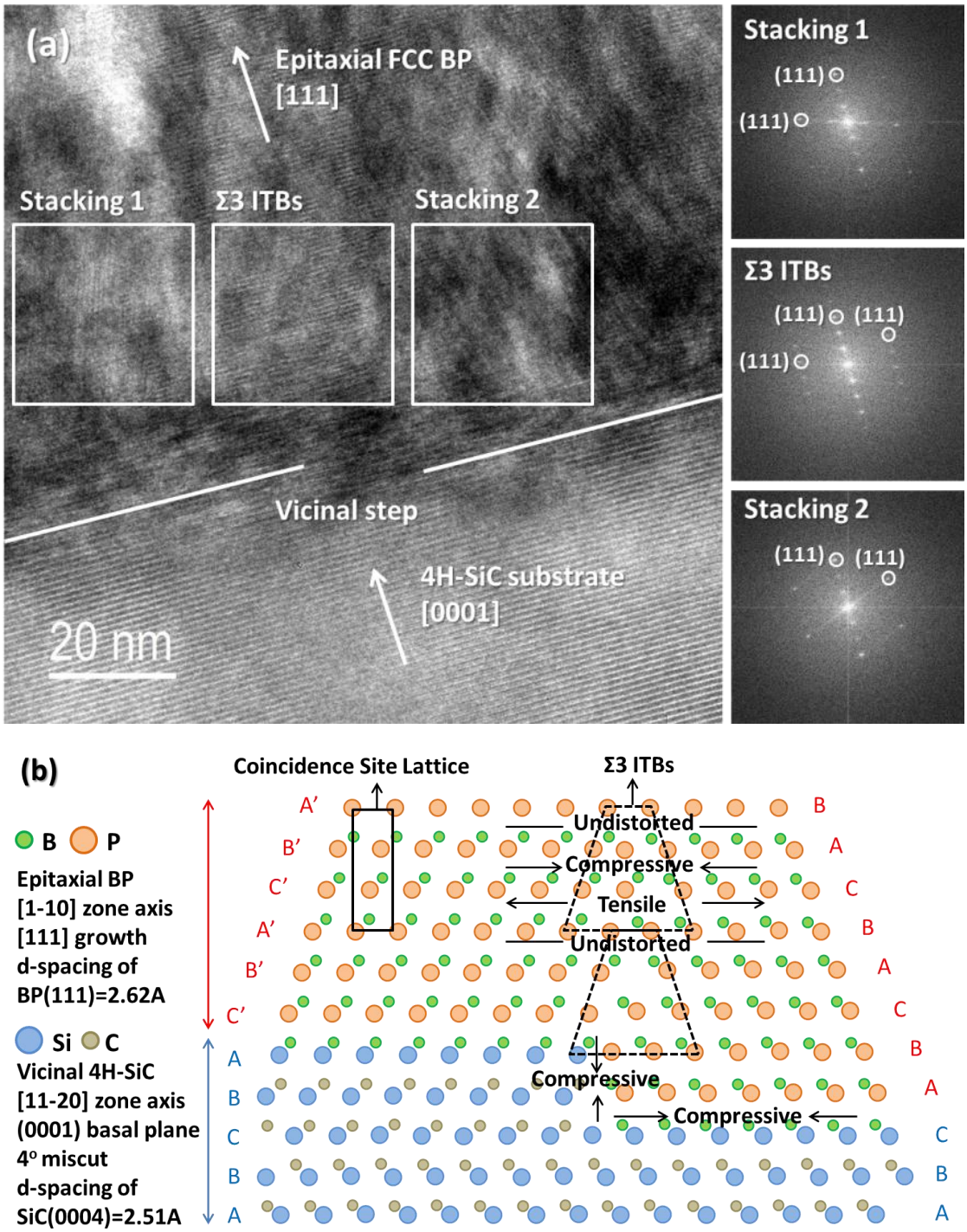

Figure 4-33. (a) HRTEM images showing the formation of Σ3 ITBs on the vicinal SiC substrate. The diffractogram of the Σ3 ITB is the combination of the diffractograms of BP grown on the neighboring terraces. (b) Atomic simulation of the microstructure at the vicinal step. Σ3 ITBs, coincidence site lattices and incoherent twin boundaries, strain types are labeled within the atomic layers. (Misfit dislocations are not shown)

4.3.5. Summary

Generally speaking, the characterized BP film is heteroepitaxial and can be considered as high-purity but fair crystalline quality BP with a variation of defect densities and types. It is not the best sample we grow, but the defect study helped us better understand our material and served as a reference for the future work.

The defect evolution can be roughly summarized as follows: misfit dislocations at interface → high-density twin boundaries and (111) planar defects near the interface → less twin boundaries and (111) planar defects in the middle → grain boundaries near the surface. This BP sample grows epitaxially from SiC, but it deviates from epitaxial growth to some extent as the film gets thicker. The deviation is caused by the crystal coalescence and twinning occurred within the film. The high-density of twins and stacking faults near the interface is due to the high density of the nucleation sites formed at 850°C, they result in a complex strain-field which accounts for the absence or threading dislocations. It has been reported that electron mobility in 3C-SiC which also has the same atomic structure as BP, is higher when the twin concentration is higher. [57] Therefore, twins might still be favorable since they diminish dislocations which are always considered to be detrimental. However, the grain boundaries should be minimized in any circumstances.

4.4. Study of the initial stage of the growth

Since most of the studied samples were synthesized in only half an hour with low growth rates, some of the films were still discontinuous when the deposition process was stopped. Therefore, the initial stage of the growth can be studied by sampling from the growing nuclei in the discontinuous regions of the film. The film growth mechanism and defect origination mechanism were understood via this study. In addition, further growth of the film was successfully predicted to some extent based on the initial stage.

Sample 83, which shows the best crystal quality, was chosen for this study. As was mentioned in 4.2.3.2, sample 83 is grown at 950°C and has fewer nucleation sites but larger-sized nuclei. It means the amount of grain boundaries is reduced compared to the characterized sample in sub-chapter 4.3 which is grown at 850°C. Therefore, a better crystal quality is expected for the 950°C growth. An early stage study of this sample will obviously facilitate the future optimization of BP growth at 950°C. In this sub-chapter, the thermodynamic and kinetic Wulff constructions of the nuclei are both performed; the fastest growth direction is determined; then some specific cases including two most common nuclei and accidentally grown nanorods are thoroughly investigated by electron microscopies. The growth mechanism is well understood through the integrated theoretical and experimental study.

4.4.1. Thermodynamic Wulff construction of the nuclei

We'll start with constructing the thermal equilibrium shape of zincblende BP. According to the Wulff construction method, the crystal shape of equilibrium is the smallest inner polyhedron formed by planes orthogonal to lines drawn from the origin and intersecting these lines at distances proportional to the surface free energy of the respective faces. BP has a FCC structure and is usually bound by three low-index planes, namely (001), (011) and (111) surfaces. These orientations have the lowest surface free energy and their corresponding surface free energy planes can enclose the smallest polyhedron which is considered as the equilibrium shape. Normally the Wulff shape has a faceted morphology composed only of planes, edges and corners.

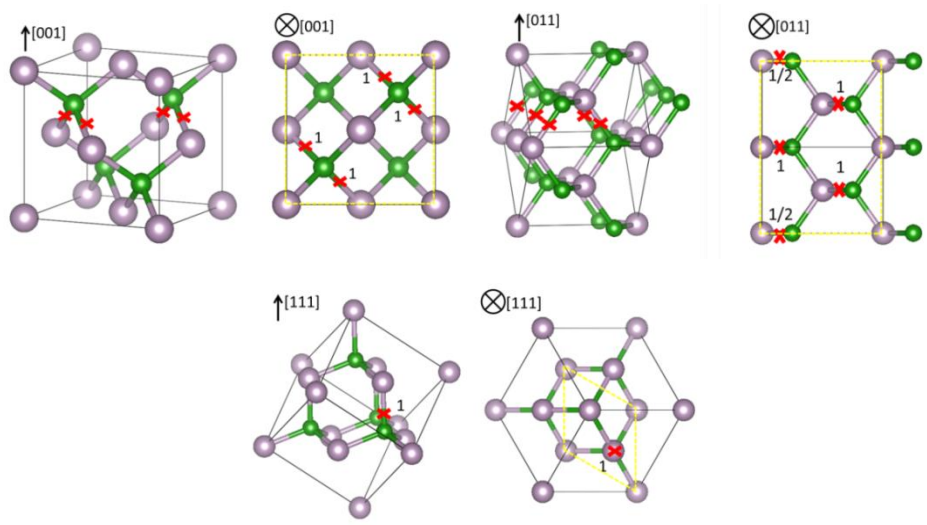

Figure 4-34. Illustration of the surface free energy calculation via the broken-bond model.

To construct Wulff shape, the surface free energies of the facets need to be calculated first. The surface free energy calculation via broken bond model is illustrated in Figure 4-34. The yellow quadrangles represent the calculation units. The number of broken bonds (labeled with red crosses) within the [001], [011], [111] units are 4, 4, 1 respectively. The area of the units in the three orientations are $A_{(001)}= a^2$; $A_{(011)}= \sqrt{2}a^2$; $A_{(111)}= \sqrt{3}/4a^2$ ("a" is the lattice parameter of zincblende BP), respectively. If we use the number of broken bonds to represent energy, the surface free energy vectors of the three facets can be given as follows:

$\boldsymbol{\gamma_{(001)}}= 4/a^2 \times \mathbf{[001]}$;
$\boldsymbol{\gamma_{(011)}}= 4/\sqrt{2}a^2 \times 1/\sqrt{2}\mathbf{[011]}$;
$\boldsymbol{\gamma_{(111)}}= 4/\sqrt{3}a^2 \times 1/\sqrt{3}\mathbf{[111]}$

Note that $\boldsymbol{\gamma_{(001)}}$, $\boldsymbol{\gamma_{(011)}}$, $\boldsymbol{\gamma_{(111)}}$ have 6, 12, 8 equivalent orientations respectively. Each of these vectors has a corresponding surface free energy plane which includes the ending point of the vector and is orthogonal to it. Set a common origin for these vectors, and the equilibrium shape of BP can be constructed by all the corresponding planes. The construction process is shown in Figure 4-35. First, we

plot the polyhedron enclosed by the six (001) surface free energy planes which has the largest surface free energy. A cube with the side length of $8/a^2$ will be obtained. Then we draw the twelve (011) planes. The cube is then truncated into a rhombic dodecahedron with side length of $2\sqrt{3}/a^2$. At last, we further truncate octahedron with the eight (111) planes. The resulted polyhedron is an octahedron with side length of $4\sqrt{2}/a^2$. Therefore, the equilibrium shape of BP should be a perfect octahedron.

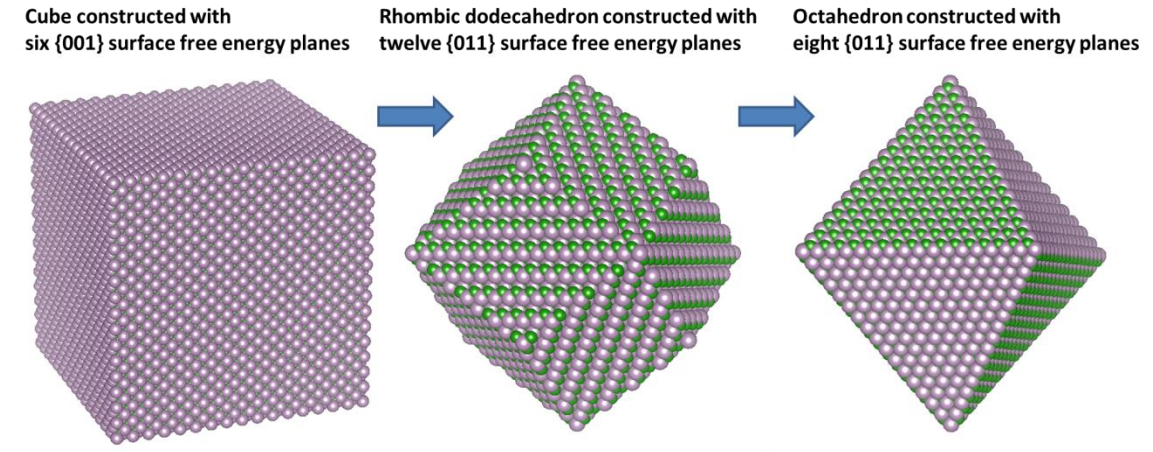

Figure 4-35. Thermodynamic Wulff construction of the equilibrium shape of BP. The cube is constructed by six (001) surface free energy planes. The rhombic dodecahedron is constructed by twelve (011) surface free energy planes. The octahedron is constructed by eight (111) surface free energy planes, it has the smallest volume and serves as the equilibrium shape of BP.

However, perfect octahedrons were never observed during growth. The SEM image and atomic models of the nuclei are shown in Figure 4-36. “A” and ”B” were representatives of the most frequently observed nuclei. They are simulated with atomic models with all the facets indexed. Generally speaking, the shape of a nucleus tends to start with truncated octahedral plate like “A”, and evolves into cub-octahedron like “B” as it grows higher. “C” is actually caused by twinning of a

truncated octahedron, therefore, it is named as twinned truncated octahedron. It is another relatively common nucleus which will be discussed in the 4.4.4.2.

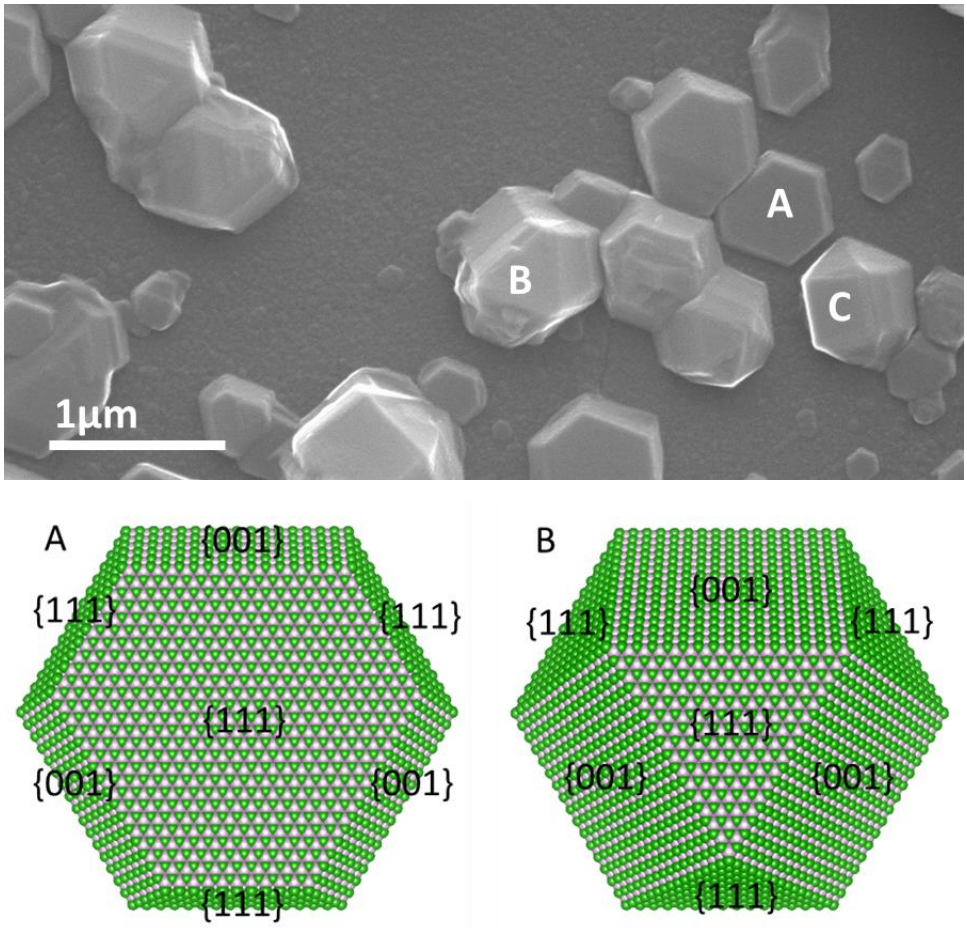

Figure 4-36. SEM image and the atomic models of the nuclei. A" and "B" are representatives of the most frequently observed nuclei. They are simulated with atomic models with all the facets indexed. Most of the nuclei start with shape "A", and evolves into shape "B" as they grow higher. "C" is actually caused by twinning of a truncated octahedron, therefore, it is named as twinned truncated octahedron. It is another relatively common nucleus which will be discussed in the 4.4.4.2.

The mismatch between the construction and the experimental observation means that the growth process is non-equilibrium or the evolution of the nuclei is not thermodynamic results. It seems that thermodynamic Wulff construction method is

not able to predict the crystal shape during growth. However, this is where kinetic Wulff construction comes in.

4.4.2. Kinetic Wulff construction of the nuclei

C. wild [48, 49] did a research on diamond growth and developed kinetic Wulff construction which deals with non-equilibrium growth of nuclei and they successfully simulated diamond growth from faceted nuclei. In their approach, facet growth rates instead of the surface free energies were employed to perform Wulff construction. They induced $\alpha=\sqrt{3}(V_{001}/V_{111})$ as a gauge for the determination of crystal shapes. A series of invariant shapes of the crystallites can be formed by changing α. Figure 4-37 shows the variation of the shape of the kinetic Wulff shapes for diamond with different α values. [50]

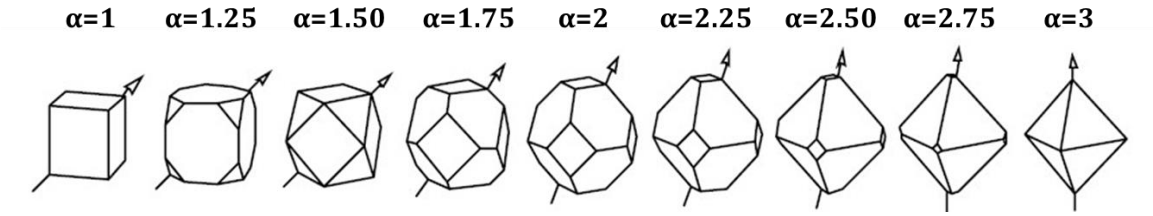

Figure 4-37. The kinetic Wulff shapes for diamond as a function of the facet growth velocity ratio, α. The arrows indicate the fastest growing directions. [50]

Since BP has the similar atomic structure as diamond, the above kinetic method can serve as a good reference for the study of BP nucleation and prediction of further growth. According to Figure 4-37, α for BP should be 1.50 since basically all the nuclei tend to evolve into cub-octahedrons.

P. Smereka, based on Paritosh's work on simulating the dominating growth direction, [51] developed the following expression to show the fastest growing direction:

$$[hkl]_{fastest} = \begin{cases} [111], \alpha \leq 1, \\ [h11], 1 \leq \alpha \leq 1.5 \\ [0k1], 1.5 \leq \alpha \leq 3, \\ [001], \alpha \geq 3, \end{cases} \quad [1]$$

Where

$h=(3-2\alpha)/\alpha$, $k=(3-\alpha)/\alpha$ and $l=1$

Substitute $\alpha=1.5$ for BP into equation [1] and the fasted growth direction is then calculated to be [011]. However, this is still a theoretical result and it has to match with the experimental observations before we can use it for studying the growth mechanism and predicting further growth. The following 4.4.3 will be focused on the experimental verification of the calculation.

4.4.3. The fastest growth direction

The reliability of the above calculation can be verified by reviewing the early experiments in which polycrystalline BP films randomly nucleated on thin amorphous layers that formed first on top of the [001] silicon substrates. The morphology development of a polycrystalline film is determined by the growth competition between the grains. The surviving grains, or in other words, the fastest-growing grains which grow perpendicular to the substrate will dominate the morphology of the film because they will outgrow all the other grains; therefore, the orientations and morphology of a polycrystalline film indicate growth preferences.

In most of the XRD patterns of the early samples, only (111) and (220) peaks were observed. The absence of [001] orientations means the films are not in epitaxial relationship with the [001] silicon substrates. The crystal orientation of the substrate is not inherited by the film because an amorphous layer was formed first due to the large mismatch and some other factors. Instead of epitaxial growth, polycrystalline BP nucleated on top of the amorphous layer and then [111] and [220]

orientations grow competitively. To find out the dominating growth orientations at different growth stage, the XRD count ratios of (111)/(220), as well as (220)/(111), versus film thickness were plotted and shown in Figure 4-38. The data points are collected from a series of BP films grown on [001] silicon substrates.

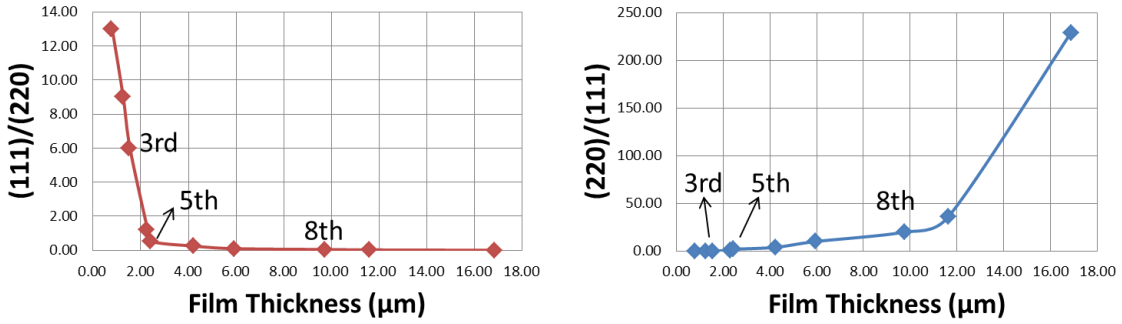

Figure 4-38. Plots of XRD count ratio of (111)/(220) and (220)/(111) versus film thickness. The data points are collected from a series of BP films grown on [001] silicon substrates. Obviously, [220] becomes to the dominating growth orientation as the film grows thicker. SEM images of the cross-section of the 3rd, 5th and 8th samples are shown in Figure 4-39.

The growth competition between [111] and [220] is straightforwardly shown in Figure 4-38. It can be roughly summarized as: [111] growth dominates when the film thickness is less than 1.5μm; [111] and [220] growths are comparable when film thickness in the range of 1.5μm to 2.5μm; [220] growth dominates when the film thickness is larger than 2.5μm. Apparently, [220] is the fastest growing direction since it outgrows [111] eventually as the film thickness increases. The advantage of [111] over [220] growth during the early stage should be due to the larger number of [111] nuclei. However, these [111] nuclei grow much slower than [220] nuclei and will eventually be blocked by the fast growing [220] grains. This explains why pyramid morphology which corresponds to [111] growth dominates in the early stage (<1.5μm) of the growth, while the columnar morphology which implies [220] growth dominates as the film grows to thicker than 2.5μm. SEM images of the cross-section of the 3rd, 5th and 8th samples employed in Figure 4-38 are shown in Figure 4-39.

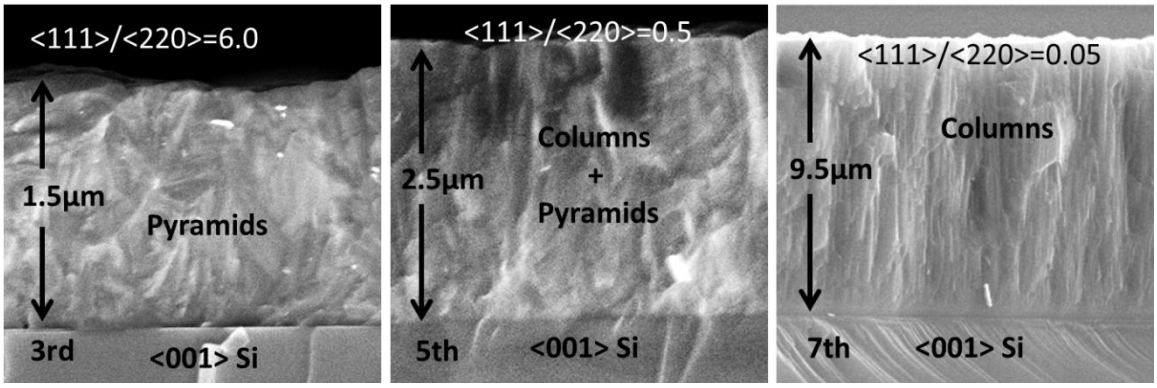

Figure 4-39. SEM images of the cross-sections of the 3rd, 5th and 8th samples involved in of XRD count ratio versus film thickness plot. The evolution of the morphology is: pyramids → Pyramids+columns → columns. This trend matches well with the XRD results.

As labeled in Figure 4-39, the [111]/[220] ratios of the three samples are 6.0, 0.5 and 0.05, respectively. The evolution of the morphology is as follows: pyramids → Pyramids+columns → columns. To further confirm that the columnar structures are indeed oriented in [220] direction, STEM was performed on the 8th sample. The results are shown in Figure 4-40.

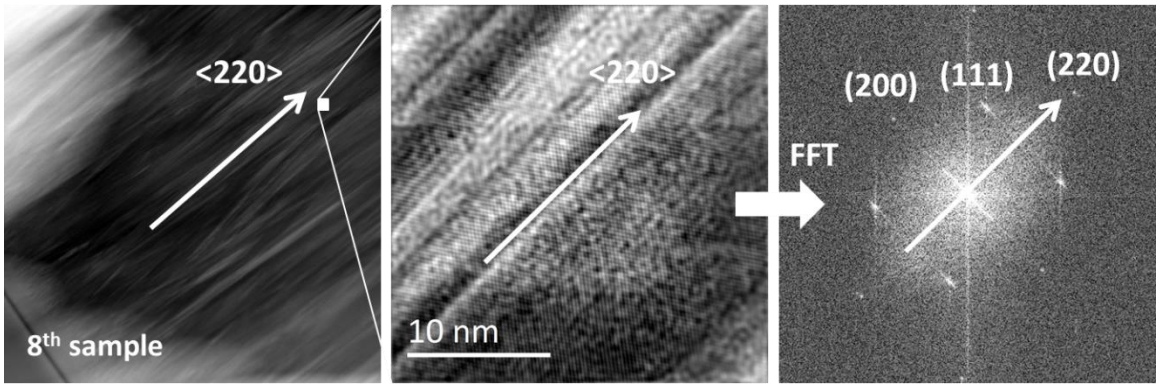

Figure 4-40. The left image is a low magnification STEM image, the columnar structures can be clearly seen. The middle image is taken at 500k, its diffractogram is shown on the right. The columnar orientation is parallel to the (220) diffraction in the diffractogram. It means the columnar crystal grows in [220] direction.

The left image in Figure 4-40 is a low magnification STEM image in which the columnar structures can be clearly seen. The middle image is taken at a magnification of 500k and the right image is the diffractogram of it. Obviously, the columnar orientation is parallel to the (220) diffraction in the diffractogram. This means the columnar crystal grows in [110] direction.

Now, if we refer to Figure 4-36. The nucleus shape evolution can be explained. Figure 4-41 shows simply how the initial nucleus should evolve with different growth rates of the facets. According to SEM examination, no triangular islands are observed, therefore, [110] is the fast growth direction and the equilibrium nucleus shape is cub-octahedron.

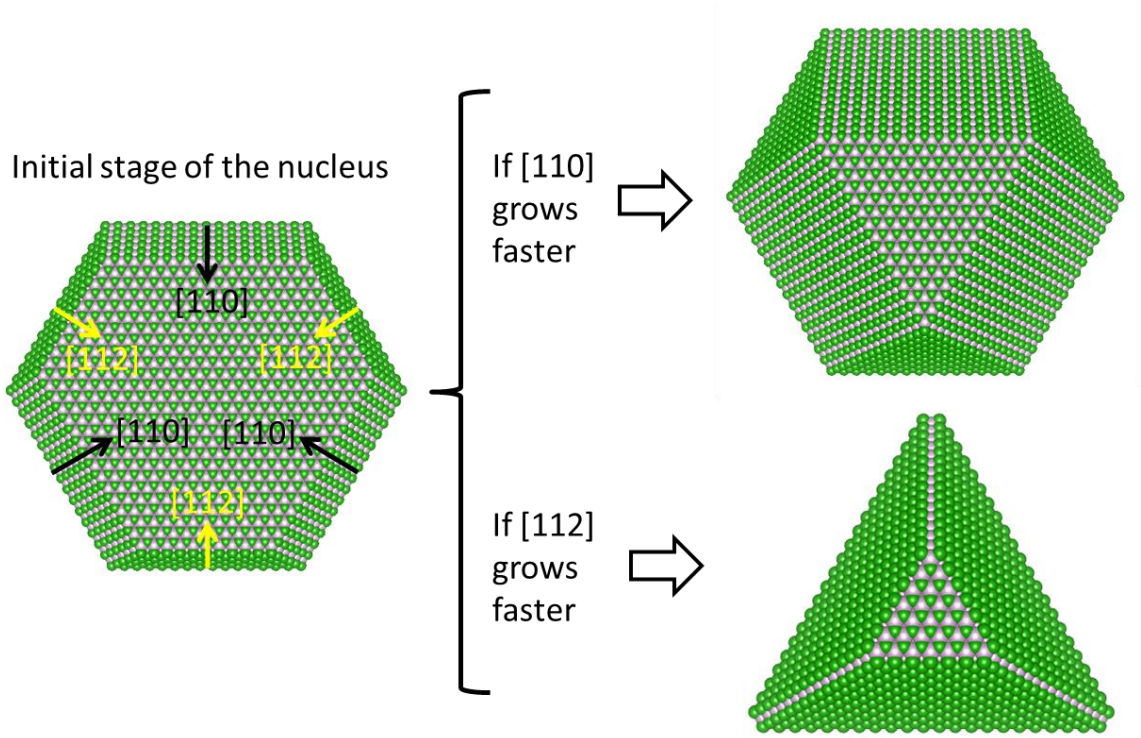

Figure 4-41. Effect of facet growth rate on the shape evolution of a nucleus.

In summary, the orientation and morphology investigations all support the conclusion that [110] is fastest growing orientation. The morphology development

of BP film is perfectly explained. This conclusion is also applied to explain some of the defect originations in the following 4.4.4.

4.4.4. Case study

Defect types and distributions within the film are important to device performance. If one wants to have a better control of the defects, understanding how the defects originate, develop and interact with each other would be the first thing to do, while investigating the typical structures formed during nucleation process is the best way of doing so. We will look into the nuclei before they coalesce and find out what kind of defect originated in the early stage. As was mentioned in 4.4.1, most of the nuclei have truncated octahedral shapes, however there are also non-neglectable number of nuclei are in twinned truncated octahedral shapes which have not be reported before. Besides, some hexagonal nanorods are also formed accidentally in some area. Though the nanorods are unexpected and undesired, investigation of these structures will help understand the growth mechanism. The above-mentioned structures will be the cases covered in this small sub-chapter. All the TEM samples in this chapter are taken from sample 83. FIB, SEM and TEM with high-resolution and tilting capabilities make the selection of interested regions, 3D examinations and atomic-level analysis available.

4.4.4.1. Truncated octahedral nuclei

We will start with the most popular truncated octahedral nuclei. Overview images of the selected nuclei are shown in Figure 4-42. Three truncated octahedrons in a row were targeted for SEM as well as TEM study.

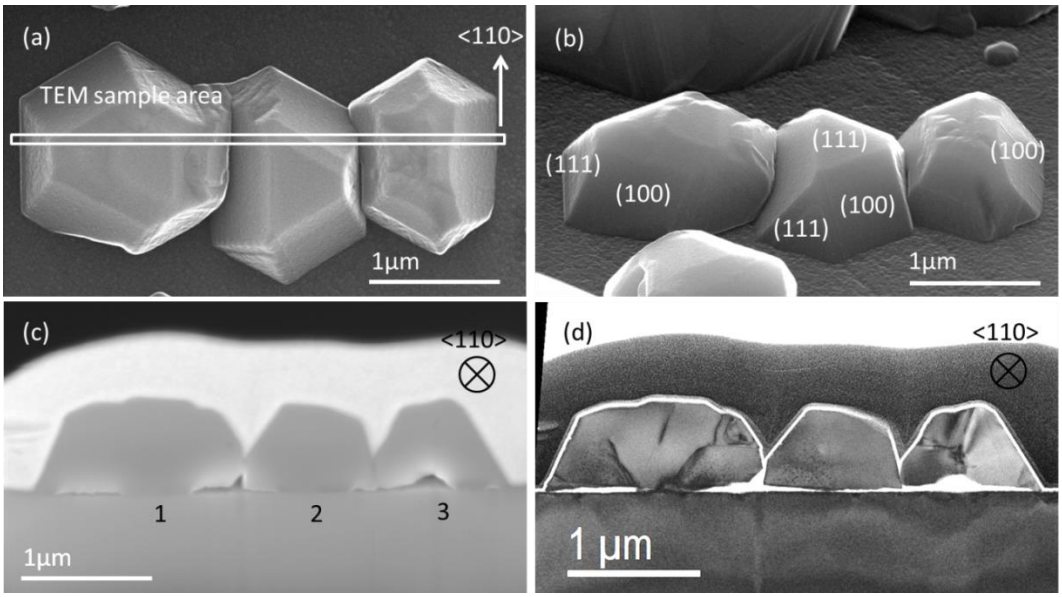

Figure 4-42. SEM and STEM overview of the truncated octahedral nuclei. (a). SEM image of the planview of the nuclei. TEM sampling area is labeled. (b). 54° tilted view of the nuclei. Some of the facet planes are indexed. (c). SEM image of the cross-section sample. This TEM sample is cutted via FIB. (d) STEM image of the cross-section. Features such as grain boundaries and stacking faults can be seen.

Figure 4-42 is the SEM and STEM overview of the truncated octahedral nuclei. (a) is an SEM image of the planview of the nuclei. All the edges of the hexagons are parallel to equivalent [110] directions. The white rectangle represents the TEM sampling area. (b) is an SEM image of the nuclei after a 54° tilt. As is labeled in the image, the large facets are either (001) type or (111) type. (c) is an SEM image of the FIB cut sample. The nuclei are labeled as number 1, 2 and 3. They roughly show trapezoid shapes if viewing in [110] direction. (d) STEM images of the nuclei cross-sections. Features such as grain boundaries and stacking faults can be clearly seen. The void between the substrate and the nuclei are caused by the ion beam damage. What happened at the interface? What kinds of structures initialized from the very beginning? How does the crystal evolve and how do the nuclei coalesce? The answers can be found out by zooming into these nuclei. We will start with the first nucleus. A composite image of nucleus 1 is shown in Figure 4-43. Some typical structures are shown in the atom resolved TEM images.

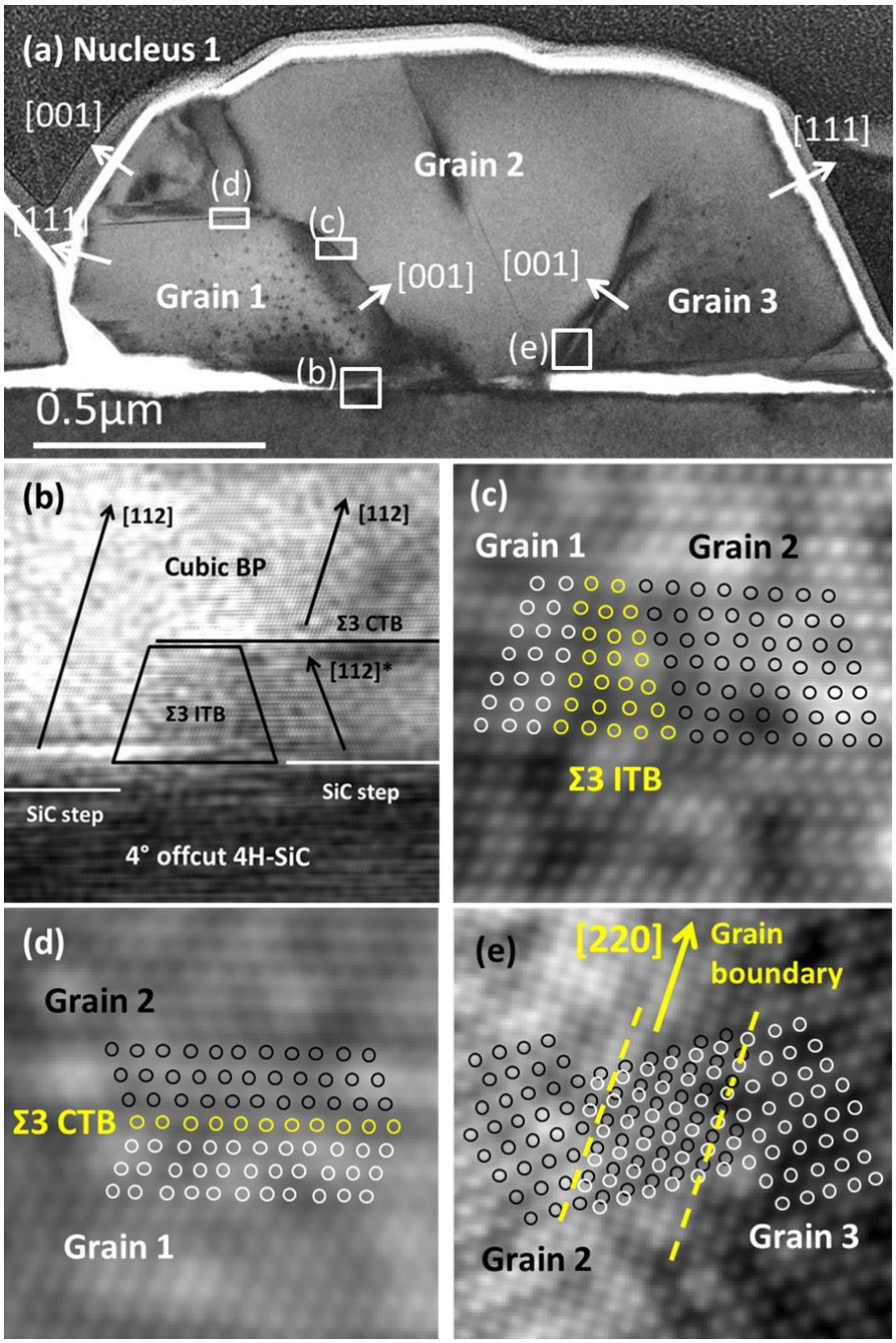

Figure 4-43. Composite image of nucleus 1 which consists of 3 grains and 2 orientatioins. All images are taken in [110] direction. It can be seen that grain 2 outgrew grain 1 and 3. The previously proposed interface structure is observed again in (b). (c) and (d) are the grain boundaries between grain 1 and 2 in different positions, they are Σ3 ITB and Σ3 CTB, respectively. The yellow circles represent the boundary atoms. (e) shows the grain boundary between grain 2 and 3. The orientations of the two grains are the same, but the atomic planes mismatched a little bit. The atom arrangements are modeled with white and black circles.

It can be easily found in Figure 4-43 that the previously named nucleus 1 actually consists of three large grains, which cannot be distinguished under SEM. We will still use the name "Nucleus 1" for convenience and consistency. The orientations of the lateral facets of grain 1 are in the reverse order of that of grain 2 and grain 3. Grain 2 outgrew the other two grains and eventually blocked the growth of grain 1 while consuming grain3. Four areas of this nucleus were selected and magnified to reveal the details. (b) shows the BP/SiC interface, the previously proposed structure in chapter 4.3.4 is observed again. (c) and (d) show the grain boundaries between grain 1 and 2 in the lateral direction and film growth direction, respectively. The yellow circles represent the boundary atoms. Since grain 2 is the one-fold twin of grain 1, the grain boundary between them is either Σ3 ITB or Σ3 CTB. While the boundary between grain 2 and grain 3 is different since they have exactly the same orientations. Their boundary is along [220] direction and it is caused by the mismatch of the atomic planes. The atom arrangements are modeled in (e). The contrast of this boundary is a result of the strain field induced by the atomic plane mismatch. These grain boundaries are the dominating defects in this nucleus. The sharp lines in the middle and the flat curves in the left corner of Figure 4-43 (a) represent stacking faults and dislocations respectively. They result from the strain accumulated at the grain boundaries. More detailed descriptions can be found in the analysis of Nucleus 3 which has almost all kinds of defects. Besides, there are also some abnormal defects which had never been observed before, that are, the densely dispersed black spots near the (001) facet of grain 1 and 3. The same thing also happened in nucleus 2 which is single-crystalline bulk and has no grain boundaries at all, as is shown in Figure 4-44.

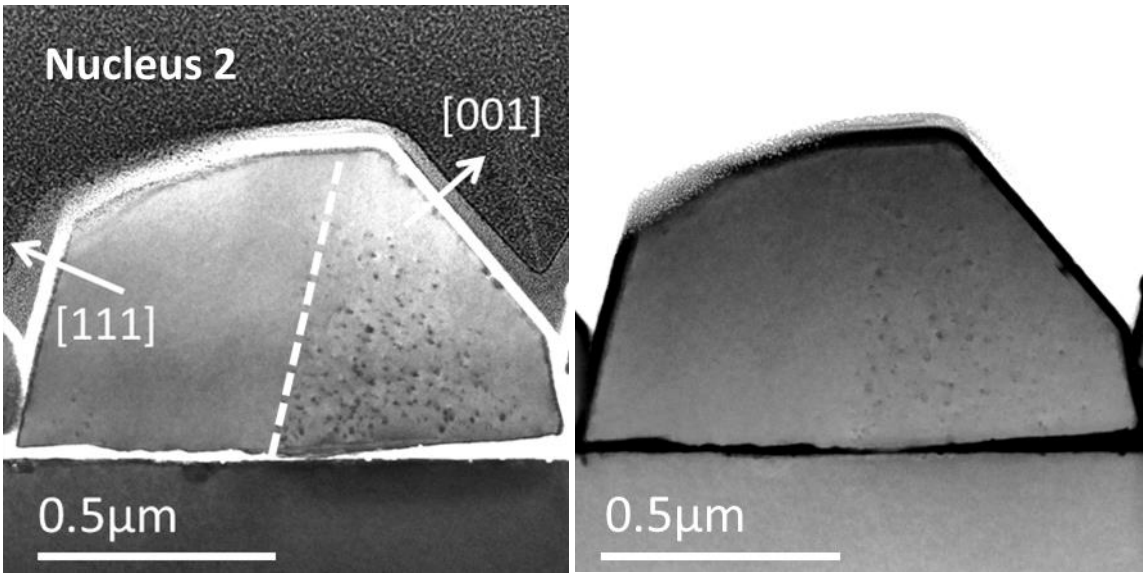

Figure 4-44. STEM bright field image (left) and Z-contrast image (right) of nucleus 2. Note that the black spots dispersed only near the [001] facet. It is hard to identify this type of defect from only one view direction.

Figure 4-44 shows the STEM bright field (left) and Z-contrast (right) images of Nucleus 2. The above-mentioned black spots dispersed only near the [001] facet. The contrast of these spots comes from the strain field induced by the defects. And the defects could be dislocation loops, impurities or precipitates. According to the EELS analysis, no extra elements were observed on these spots compared to the bulk BP crystal. Thus possibility of them being impurities can be excluded. But it is still hard to identify this type of defect from only one view direction. A planview investigation was performed and the integrated analysis is shown in 4.4.4.3.

The structure of nucleus 3 is more complicated than that of both nucleus 1 and 2. It has four grains and three different orientations. The details are shown in Figure 4-45. Figure 4-45 (a) is an overview. (b) is a magnified image of the joint of the four grains. The boundaries are roughly marked out with the dashed lines. (c) is the boundary between Nucleus 3 and 2. The position of it can be referred to the small square in (a). As is shown in the simulated atomic arrays, the two coalesced nuclei have exactly the same orientations. This is the reason why I named it coherent

boundary in the figure. The difference between this boundary and that in Figure 4-43 (e) is that no lattice mismatch is observed. Instead, a very small amount of stacking faults and microtwins are generated to release the strain induced during the coalescence. (d) is a HRTEM image of the joint of grain 1, 2 and 3. Grain 2 is a one-fold twin of grain 1, while grain 3 is a two-fold twin of grain 1. Therefore, the grain boundary between grain 1 and 2 is Σ3 type and that between grain 1 and 3 is Σ9 type. Note that though the common areas of grain 1 and 2, as well as grain 2 and 3 are labeled as Moire' fringes, they are indications of Σ3 ITBs. Because whether they appear as Moire' fringes or Σ3 ITBs depends on the view direction (see Figure 4-46). (e) shows the joint of grain 1, 3 and 4. According to the simulated 4×4 atomic arrays, grain 4 has the same orientation as grain 2 and they are both one-fold twins of grain 1. Thus the boundary between grain 1 and 4 is Σ3 type and the boundary between grain 3 and grain 4 is still in the form of Moire's fringes. (f) shows the end of a dislocation. It starts from the highly strained Σ9 grain boundary region and ends inside the crystal. A strain field is generated along the way it extends. Figure 4-46 illustrated the correlation between Σ3 ITB and Moire fringes in FCC structured materials (covalent bonds are not shown). (a) is the planview of the boundary between two atomic layers in different stacking sequences. The red balls represent stack "A" and it lies at the bottom. The second layer on top of "A" is "B" on the left part and "C" on the right part. They all have hexagonal arrangements along [111] direction. The red dashed rectangle is the boundary region. This boundary appears as Σ3 ITB if viewed in direction parallel to it, while it becomes to Moire fringes if the view direction is rotated by 60°. (b) is the cross-sectional view in [1-10] direction of (a), the first two layers are marked with a black dashed rectangle. And, the red dashed rectangle means the Σ3 ITB region. Apparently, the atom arrangements look distorted at the boundary region. (c) is another cross-sectional view after a 60° rotation of [1-10]. The Σ3 ITB becomes to Moire fringes from this view direction. The two layers between two "A" stacks are equivalent to the electron beam, therefore, they show the same contrast in the TEM images. TEM images of Σ3 ITB and Moire fringes are shown in Figure 4-47 for comparison.

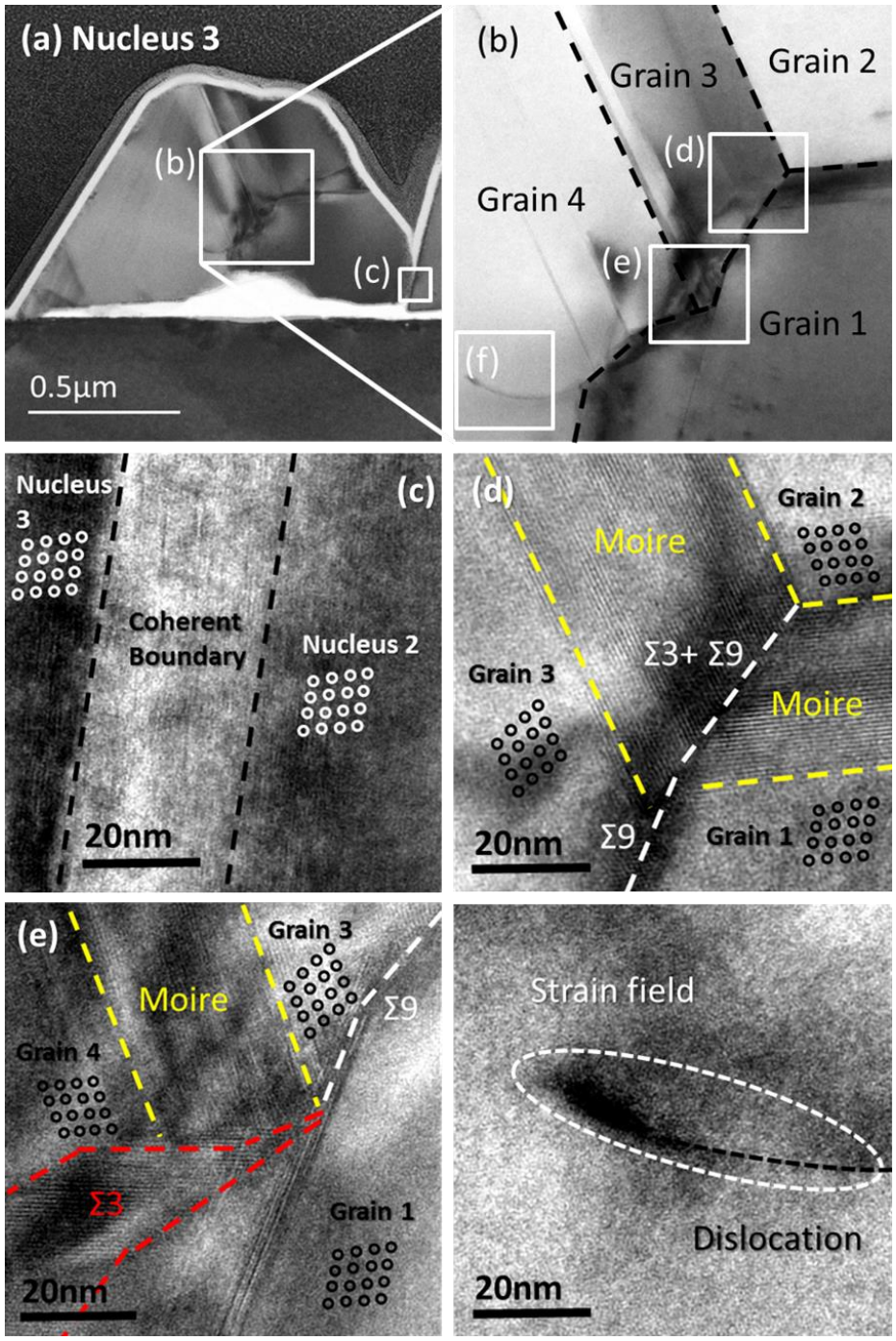

Figure 4-45. Composite image of nucleus 3 which consists of 4 grains and 3 orientations. All images are taken in [110] direction. (a) is an overview. (b) is a magnified image of the joint of the 4 grains. (c) is the boundary where nucleus 3 and nucleus 2 coalesce. (d) is the joint of grain 1, 2 and 3. (e) is the joint of grain 1, 3 and 4. (f) shows the end of a dislocation and the strain field it brought. The types of the boundaries are all labeled in the figures. The 4×4 atomic arrays show the orientations of the corresponding grains.

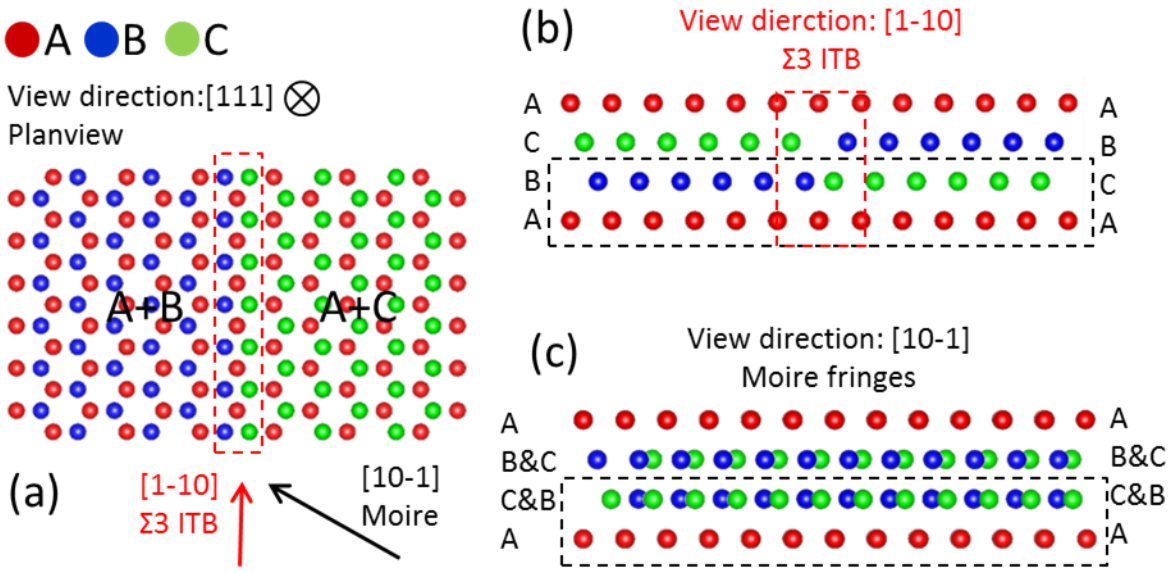

Figure 4-46. Illustration of the correlation between Σ3 ITB and Moire fringes (covalent bonds are not shown here). (a) is the planview of the boundary between two atomic layers in different stacking sequences. The red balls represent stack "A" and it lies at the bottom. The second layer on top of "A" is "B" on the left part and "C" on the right part. The red dashed rectangle is the boundary region. This boundary appears as Σ3 ITB if viewed in direction parallel to it, while it changes to Moire fringes if the view direction is rotated by 60°. (b) is the cross-sectional view in [1-10] direction of (a), the first two layers are marked out with a black dashed rectangle. And still, the red dashed rectangle means the Σ3 ITB region. (c) is another cross-sectional view after a 60° rotation of [1-10]. The Σ3 ITB becomes to Moire fringes from this view direction.

Figure 4-47 shows the TEM images of Σ3 ITB and Moire fringes. (a) is the STEM bright-field (BF) overview image of nucleus 1, and the white rectangle inside is where (b) is taken. Both Moire fringes and Σ3 ITB can be found in (b). Moire fringes give extended uniform contrast in STEM BF image, while Σ3 ITB looks like a sharp boundary in a zigzag shape. (c) and (d) are HRTEM images of the selected region in (b). Atomic simulations are given in (c) and (d) for comparison. Moire fringes are observed much more frequently than Σ3 ITB because any view direction that is not parallel to the boundary will result in an area of Moire fringes under TEM.

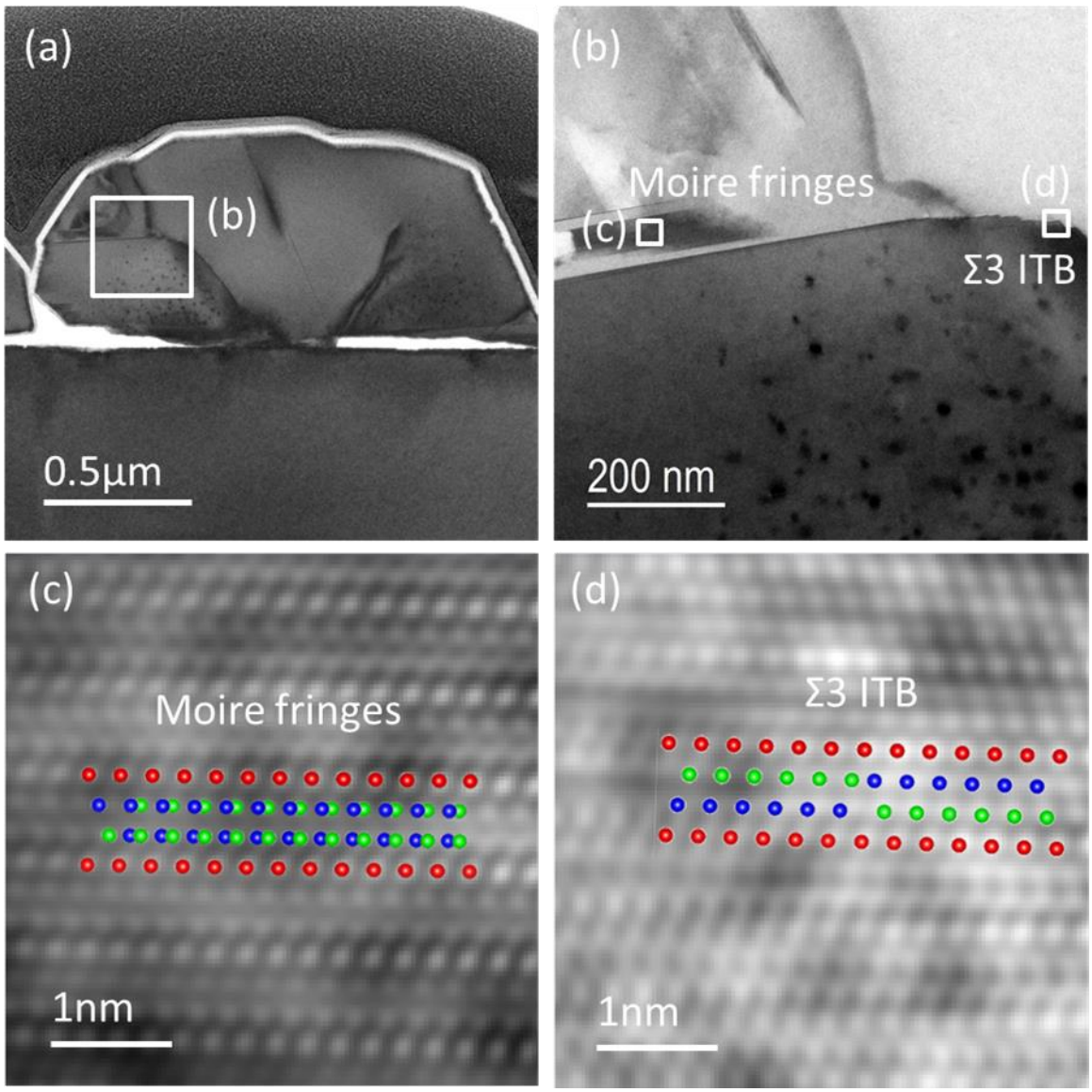

Figure 4-47. TEM images of Σ3 ITB and Moire fringes. (a) is the STEM bright-field (BF) overview image of nucleus 1, the white rectangle is where (b) is taken. Both Moire fringes and Σ3 ITB can be found in this region. Moire fringes give uniform contrast in STEM BF image, while Σ3 ITB appears as a sharp boundary in a zig-zag shape. (c) and (d) are HRTEM images of the selected region in (b). Atomic simulations are given in (c) and (d) for comparison. (what are shown are just lattice points, covalent bonds are not shown.)

To sum up, basically all kinds of defect and microstructures demonstrated in 4.3.1 were found to emerge in the early stage. Twin boundaries, stacking faults and Moire fringes resulted from lattice mismatch, low twinning and stacking fault energies and

the competition between “ABC” and ”ACB” growths. The formation of Σ9, 27 or 81 grain boundaries was due to the coalescence of multiple-fold twinned crystals. Dislocations were generated to release the strain at the interface or grain boundaries. Therefore, interface quality, low twinning and stacking fault energies and alternating “ABC” and ”ACB” growths are responsible for the origination of the defects.

4.4.4.2. Twinned truncated octahedral nuclei

Another common shape of the nuclei is the so-called twinned truncated octahedron. Figure 4-48 shows the SEM and STEM overview. Figure 4-48 (a) and (b) show the planview and 54° tilted SEM images respectively. It doesn’t have a (111) mesa as the typical nucleus discussed in 4.4.4.1, instead, it has an edge on the very top. This edge is parallel to [110] direction because it aligns with the edge of the nearby hexagonal nuclei. (c) and (d) show the STEM images of the cross-sections in [110] and [112] zone axes, respectively. To be specific, (d) is obtained by rotating the orientation of (c) by 30° about the normal direction of the basal plane. As is labeled in (c) as well as (d), the nucleus is partitioned into 4 grains by 3 twin boundaries (TBs). Note that two of the grains becomes white after rotating from [110] zone-axis into [112] zone-axis. This which means the two grains do not reach [112] zone-axis as the other two. Therefore, it can be concluded that the (111) planes of these two grains are not parallel to the rotation plane, or in the words, the SiC basal plane. The Detailed cross-section TEM analysis is shown in Figure 4-49.

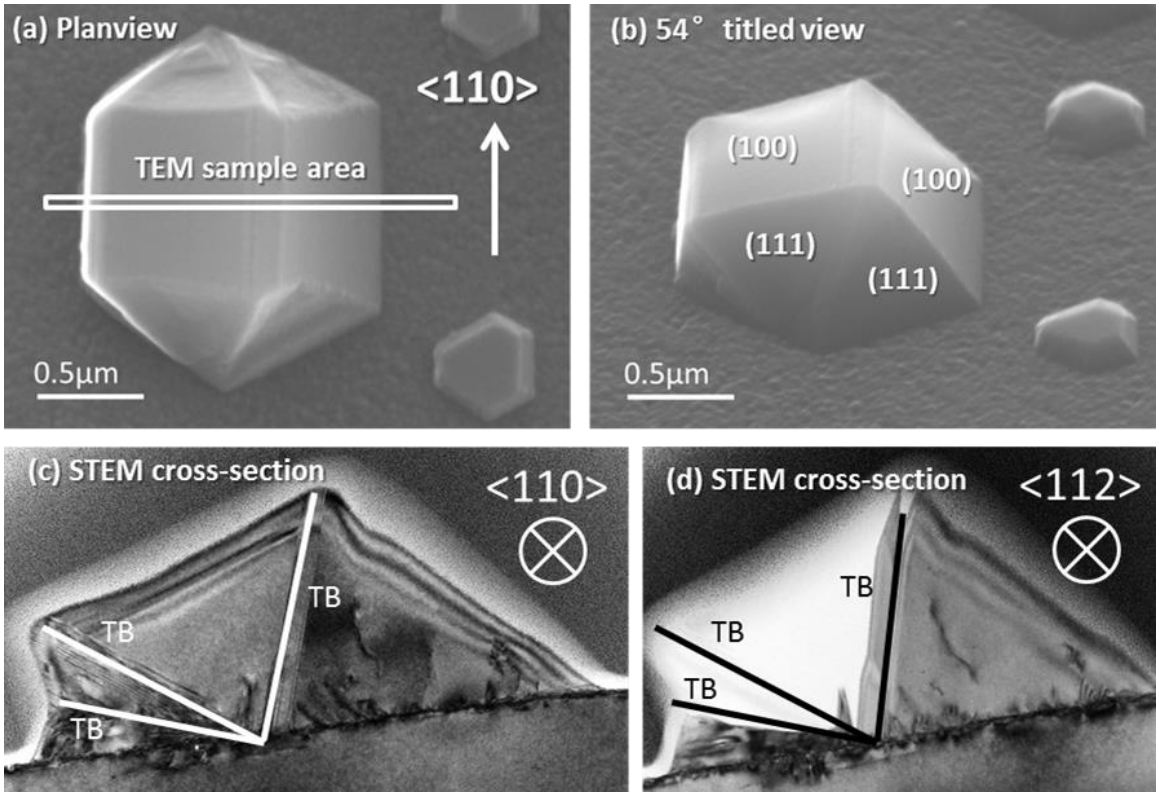

Figure 4-48. SEM and STEM overview images of the twinned truncated octahedral nucleus. (a). SEM image of the planview of the nuclei. TEM sampling area is labeled. (b). 54° tilted view of the nuclei. Some of the facet planes are indexed. (c) STEM image of the cross-section in [110] zone-axis. The nucleus is partitioned into 4 grains by 3 twin boundaries (TBs). (d) STEM image of the cross-section in [112] zone-axis. This can be obtained rotating the orientation of (c) by 30° about the normal direction of the basal plane. The two grains in the middle changed into white contrast because their (111) close packed planes are not parallel to the rotation plane, therefore, [112] zone-axis is not reached after rotation.

Figure 4-49 (a) is a STEM image of the twinned truncated octahedral nucleus. It consists of 4 grains with their (001) facets exposed to the outside. Grain 2 is the one-fold twin of grain 1, but they are not in contact with each other. Grain 3 is the one-fold twin of grain 2 and grain 4 is the one-fold twin of grain 3, they boundaries are in the form of stacking faults and microtwins. The overall result is that grain 4 is the three-fold twin of grain 1, therefore, a Σ27 grain boundary is formed between grain 4 and grain 1. (b) is the diffraction pattern of the whole area. There are four [002] diffractions corresponding to the four grains and they are perpendicular to the

respective (001) facets shown in (a). The [220] diffraction of grain 4 is also marked out to explain the (220) peak emerged in the XRD data. Because after a three-fold twinning, the (220) plane becomes parallel to the substrate surface plane which is 4° off the SiC [0001] direction. (c) is a HRTEM image of the interface. It shows the origin of the stacking faults and the microtwins. The substrate is relatively rough and non-uniform than epi-ready substrates and, therefore, some large angle vicinal steps exist. Different from crystal growth on large and smooth SiC terraces, BP grown on these large slopes suffer from much larger misfit and, therefore, more strain is generated. These stacking faults and microtwins are normally considered to be the results of strain relief. [52] Once the microtwins nucleate at these steps, they can grow into a large grain. (d) is a HRTEM image of the joint of grain 1, grain 3, grain 4 and the substrate. Grain 3 resulted from the evolution of the Microtwins. It is the two-fold twin of grain 1, thus their boundary is Σ9 type. (e) shows the Σ27 boundary between grain 4 and grain 1. The boundary appears as Σ27 Moire fringes instead of an easily-identifiable Σ27 boundary. The diffractogram inside is a combination of grain 1 and grain 4. The rotation angle is 31° which implies the Σ27 identity of the boundary.

Figure 4-49. Structural analysis of the twinned truncated octahedral nucleus. (a) is overview STEM image of cross-section. This nucleus consists of 4 grains with their (001) facets exposed to the atmosphere. (b) is the diffraction pattern of the whole area. There are four [002] diffractions corresponding to the four grains and they are perpendicular to the respective (001) facets shown in (a). The [220] diffraction of grain 4 is also marked out to explain the (220) peak in the XRD data. (c) is a HRTEM image of the interface. It shows the origin of the stacking faults and the microtwins. (d) is a HRTEM image of the joint of grain 1, grain 3, grain 4 and the substrate. Grain 3 resulted from the evolution of the Microtwins. It is the two-fold twin of grain 1, thus their boundary is Σ9 type. (e) shows the Σ27 boundary between grain 4 and grain 1. The boundary appears as Σ27 Moire fringes instead of an easily-identifiable Σ27 boundary. The diffractogram inside is a combination of grain 1 and grain 4. The rotation angle is 31°which implies the Σ27 identity of the boundary.

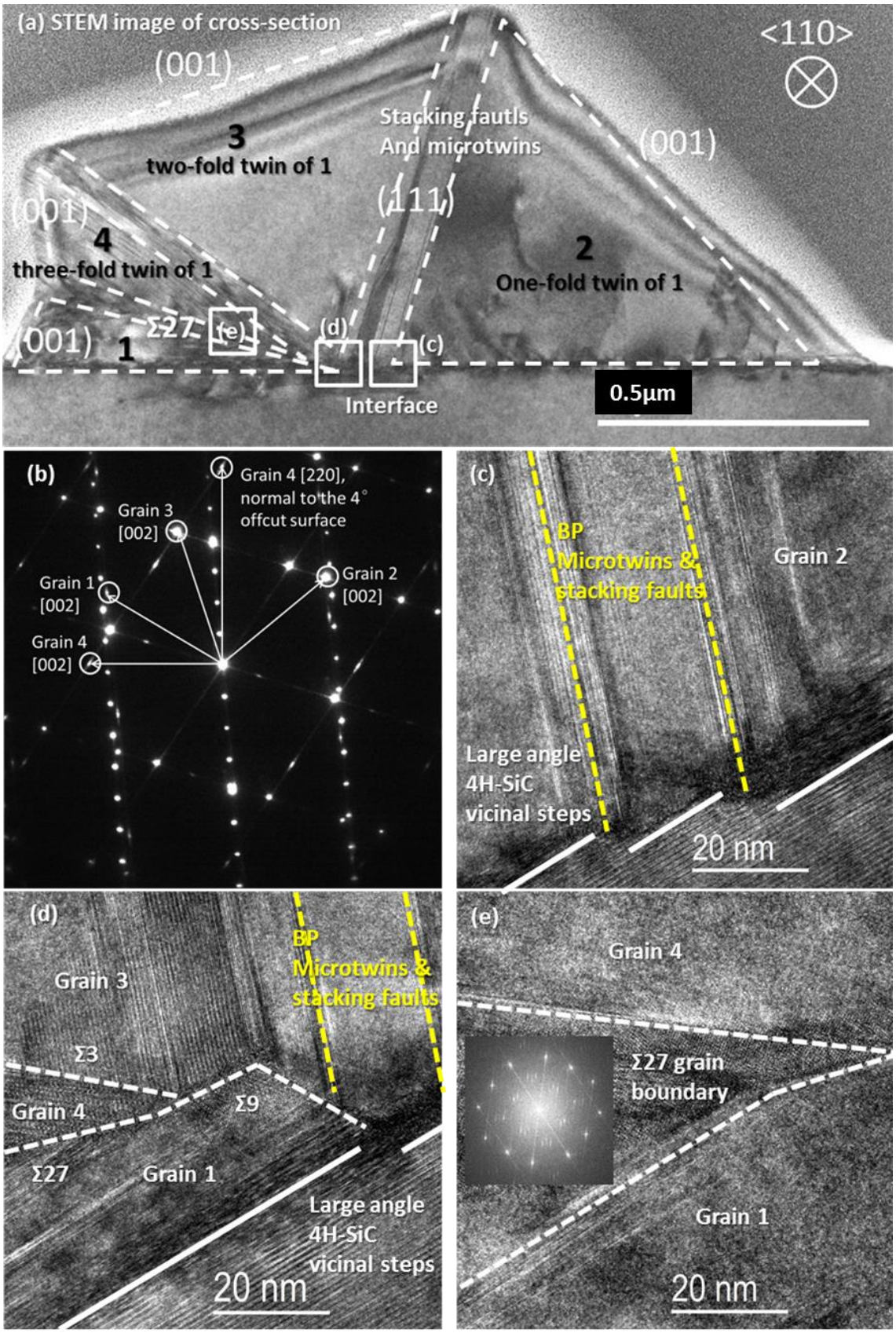
(a) STEM image of cross-section
(001)
<110>
3
two-fold twin of 1
Stacking fautls
And microtwins
(001)
(111)
(001)
4
three-fold twin of 1
2
One-fold twin of 1
Σ27
(e)
(d)
(c)
(001)
1
Interface
0.5µm
(b)
Grain 4 [220], normal to the 4° offcut surface
Grain 3 [002]
Grain 1 [002]
Grain 2 [002]
Grain 4 [002]
(c)
BP Microtwins & stacking faults
Grain 2
Large angle 4H-SiC vicinal steps
20 nm
(d)
Grain 3
BP Microtwins & stacking faults
Σ3
Grain 4
Σ9
Σ27
Grain 1
Large angle 4H-SiC vicinal steps
20 nm
(e)
Grain 4
Σ27 grain boundary
Grain 1
20 nm

The formation of this irregular shaped nucleus can be described as follows: Grain 2 nucleated first and kept growing till it expanded to the large angle vicinal steps. Then microtwins formed to release the strain caused by the large misfit at these steps, then grain 3 started to nucleate on the (111) facets of the microtwins and continued growth. At about the same time grain 1 nucleated and started growth till it met grain 3 and formed a Σ9 boundary. Again, to release the strain accumulated at the Σ9 boundary, twinning and stacking fault occured and caused the formation of grain 4. When grain 4 and grain 1 met, the above-mentioned Σ27 boundary was generated. This speculation is based on the energetic point of view. Because it is not possible for grain 4 and grain 3 to nucleate to top of grain 1 since Σ27 and Σ9 boundaries have much higher energies compared to the twinning energy of BP. The relationship between the grain boundary energy and misorientation angle of BP is not reported before, however, the work O. A. Shenderova [53] did with diamond and M. Kohyama [54] did with silicon can be used as a reference since they have the similar structures as BP. Figure 4-50 shows the plot of grain boundary energy versus misorientation angle of diamond and silicon. Apparently, Σ27 and Σ9 are energetic boundaries and cannot naturally initiate on the (111) facets of grain 1. Their formation should be due to the expansion of grain 3 and grain 4 which would inevitably cause their coalescences with grain 1 in the form of high-order grain boundaries.

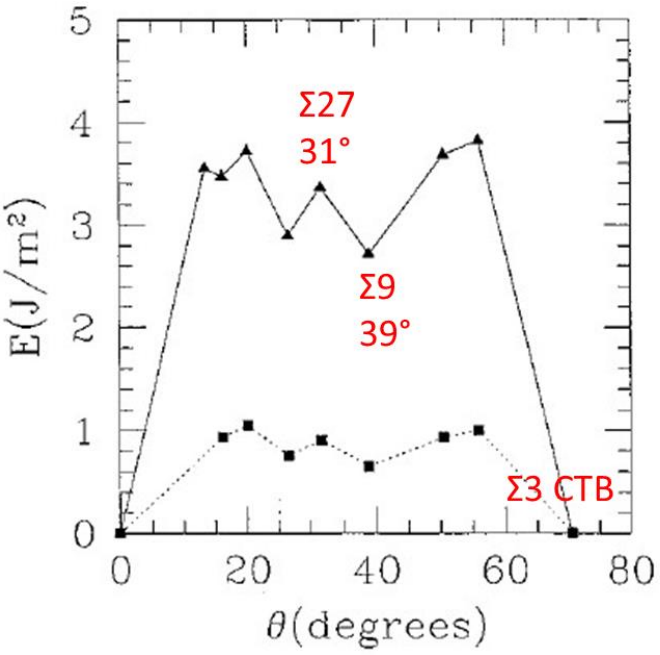

Figure 4-50. Energies of [110] symmetrical tilt grain boundaries for diamond (triangle) and silicon (square) in the misorientation range 0°≤θ≤70.53°. [ref 53 and 54]

To sum up, the origin of the irregular shape of this nucleus is the large step vicinal steps, or in other words, the rough surface and low twinning energy of BP. This kind of nucleus has more crystal orientations and, therefore, tends to induce more grain boundaries which are unfavorable for device performance. 4H-SiC substrate with epi-ready surface is supposed to suppress the number of this kind of nuclei.

4.4.4.3. Side topic: Hexagonal nanorods

Hexagonal nanorods are also observed in the middle of the film. We currently have no better control of their growth. These nanorods do not suit our thin-film detector purpose, however, the structures and origin of these rods can give us a better understanding of the growth mechanism as well as the material itself. Moreover, BP nanorods could potentially be used for designing pillar-structured neutron detector.

Figure 4-51 shows the distribution and morphology of the nanorods of Sample 83. (a) is the overview of the sample. The film is continuous and uniform except a small area (white rectangle) in the middle of the wafer. (b) is a low magnification SEM image showing the different morphologies of the continuous film and nanorod-rich region. (c) shows the a nanorod cluster sitting on top of the continuous film. The nanorods are all hexagonal. (d) shows clearly that the nanorods nucleate on top of the BP (111) facets instead of the SiC substrate.

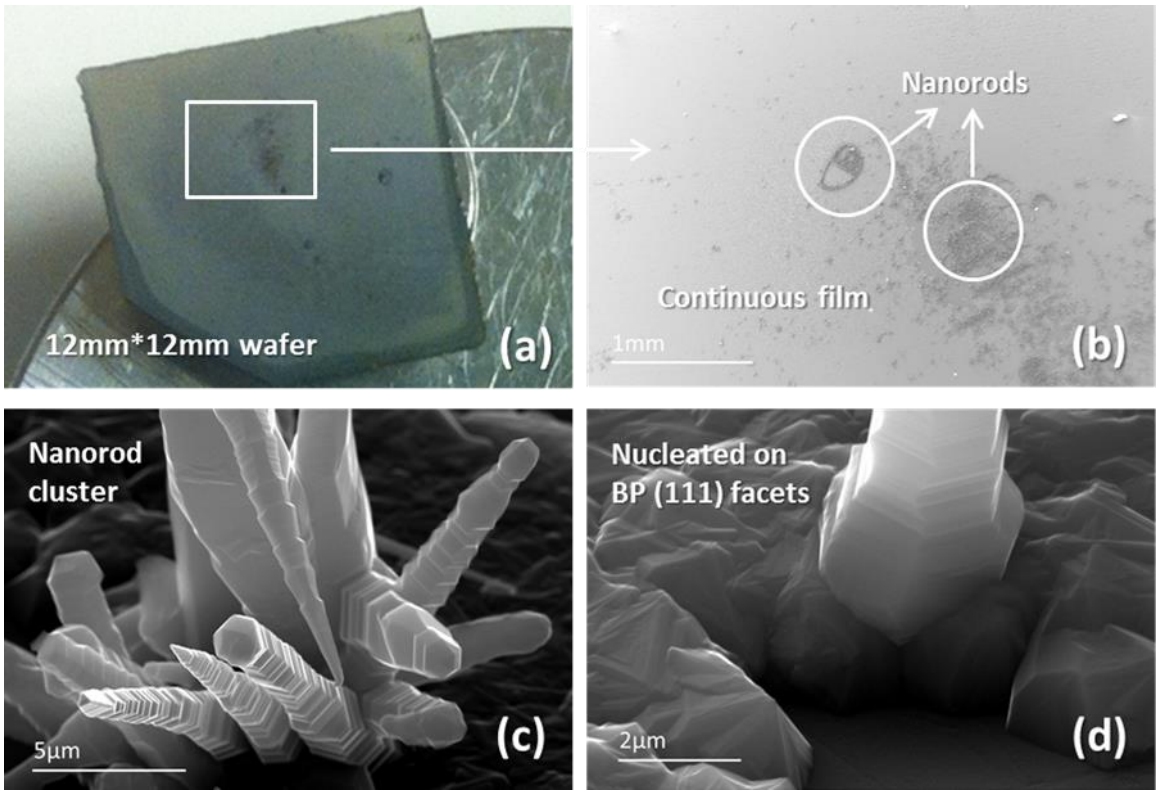

Figure 4-51. The distribution and morphology of the nanorods of Sample 83. (a) is the overview of the sample. The film is continuous and uniform except a small area in the middle of the wafer. (b) is a low magnification SEM image showing the different morphologies of the continuous film and nanorod rich region. (c) shows the a nanorod cluster sitting on top of the continuous film. The nanorods are all hexagonal. (d) shows clearly that the nanorods nucleate on top of the BP (111) facets instead of the SiC substrate.

Cross-section and plan-view TEM samples were both prepared for atomic-level investigations. The details are shown in Figure 4-52 and 4-53, respectively.

Figure 4-52 (a) is an SEM image of a nanorod standing on the substrate. This rod is a part of a broken rod which fell off onto the SiC substrate. It was not grown on the substrate. (b) and (c) are the STEM images of the cross-section of the nanorod in [110] and [112] zone axes, respectively. The surroundings are platinum layer deposited during sample preparation process. The wavy lateral edge of the rod is due to the frequently occurred twinning and stacking fault. (d) is a HRTEM image of the microtwins and stacking faults taken in [110] zone-axis. The inset diffraction pattern indicates that only two crystal orientations (See the atomic model) exist in the rod. The rod grows and tapers in the form of frequently twinning. (e) is the HRTEM image of the nanorod taken in [112] zone-axis, which can be obtained by rotating the sample by 30° about the growth direction. The columnar and streaked domains which represent microtwins and stacking faults in (d) disappeared because after a 30° rotation the twinned crystals and faulted stacks show the same structure (See the inset atomic model) and cannot be distinguished anymore. The inner diffraction pattern of (e) also agrees with the statement.

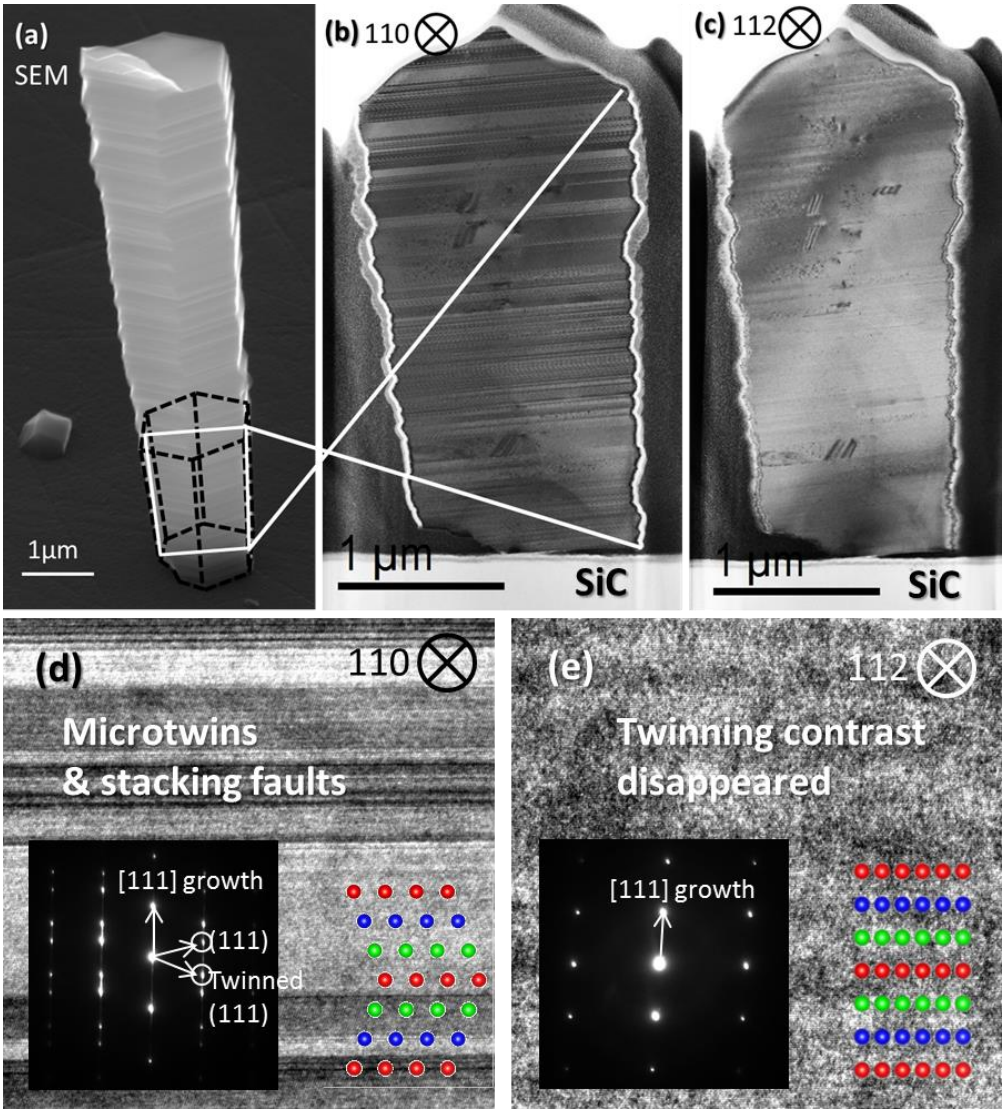

Figure 4-52. Cross-section analysis of the BP nanorod. (a) is an SEM image of a nanorod standing on the substrate. This rod is a part of a broken rod which fell off onto the SiC substrate. It's not grown on the substrate. (b) and (c) are the STEM images of the cross-section of the nanorod in [110] and [112] zone-axis, respectively. The surroundings are platinum layer deposited during sample preparation process. The wavy edge is due to the frequently occurred twinning and stacking fault. (d) is a HRTEM image of the microtwins and stacking faults in [110] zone-axis. The inset diffraction pattern indicates that only two crystal orientations exist in the rod. The rod grows and tapers in the form of frequently twinning. (e) is the HRTEM image of the nanorod in [112] zone-axis, which can be obtained by rotating the sample by 30° about the growth direction. The sharp columnar and streaked contrast observed in (d) disappeared because after a 30° rotation because the twinned crystals and faulted stacks show the same structure. (See the inset atomic model)

Figure 4-53 (a) is an SEM image of a nanorod plan-view. The dashed hexagon shows where the TEM sample is taken. (b) is a STEM image of the cross-section. The hexagon is divided into seven regions by three white dashed lines. As can be seen, there are three triangles that are filled with black spots, while all the other area seems clean and defect-free. If we consider this sample as the plan-view of nucleus 2 studied in chapter 4.4.4.1, then the possibility of these black spots being part of dislocation loops can also be excluded because they appear as spots in both view directions. Most probably these spots are precipitates formed during film deposition. Furthermore, the three triangles should be close to the (001) facets if this is consistent with the observation shown in Figure 4-44. (c) is the diffraction pattern of the (b). In addition to the normal (220) diffraction spots, the forbidden 1/3(224) spots are also observed. The presence of the forbidden diffractions is caused by stacking faults. [55] This phenomenon is further discussed in Figure 4-54. (d) is a high-magnification HRTEM image of the black spots. The diameter of these spots is below 10nm. The contrast should come from the strain field induced by the precipitates. More results are shown in Figure 4-55.

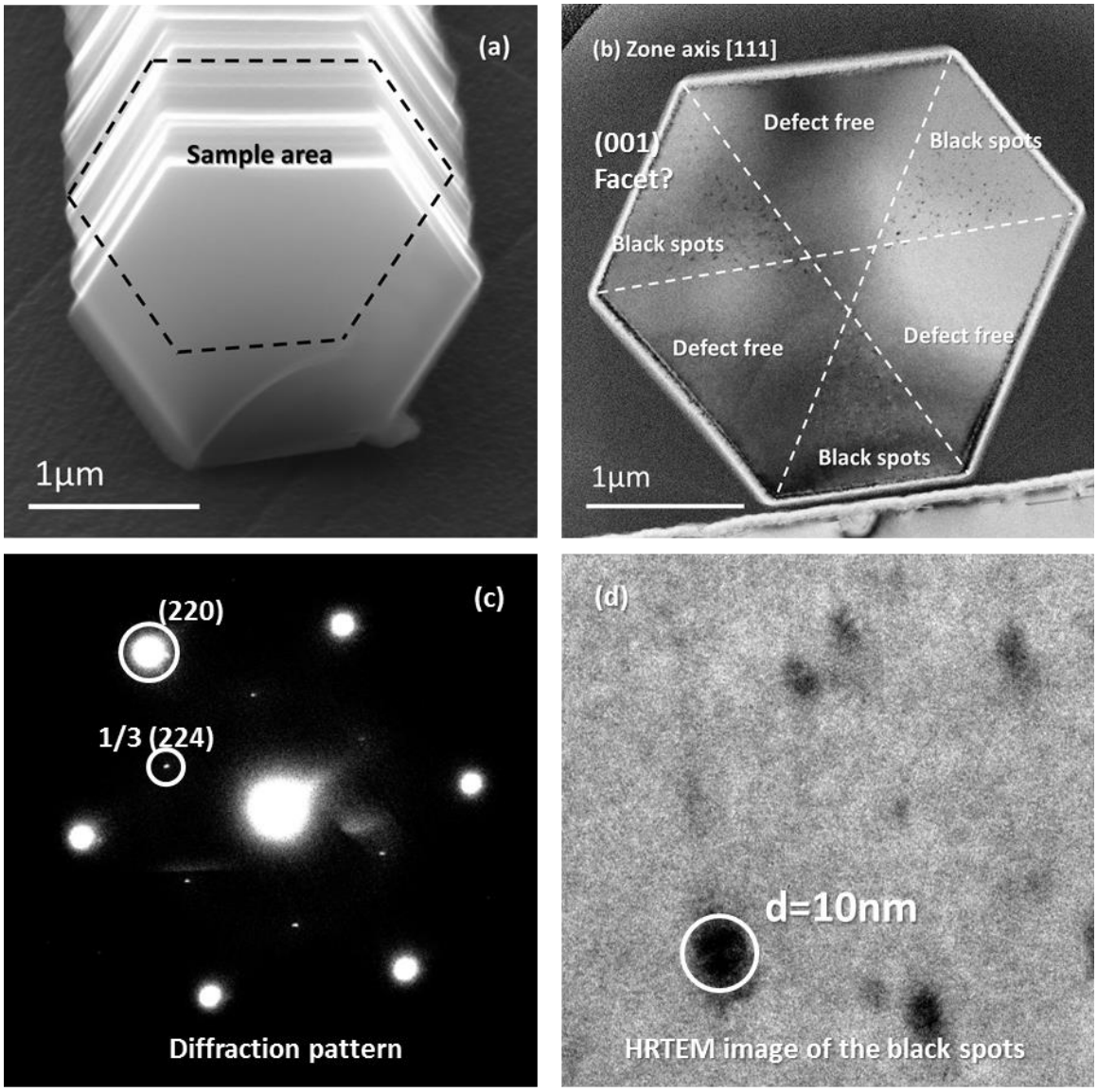

Figure 4-53. Plan-view analysis of the BP nanorod. (a) is an SEM image of a nanorod cross-section. The dashed hexagon shows where the TEM sample is taken. (b) is a STEM image of the cross-section. The hexagon is divided into seven regions by three white dashed lines. As can be seen, there are three triangles that are filled with black spots, while all the other area seems clean and defect-free. The three triangles should be close to the (001) facets if this is consistent with the observation shown in Figure 34. (c) is the diffraction pattern of (b). In addition to the normal (220) diffraction spots, the forbidden 1/3(224) spots are also observed. (d) is a high-magnification HRTEM image of the black spots. The diameter of these spots is below 10nm. They are most probably precipitates which induce a strain field around them.

Figure 4-54 shows the stacking fault analysis of the nanorod. (a) is a bight field STEM image of the cross-section in [111] zone-axis. The stacking faults are not discernible in this image. (b) is a dark field image acquired by imaging using the 1/3(224) diffraction beam circled in Figure 4-53 (c). The marked area should be the stacking fault area according to ref [46]. (c) is a bight field STEM image of the cross-section in [110] zone-axis. It can be obtained by rotating the sample by 35° about the [110] direction (see the atomic model shown in (a)). In this image, a clear stacking fault caused contrast can be seen. It matches well with the bright region of (b). (d) is the atomic model explains why the stacking faults can be mapped out in [110] zone-axis. Because the [110] incident beam can get strongly scattered at the stacking fault. However, this is not the case for the [111] incident beam because the atomic column spacing in its way does not change. This experiment also excluded the possibility that the black spots are related to the stacking faults because their distributions seem to be irrelevant.

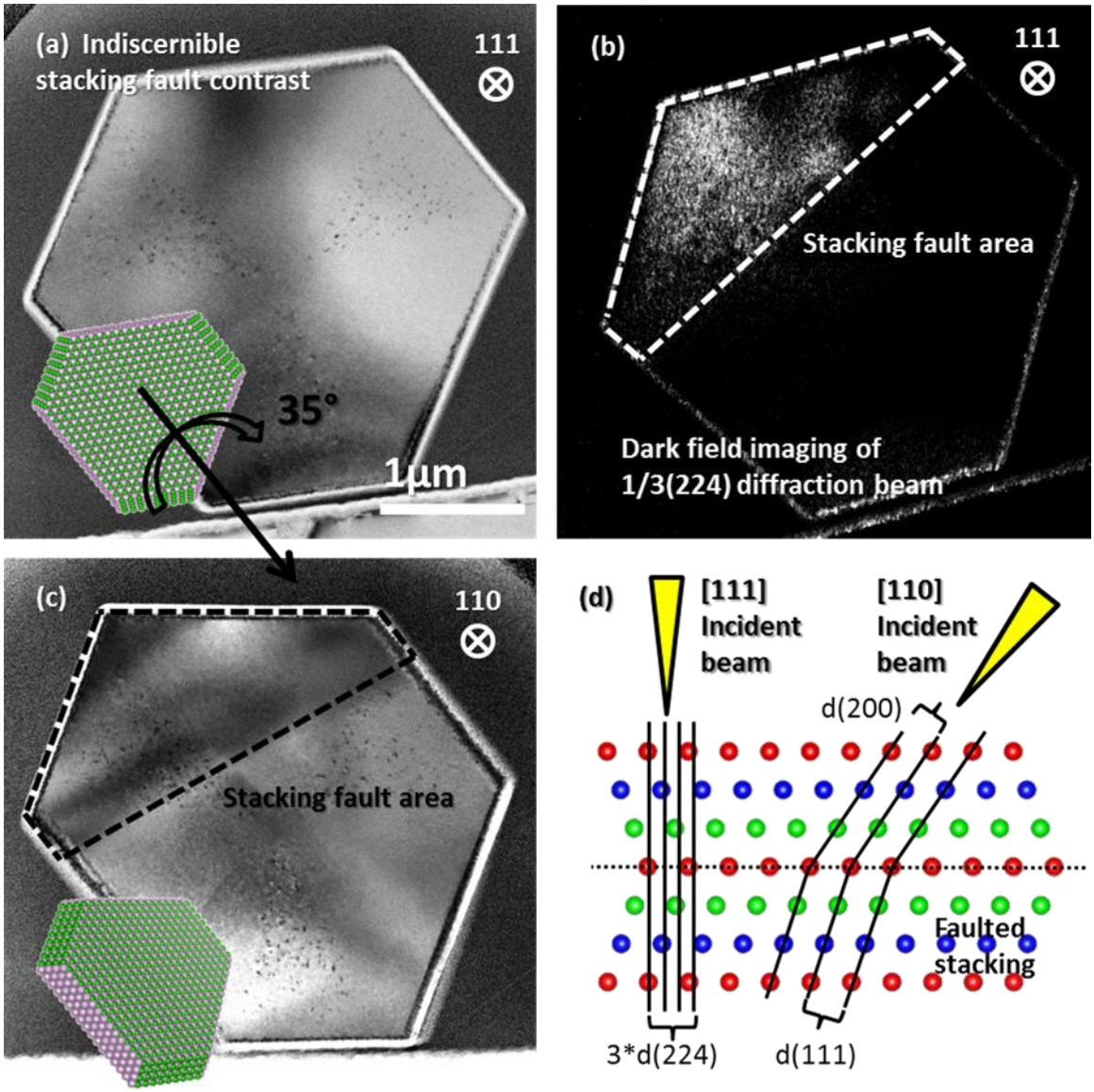

Figure 4-54. Stacking fault analysis of the BP nanorod. (a) is a bight field STEM image of the cross-section in [111] zone-axis. The stacking faults are not discernible in this image. (b) is a dark field image acquired by imaging using the 1/3(224) diffraction beam circled in Figure 4-54 (c). The marked area should be the stacking fault area according to ref [46]. (c) is a bight field STEM image of the cross-section in [110] zone-axis. It can be obtained by rotating the sample by 35° about the [110] direction shown in (a). In this image, a clear stacking fault caused contrast can be seen. (d) explains why the stacking faults can be mapped out in [110] zone-axis. Because the incident beam can get strongly scattered at the boundary induce by the stacking faults, which can be clearly seen in the atomic model. However, this is not the case for [111] incident beam since the atomic column spacing in its way does not change.

Now we will discuss more the black spots. It is hard to identify this kind of defect because little structure information can be resolved from the TEM images and no abnormal features are observed in the EELS spectrum taken at these spots. Figure 4-55 shows the 3D examination of the spots. The extra diffraction spot in Figure 4-55 (e) might imply the existence of another crystal phase or misorientated nanocrystals, but it is not convincible enough since the signal is so weak. However, some possibilities can be excluded according to the TEM images and EELS spectrums. For instance, the black contrast of the spots indicates a large strain field are generated which deflects the electron beam; the EELS spectrums make it clear that these black spots are not impurities. As was mentioned in the description of Figure 50, they are not dislocations either. It was reported that 3C-SiC precipitates in Si can be either coherent which means the periodicity is reserved, or incoherent which means a disordered lattice forms. [56] Therefore, it is possible that these black spots are misorientated BP nanocrystals. And there is another possibility that these black spots are some kind of BP precipitates with an unknown structure.

These precipitates were not observed in the 850° samples probably because the nucleus were much smaller compared to the 950° samples and they coalesced with each other very soon. It seems that a certain volume of the nucleus and a higher temperature is needed for their formation. According to Figure 4-53(b) and Figure 4-44, they tend to distribute near the three (001) facets and form a three-fold symmetry. As was shown in Figure 4-41, growth rate along [110] direction of the (001) facet is higher than that along [112] direction of the (111) facet. This suggests that growth rate variation might have contributed to the formation and distribution symmetry of these precipitates. Another thing is that, these precipitates only occur near the SiC/BP interface or in the hexagonal nanorods where BP crystal is largely strained. This implies that strain field might also be involved in the formation of these precipitates.

This kind of precipitate has never been reported before. According to results I have, large strain field, growth rate variation and temperature contributed to their formation and three-fold symmetric distribution.

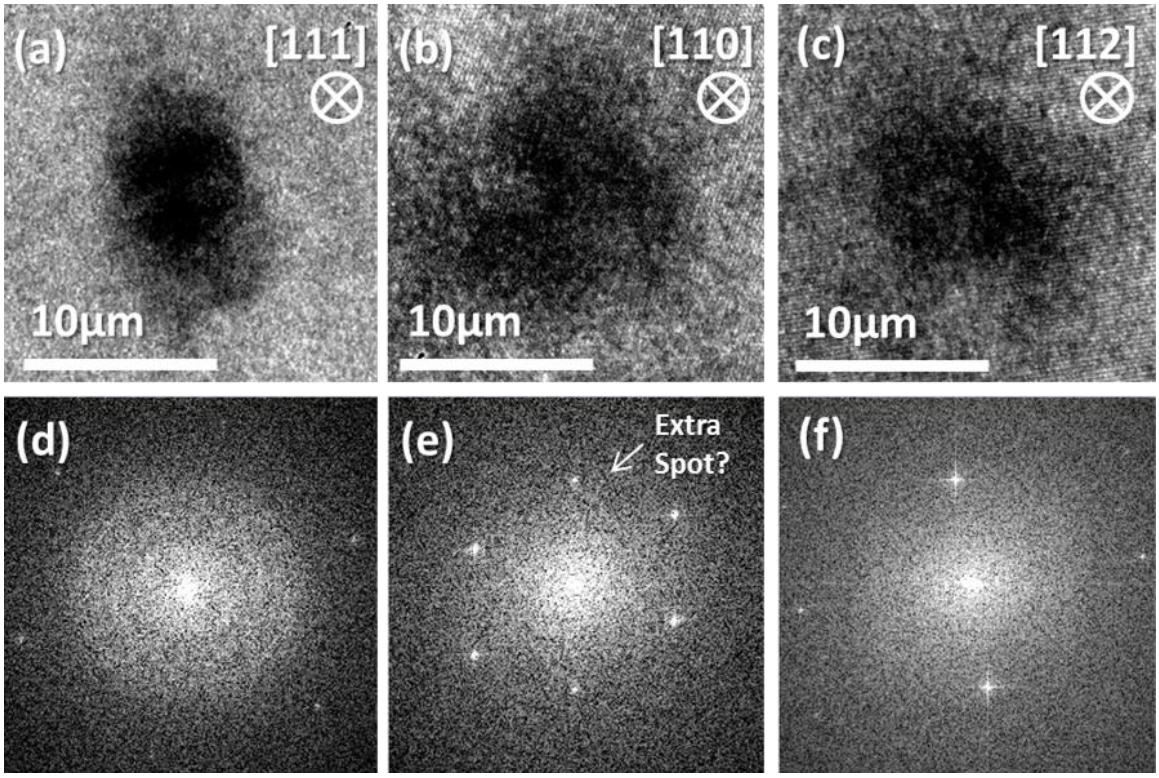

Figure 4-55. 3D-examination of the precipitates (black spots). The three spots are not from the same position. (a), (b), (c) are HRTEM images taken in [111], [110], [112] zone axes, respectively. (d), (e), (f) are the corresponding diffractograms of (a), (b), (c), respectively. There is a very weak extra spot in (e), which might imply the presence of another crystal phase or misorientated nanocrystals. But, this speculation is not convincible enough since the signal is so weak.

4.4.5. Summary

The film growth mechanism and defect origins are deduced via this study. If BP crystal grows on an amorphous layer, [111] growth dominates when the film thickness is less than 1.5μm; [111] and [220] growths are comparable when film

thickness in the range of 1.5μm to 2.5μm; [220] growth dominates when the film thickness is larger than 2.5μm. The advantage of [111] over [220] growth during the early stage should be due to the larger amount of [111] nuclei. The reason for the reversion after 2.5μm is because [220] is the fastest growth direction and it will eventually block [111] growth and dominate the growth. While, if BP crystal grows epitaxially on the basal plane of SiC, [111] growth dominates the early stage due to the SiC (0001), [11-20] // FCC BP (111), [1-10] epitaxial relationship. Deviation occurs as the film grows because of twinning and crystal coalescences. The former causes Σ3n grain boundaries, "n" is the number of twinning fold. The latter causes random columnar growths at the coalescing boundaries of the nuclei, the [220] columnar growth is faster than all the others and will become the dominating growth eventually. Since however large the grain size is, they have to coalesce eventually, the best stratagem is to maximize the grain size to reduce the boundaries. 950°C is tested to be a good temperature to obtain large grains and further tuning will be necessary. The Defect types and distributions, origins, interpretations and improvement strategies are summarized in Table 4-6.

Table 4-6. Defect types and distributions, origins, interpretations and improvement strategies.

Defect type and distribution	*Origin*	*Interpretation*	*Improvement strategy*
Misfit dislocations, Σ3 CTBs and (111) planar defects at the interface	Lattice-mismatch	Result of lattice-mismatch strain relief	Not variable for the studied BP/4H-SiC system
Non-epitaxial microtwins at the interface	Surface roughness	Result of strain relief at large-angle vicinal steps	Use epi-ready SiC substrates
Σ3 ITBs, Moire fringes near the interface	Coalescence of "ABC" and "ACB" growths	Common phenomenon for 3-fold symmetric plane growth on 6-fold symmetric surface	Refine growth temperature to obtain large nuclei. 950°C seems to be favorable, further tuning is possble.
Precipitates near the interface	Growth rate variation between different facets and strain field	Possibly due to Adatoms mobility variation between different regions, but not sure.	Not variable for the studied BP/4H-SiC system
Σ3 CTBs, Moire fringes, (111) planar defect s, Grain boundaries, Σ3, Σ9, ... Σ3n ITBs and dislocations within the film	Low twinning and stacking fault energy of BP, and inevitable crystal coalescence.	Σ3 CTBs, Moire fringes and stacking faults are direct results. Σ3n ITBs are formed when twinned crystals meet. Dislocations are products of strain relief originated at the grain boundaries	Growth temperature refinement is found to be able to suppress twinning and (111) planar defects. BP grains are much larger at 950°C, therefore, less defective. Further tuning is possible.

4.5. Optimized BP growth on SiC

As was mentioned above, all the C-face substrates are actually the backside of the Si epi-ready wafers and good quality BP films were obtained. According to the defect analysis and initial stage study, C epi-ready wafer should further improve the film quality. In this chapter, epitaxial BP (sample 85) grown on C epi-ready wafer at

950°C with all the other parameters optimized is characterized. It turned out this is the best sample so-far.

4.5.1. SEM and XRD examinations

SEM and XRD results are shown in Figure 4-56. Basically all the nuclei have truncated octahedral shapes. Irregular shapes like the twinned truncated octahedrons and icosahedrons can hardly be found. Also the surface of the continuous film is quite smooth and packed with coherent triangular BP (111) mesas. The XRD results indicate that excellent epitaxy is achieved. Both the SEM and XRD results imply an appreciable improvement is achieved on this sample compared to sample 83 which was considered to be the best before.

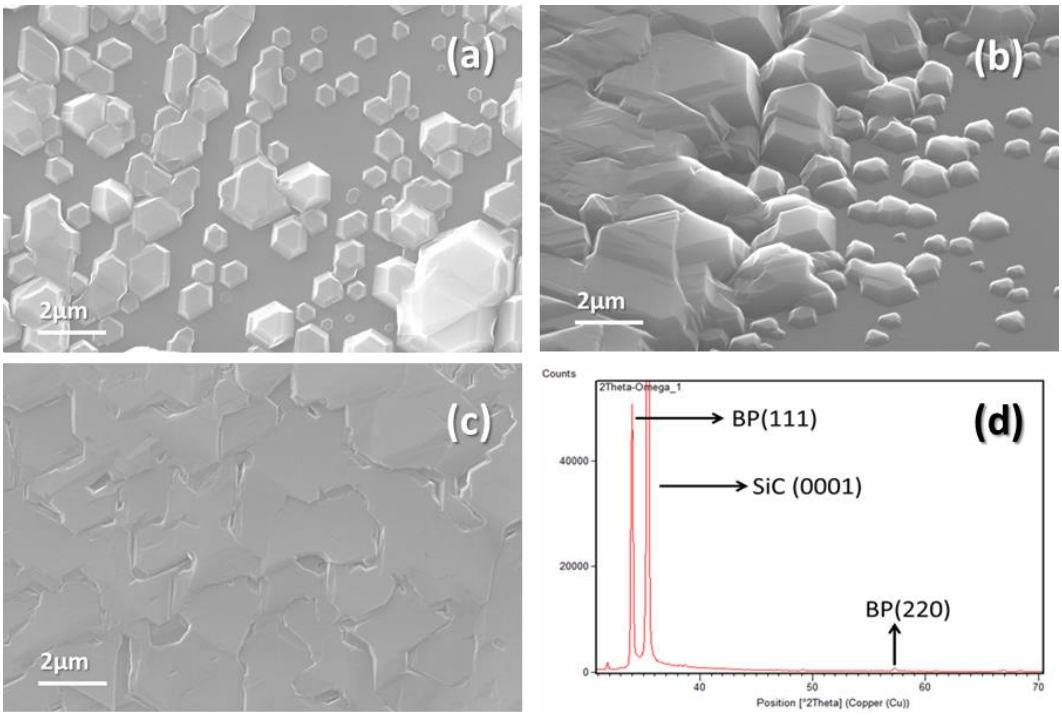

Figure 4-56. SEM and XRD examinations of the optimized sample (#85). (a) plan-view of the nuclei. All the nuclei have truncated octahedral shapes. (b) 54° tilted view of the nuclei. (c) plan-view of the continuous film. The surface is smooth and packed with coherent triangular BP (111) mesas. (d) XRD pattern of the film. Excellent epitaxial BP film is obtained.

4.5.2. TEM examination

Though the morphology and XRD results all show improvements compared to sample 83 which was grown on the backside of Si-face epi-ready SiC substrate, TEM analysis is still needed to show how the microstructure evolution changes since the material performance is closely related to the structures. Cross-section TEM sample was prepared via FIB and investigated with our Zeiss Libra 200 TEM. Electron diffraction experiments are performed on selected areas to reveal the structure and orientation information. The results are organized in Figure 4-57.

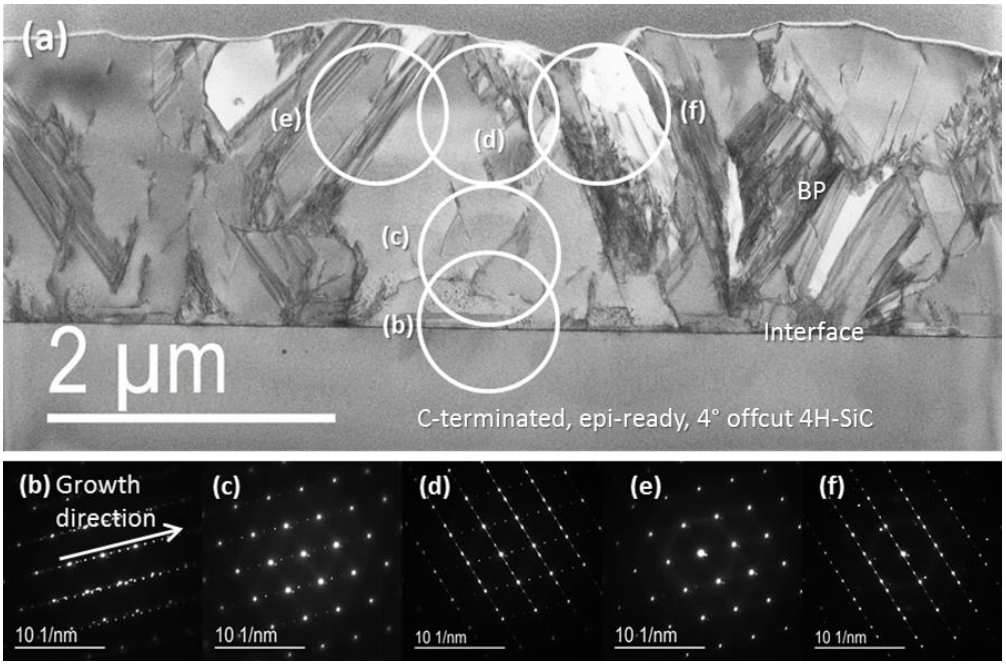

Figure 4-57. TEM and SAD examinations of the optimized sample (#85). (a) STEM overview of the cross-section in [110] zone-axis. (b) is from the interface. Apparently, BP grew epitaxially on SiC since BP (111) spot overlapped with SiC (0001) spot. (c) is the diffraction of the near-interface region. It consists of a set of strong BP [110] diffraction and a set of weak twinned diffraction. (d) More twinning orientations are observed and their diffraction patterns have about the same intensity. (e) looks like a perfect BP [110] diffraction even though some stripes are included by the aperture. The stripes are not stacking faults, dislocation loops or twin boundaries since they do not lie on (111) planes. The details are shown in Figure 4-58. (f) comes from an area with two grains with an incoherent grain boundary. This is why the extra spots did not take any twinning diffraction sites in the pattern.

Figure 4-57 (a) is a STEM overview of the cross-section in [110] zone-axis. The white circles represent the approximate positions of the SAD apertures. Most of the striped contrast in the image indicates Σ3 CTBs, or (111) planar defects like stacking faults and dislocation loops. The amount of these planar defects is decreased compared to the previously examined samples in which they started at the interface and densely distributed within the film. The separated white contrast in the film represents grains out of [110] zone-axis, which we named growth deviation in 4.3. They are formed by twinning or crystal coalescence. The ratio between the white area and the gray area which means on-axis crystals is much lower compared to the samples studied before. This means incoherent boundaries are decreased and this should benefit the electrical properties of the material. (b) is the SAD pattern of the interface. Apparently, BP grew epitaxially on SiC since BP (111) spot overlapped with SiC (0001) spot. (c) is the diffraction of the near-interface region. It consists of a set of strong BP [110] diffraction and a set of weak twinned diffraction which comes from the small amount of microtwins formed at the interface. (d) is the diffraction of the near-surface region. More twinning orientations were observed and their diffraction patterns have about the same intensity which implies that the volumes of the mutually twinned crystals were comparable. The diffuse streaks connecting the diffraction spots resulted from the (111) planar defects and twin boundaries. (e) looks like a perfect BP [110] diffraction even though some stripes are included by the aperture. Actually these stripes are not Σ3 CTBs, stacking faults or dislocation loops which are supposed to lie on the (111) planes, instead, they are parallel to [110] direction. That's why no mirrored diffractions were observed in the pattern. More details will be discussed in Figure 4-58. (f) comes from an area with two grains with an incoherent grain boundary. This is why the extra spots did not take any of the twinned diffraction sites in the pattern.

They types of defect and how they distribute are also studied since they are closely related to the performance of the material. Figure 4-58 shows a collection of the most common defects in this film.

Figure 4-58 shows the defect demonstrations of sample 85. All images are taken in [110] zone-axis. The scale bar in (e) applies for all the other images. Figure (a) shows the BP/SiC Interface. Microtwin (MT) is formed near the interface to release the in-plane strain induced by the misfit. (b) also shows BP/SiC Interface. However, different from (a), Stacking faults (SFs) and small Microtwins (MTs) are generated at the interface to release the strain. In (c), we found that precipitates are again observed at the near-interface region. (d) shows that SFs and MTs originate from Σ3 ITB. They sometimes serve as grain boundaries. (e) shows how Σ3 ITB and Σ3 CTB correlate with each other. (f) shows a Σ9 grain boundary between an original grain and its two-fold twin. (g) shows a short dislocation blocked by the Σ3 ITB. (h) shows that some [220] columnar growths are observed at grain boundaries. A large-scale image of the [220] columns can be found in the aperture position (e) in Figure 4-57 (a). (i) is an incoherent grain boundary. The right grain is in [110] zone-axis, while the left one is not. The left grain should come from twinning of a grain in the other view direction.

4.5.3. Summary

SEM, XRD and TEM examinations all suggest that a great improvement is achieved on the crystal quality of the BP film. The surface is much smoother, the epitaxial content weighs more and the growth deviation is reduced to a large extent. The defect types are basically the same as was characterized in sample 45. However, the distribution and amount vary. The incoherent boundaries becomes less and most of film is in-axis, this means the charging trapping centers should decrease compared to sample 83 which was considered the best before sample 85.

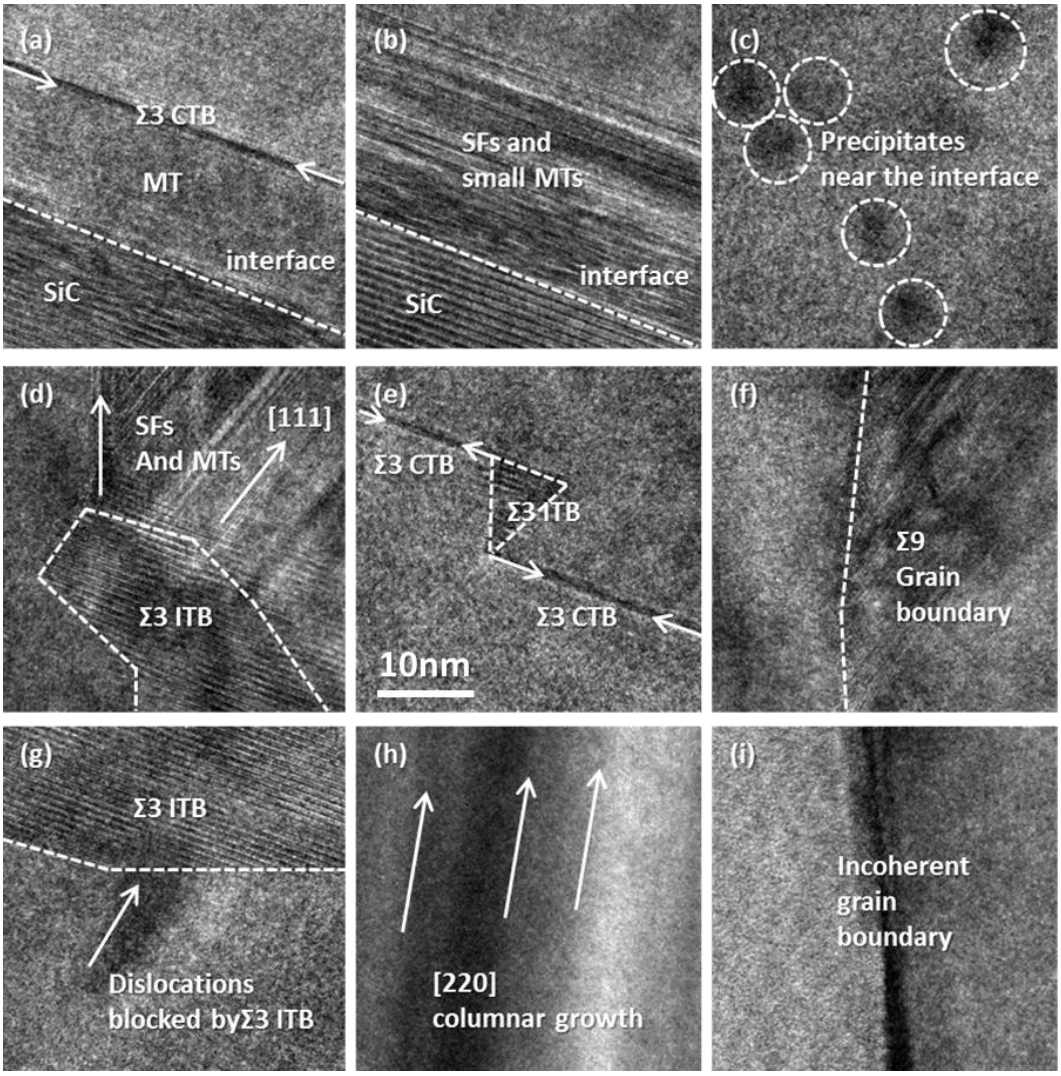

Figure 4-58. Defect demonstrations of the optimized sample (#85). All images are taken in [110] zone-axis. The scale bar in (e) applies for all the other images. Figure (a) shows the BP/SiC Interface. Microtwin (MT) is formed near the interface to release the in-plane strain induced by the misfit. (b) BP/SiC Interface. Different from (a), Stacking faults (SFs) and small Microtwins (MTs) are generated at the interface to release the strain. (c) Precipitates are again observed at the near-interface region. (d) Σ3 ITB is common in the film. And SFs and MTs always originate from Σ3 ITB and they sometimes serve as grain boundaries. (e) shows how Σ3 ITB and Σ3 CTB correlate with each other. (f) shows a Σ9 grain boundary between an original grain and its two-fold twin. (g) shows a short dislocation blocked by the Σ3 ITB. (h) Some [220] columnar growths are also observed at grain boundaries. (i) An incoherent boundary. The right grain is in [110] zone-axis, while the left one is not. The left grain should come from twinning of a grain in the other view direction. It might induce a Σ9 or Σ27 boundary within the twinning plane but not the present one.

4.5.4. Discussion

This success of sample 85 should be attributed to the smooth offcut surface of the SiC wafer since it is the only factor that was changed compared to sample 83. Now we will look at the interface of this sample and find out what difference the smooth surface make compared to the rough surface of sample 83. Figure 4-59(a) is a Z-contrast image of sample 85 in which BP is grown on C-face 4° offcut 4H-SiC with smooth surface. (b) is a Z-contrast image of sample 83 in which BP is grown on C-face 4° offcut 4H-SiC with rough surface. (c) is a HRTEM image of the interface of sample 85. As can be seen, the microtwins lie parallel to the basal plane of SiC. (d) is a HRTEM image of the interface of sample 85. The microtwins originate at the large-angle vicinal steps of the SiC and they lie 71° off the basal plane of SiC. The decrease of the 71° microtwins in sample 85 is apparently due to the smooth surface, or to be specific, the uniformly distributed vicinal steps and large terraces.

As was mentioned in chapter 4.4.4.2, microtwins normally play the role of strain relief. The orientation of the microtwins should be closely related to that of the strain field. This will be where vicinal steps come in. In addition to the lattice mismatch, the slope and size of a vicinal step to a large extent affect the generated strain field. The lattice-mismatch strain field on a large SiC terrace is parallel to the basal plane of SiC, while the strain field generated due to BP growth at the steps has more upward components because the atom arrangement at the steps are more complex than simply distributing within a plane. Extend distortion occurs at the vicinal steps. The atomic models are shown in Figure 4-60. Figure 57(a) shows BP growth on a smooth 4H-SiC surface with a small offcut angle. Most of the strain is generated due to the in-plane lattice mismatch. Therefore, microtwins formed close and parallel to the basal plane of SiC to release the strain (Misfit dislocations are another way of releasing this strain). Figure 57(b) shows BP growth on large-angle 4H-SiC vicinal steps which randomly distribute on a rough surface. In this model, the SiC terrace is so small that most the strain originates at the steps. The generated strain field has a much larger upward component than the horizontal component.

The upward component is then released by forming microtwins along the other close-packed plane which is 71° with respect to the basal plane. Microtwins are not able to form horizontally because the terraces are too small for them to effectively release the strain. Therefore, strain energy is stored at these steps.

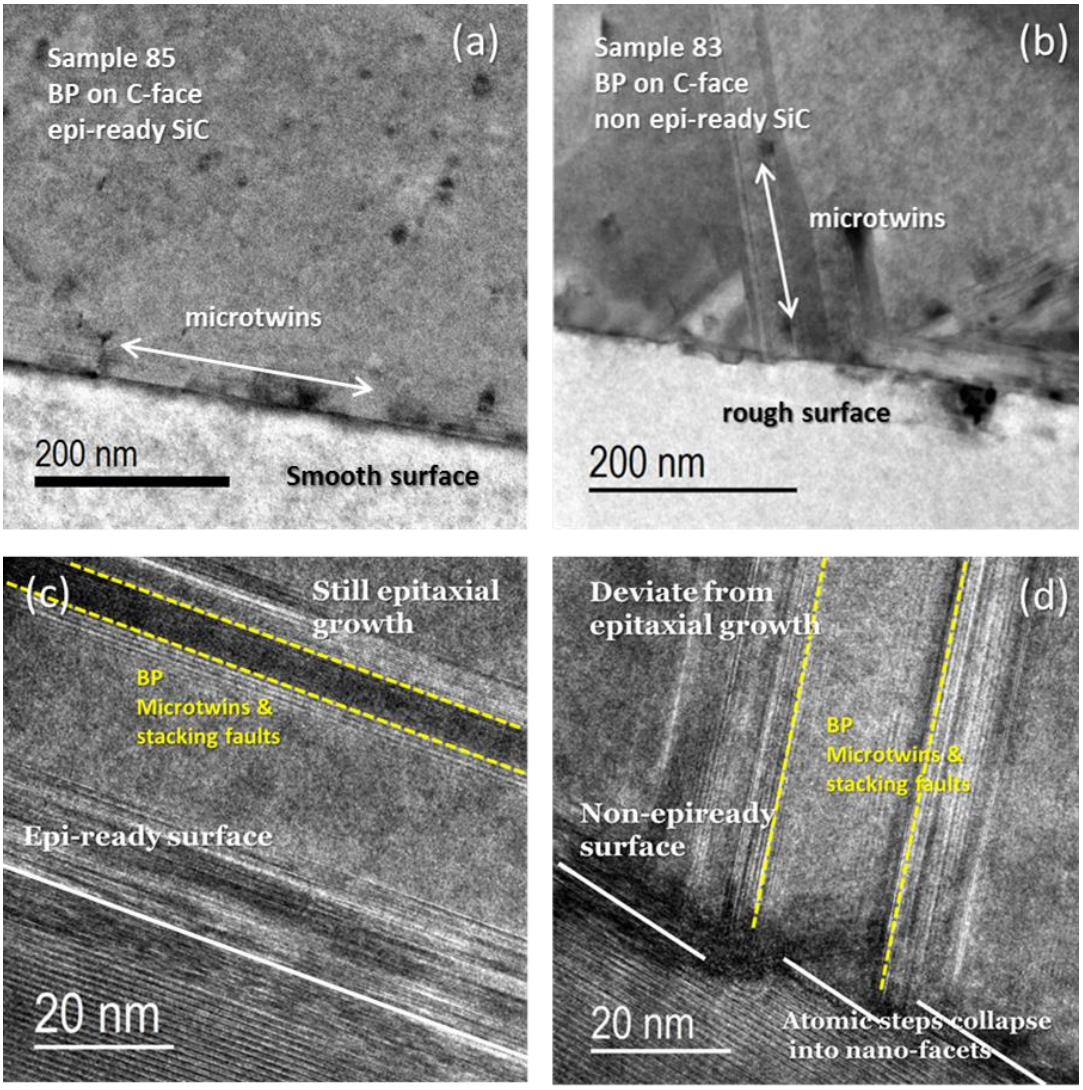

Figure 4-59. Interface investigation of the optimized sample (#85). (a) Z-contrast image of sample 85. BP is grown on C-face 4° offcut 4H-SiC with smooth surface. (b) Z-contrast image of sample 83. BP is grown on C-face 4° offcut 4H-SiC with rough surface. (c) HRTEM image of the interface of sample 85. The microtwins lie parallel to the basal plane of SiC. (d) HRTEM image of the interface of sample 85. The microtwins lie parallel to the (111) plane of a epitaxial BP grain instead of the basal plane of SiC.

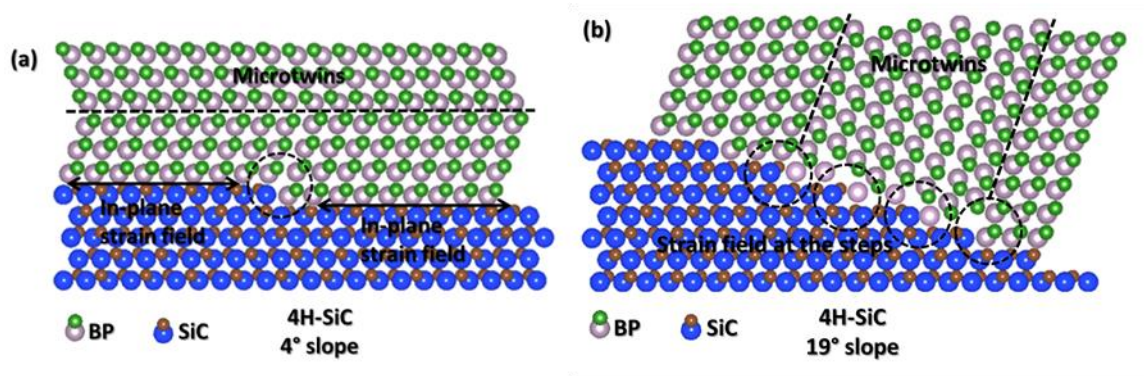

Figure 4-60. Atomic models of BP growth on a smooth surface and a large-angle vicinal SiC surface. (a) shows BP growth on a smooth 4H-SiC surface with a small offcut angle. Most of the strain is generated due to the in-plane lattice mismatch. Therefore, microtwins formed close and parallel to the basal plane of SiC to release the strain. Figure 4-60(b) shows BP growth on 4H-SiC with a large offcut angle. In this model, the SiC terrace is so small that most the strain originates at the steps. The generated strain field has a much larger upward component than the horizontal component. The upward component is then released by forming microtwins along the other close-packed plane which is 71° with respect to the basal plane. However, microtwins are not able to form horizontally because the terraces are too small for them to effectively release the strain. Therefore, strain energy is stored at these steps.

CHAPTER 5. CONCLUSIONS AND DISCUSSIONS

In conclusion, the optimized growth conditions, film growth mechanism and defect origination mechanism are all explained for the BP/4H-SiC system based on the extensive experimental results and thorough structural analysis.

The best BP film was grown at 950 °C on a C-face epi-ready 4H-SiC wafer with 4° offcut and the gas flow rates were 1% B_2H_6 in H_2 at 20sccm, 5% PH_3 in H_2 at 100sccm and H_2 at 2500sccm. Further fine tuning of the growth parameters may further improve the film quality.

The film growth mechanism can be summarized as follows: If a BP crystalline film grows on an amorphous layer: [111] growth dominates when the film thickness is less than 1.5μm; [111] and [220] growths are comparable when film thickness in the range of 1.5μm to 2.5μm; [220] growth dominates when the film thickness is larger than 2.5μm. The advantage of [111] over [220] growth during the early stage should be due to the larger number of [111] nuclei. The reason for the reversion after 2.5μm is because [220] is the fastest growth direction and it will eventually block [111] growth and dominate the growth. If the BP crystals grow epitaxially on the basal plane of SiC, [111] growth dominates the early stage due to the SiC (0001), [11-20] // FCC BP (111), [1-10] epitaxial relationship. Deviation occurs as the film grows because of twinning and crystal coalescence, and the deviated crystal cause grain boundaries. The former induce Σ3n grain boundaries, “n” is the number of twinning fold, while the latter causes random columnar growths at the coalescing boundaries of the nuclei, the [220] columnar growth is faster than all the others and will become the dominating growth eventually.

Lattice mismatch, low twinning and stacking fault energy, frequently alternating “ABC” and “ACB” growths, grow rate variation between growth directions and surface roughness are responsible for the defect originations. Lattice mismatch is inherent in the BP/SiC system and not variable. The lattice-mismatch strain relief process brings about twins, stacking faults, accompanied dislocation loops and

misfit dislocations at the interface. Low twinning and stacking fault energies and frequent variation of stacking-sequences directly result in stacking faults, dislocation loops, coherent twin boundaries and indirectly result in dislocations and incoherent grain boundaries. Their influences can be controlled via temperatures. For instance, many fewer twin boundaries and stacking sequence variations were observed in the 950°C sample compared to the 850°C sample because the grain size is much larger. Further tuning is possible. Growth rate differences between different growth orientations and a relatively large strain field are presumably two necessary factors for the formation of the precipitates. Because the precipitates are only observed either near the highly-strained BP/SiC interface or in the highly-strained hexagonal nanorods and their distribution within the (111) atomic planes has a three-fold symmetry. A rough surface normally contains randomly distributed large-angle vicinal steps which cause complex strain fields extending around. The complex strain fields lead to the formation of microtwins, stacking faults or potentially dislocations which are not observed though. The effect of surface roughness is overcome by using epi-ready SiC wafers. The initial stage of the growth is critical to film growth.

Good BP epitaxial film on SiC was obtained, fully characterized and well understood. Crystal coalescence is inevitable and causes random crystal growth at the coalescing boundaries. Twinning, (111) planar defects like stacking faults and dislocation loops are the major defects and they directly or indirectly brings about some other defect like dislocations and grain boundaries. However, a high twin concentration itself might not degrade the electrical properties according to Alexander's experiment on 3C-SiC which has the same atomic structure as BP. [57] Therefore, the film might still be well suited for detector uses. Actually, a superior design is to perform BP growth on [110] orientated 3C-SiC or some other FCC materials with small lattice mismatches with BP. In this way, not only the stacking-sequence variation can be eliminated at the interface, a faster growth can be achieved. This is also supposed to solve the precipitate problem since all the nuclei would grow equally in the form of

crystal columns in one direction. However, this kind of substrate is not available yet and threading dislocation is another concern. We will have to stick to the BP/SiC system which is so far the most appropriate system and keep optimizing the growth parameters to maximize the epitaxial content of the film.

CHAPTER 6. FUTURE WORK

(1). Keep optimizing growth parameters for BP/4H-SiC system to further improve the film quality and at the same time make sure it is reproducible.

(2). Search for [110] orientated 3C-SiC or some other FCC materials with small lattice mismatches with BP and try film growth on them.

(3). Perform TEM and electrical measurements synergetically to correlate the defect type and density with electrical performances.

(4). Grow thicker films for neutron irradiation test.

REFERENCES

[1]. Douglas S et al, Nuclear Instruments and Methods in Physics Research A 517 (2004) 180–188.
[2]. G.F. Knoll, Radiation Detection and Measurement, 3rd Edition, Wiley, New York, 2000.
[3]. Robertson, B.W et al, Applied Physics Letters 80 (2002) 3644.
[4]. Nina Hon et al, J. Phys. D: Appl. Phys. 43 (2010) 275101.
[5]. A N Caruso, J. Phys.: Condens. Matter 22 (2010) 443201 (32pp)
[6]. Nikolic, R.; Conway, A. Fabrication of Pillar-structured thermal neutron detectors. IEEE Nuclear Science Symposium Conference Record 2007, 2, 1577–1580.
[7]. Yukinobu Kumashiro, "Electric Refractory Materials", CRC Press 2000, Print ISBN: 978-0-8247-0049-2.
[8]. J.C. Lund, F. Olschner, F. Ahmed and K.S. Shah, Mat. Res. SOC. Symp. Proc., 162, 601 (1990).
[9]. Y. Kumashiro, J. Mater. Res., 5(12), 2933 (1990).
[10]. Michael Fitzsimmons, Roger Pynn, A proposal for Fabrication of Boron-Phosphide Neutron Detectors.
[11] S. Weissmantel (1999). "Microstructure and Mechanical Properties of Pulsed Laser Deposited Boron Nitride Films". Diamond and Related Materials 8 (2–5): 377. Bibcode 1999DRM.....8..377W. doi:10.1016/S0925-9635(98)00394-X.
[12] G. Leichtfried et al, (2002). "13.5 Properties of diamond and cubic boron nitride". In P. Beiss et al,. Landolt-Börnstein – Group VIII Advanced Materials and Technologies: Powder Metallurgy Data. Refractory, Hard and Intermetallic Materials. 2A2. Berlin: Springer. pp. 118–139.
[13]. N. Hong, J. Mullins, K. Foreman, and S. Adenwalla, Boron carbide based solid state neutron detectors: the effects of bias and time constant on detection efficiency," Journal of Physics D: Applied Physics, vol. 43, no. 27, p. 275101, 2010
[14]. H. Werheit et al, Journal of Physics: Condensed Matter, vol. 18, no. 47, p. 10655, 2006.

[15]. Terry L. Aselage, Ralph G. Tissot, Journal of the American Ceramic Society, Volume 75, Issue 8, pages 2207–2212, August 1992
[16]. UGOCHUKWU NWAGWU, Dissertation. Kansas State University (2013)
[17]. Zhenlin Liu et al, Journal of Electron Spectroscopy and Related Phenomena 135 (2004) 73–81
[18]. T. Udagawa, M. Odawara, and G. Shimaoka, Appl Surf Sci 244, 285 (2005).
[19]. T.L. Chu, J.M. Jackson, A.E. Hyslop, and S.C. Chu, J Appl Phys 42, 420 (1971).
[20]. T. Yamashita, K. Yamatake, M. Odawara, and T. Udagawa, Thin Solid Films 464–465, 120 (2004).
[21]. K. Shohno, H. Ohtake, and J. Bloem, J Cryst Growth 45, 187 (1978).
[22]. Y. Kumashiro, T. Yokoyama, A. Sato, and Y. Ando, J Solid State Chem 133, 314 (1997).
[23]. Y. Kumashiro, T. Yokoyama, T. Sakamoto, and T. Fujita, J Solid State Chem 133, 269 (1997).
[24]. Y. Kumashiro, Y. Okada, and S. Gonda, J Cryst Growth 70, 507 (1984).
[25]. Y. Kumashiro, Y. Okada, and H. Okumura, J Cryst Growth 132, 611 (1993).
[26]. Y. Kumashiro, T. Enomoto, K. Sato, Y. Abe, K. Hirata, and T. Yokoyama, J Solid State Chem 177, 529 (2004).
[27]. Y. Kumashiro, K. Sato, S. Chiba, S. Yamada, D. Tanaka, K. Hyodo, T. Yokoyama, and K. Hirata, J Solid State Chem 154, 39 (2000).
[28]. Y. Kumashiro, K. Nakamura, T. Enomoto, and M. Tanaka, J Mater Sci: Mater Electron 22, 966 (2010).
[29].Cheung, Rebecca (2006). Silicon carbide microelectromechanical systems for harsh environments. Imperial College Press. p. 3. ISBN 1-86094-624-0.
[30]. U. STARKE et al, SURFACE REVIEW AND LETTERS 6 (1999) 1129-1141.
[31]. Tatau Nishinaga et al, Journal of Crystal Growth, Vol 13–14, May 1972, Pages 346–349 .
[32]. M Takigawa, M Hirayama, K Shohno. Jpn J Appl Phys 13:411, 1974.
[33]. Nishinaga et al, Japanese journal of applied physics, yr:1975 vol:14 iss:6 pg:753 -760

[34]. Takao Takenaka et al, J. Electrochem. Soc. 1978, Volume 125, Issue 4, Pages 633-637.
[35]. Y. KUMASHIRO et al, Journal of Crystal Growth 70 (1984) 507—5 14 507.
[36]. Y. KUMASHIRO et al, Journal of the Less-Common Metals, 143 (1988) 71 - 75 71.
[37]. S. Nishimura et al, Optical Materials 19 (2002) 223–228.
[38]. M. Odawara et al, Journal of Crystal Growth 258 (2003) 431–434.
[39]. T. Yamashita et al, Thin Solid Films 464–465 (2004) 120– 122.
[40]. S. Dalui, A.K. Pal. Applied Surface Science, 254 (2008) 3540–3547
[41]. Y. Kumashiro, M. Matsumoto, H. Yoshizawa. Heteroepitaxial growth of boron phosphide single crystal on sapphire single crystal. JJAP Ser 10:160, 1994.
[42]. M. Odawara et al, Applied surface science, yr:2005 vol:244 iss:1-4 pg:289 -292
[43]. D. Hobgood et al, Materials Science Forum Vols. 338-342 (2000) pp 3-8.
[44]. T. Udagawa et al, Applied Surface Science 244 (2005) 285–288.
[45]. Julia K.C. Abbott, J. Daniel Brasfield, el al." Chemical Vapor Deposition of Boron Phosphide Thin Films", 2012 MRS spring meeting.
[46]. UGOCHUKWU NWAGWU, Dissertation. Kansas State University (2013)
[47]. Zhenmeng Peng and Hong Yang, Nano Today (2011) 6, 265—285
[48]. Wild C, Herres N, Koidl, P. J Appl Phys 1990;68:973.
[49]. Wild C, Koidl P, Muller-Sebert W et al, Diam Related Mat, 1993;2:158.
[50]. Peter Smereka et al, Acta Materialia 53 (2005) 1191–1204
[51]. Paritosh, Srolovitz DJ, Battaile CC, Li X, Butler JE. Simulation of faceted film growth in two-dimension: microstructure morphology and texture. Acta Mater 1999;47:2269.
[52]. P. D. Brown, Y. Y. Loginov, W. M. Stobbs & C. J. Humphreys. Philosophical Magazine A, Vol 72, Issue 1, 1995
[53]. O. A. Shenderova and Donald W. Brenner, Phys. Rev. B 60, 7053–7061, 1999
[54]. M. Kohyama, R. Yamamoto, and M. Doyama, Phys. Status Solidi B 137, 11, 1986
[55]. V. Germain, Jing Li, D. Ingert, Z. L. Wang, and M. P. Pileni, J. Phys. Chem. B, Vol. 107, No. 34, 2003

[56]. C. Guedj, M. W. Dashiell, L. Kulik, J. Kolodzey, and A. Hairie, J. Appl. Phys. 84, 4631 (1998)

[57]. AlexanderA.Lebedev et al, Physica B 404 (2009) 4758–4760

[58]. Tsunenobu Kimoto and Hiroyuki Matsunami, J. Appl. Phys. 75, 850 (1994).

[59]. Douglas J Paul, Semicond. Sci. Technol. 2004, 19, 75.

[60]. K. Bakke, F. Moraes, Phys. Lett. A 2012, Vol. 376, Issue 45, 2838.

[61]. H. GOTTSCHALGK et al, phys. stat. sol. (a) 46, 207 (1978)

[62]. Williams, DB and Carter, CB, Transmission Electron Microscopy. (1996)

[63]. Egerton, R. F, Electron Energy-loss Spectroscopy in the Electron Microscope. (1996)

VITA

Mr. Guoliang Li was born in Liaocheng, a mid-sized city of Shandong Province in China. After high school study, he was enrolled in Central South University in Changsha, where his career in materials science and engineering began. He completed his Bachelor's degree in materials science and engineering and a minor degree in applied physics.

After graduation from Central South University, Mr. Li continued his study at the University of Tennessee. He joined the materials science and engineering program to pursue a PhD degree.

During his eight years of study and research in the field of materials science and engineering, Mr. Li explored a wide range of topics including electron and ion microscopies, thin film engineering, semiconductor engineering and organic electronics.

Mr. Li is a good team worker with self-motivated and hard-working style. He enjoys doing researches and exploring the unknown. He wishes to gain more knowledge and make contributions to the society.